UNIVERSITÀ DELLA CALABRIA

UNIVERSITA' DELLA CALABRIA

Dipartimento di Chimica

Dottorato di Ricerca in

Scienze e Tecnologie Fisiche, Chimiche e dei Materiali

CICLO

XXX

TITOLO TESI

Gold Nanoparticles: where shape becomes essence. Synthesis and characterization of an outstanding nanomaterial

Settore Scientifico Disciplinare

CHIM/03

Coordinatore: Ch.mo Prof. Vincenzo Carbone

Firma Vincenzo Carbone

Supervisore/Tutor: Ch.mo Prof. Massimo La Deda

Firma Massimo La Deda

Dottorando: Dottoressa Angela Candreva

Firma Angela Candreva

UNIVERSITY OF CALABRIA

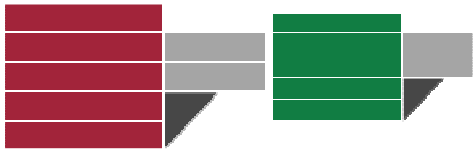

Department of Chemistry and Chemical Technologies
CHIM/03 General and Inorganic Chemistry

Doctorate School of Physical, Chemical, Materials Science and Technologies

PhD Thesis

Gold Nanoparticles: where Shape becomes Essence. Synthesis and Characterization of an Outstanding Nanomaterial

SUPERVISOR
Prof. Massimo LA DEDA

PhD CANDIDATE
Angela CANDREVA

XXX Cycle

First of all I would like to thank my supervisor Professor Massimo La Deda, I'm grateful for everything that he taught me. He supported me in any circumstance, respecting my opinion and leaving me free to synthesize and characterize "disproportionately" high amount of nanoparticles.

Many thanks to Loredana and MATinLAB group: Professor Crispini, Professor Ghedini, Professor Aiello and Doctor Godbert, Franco, Andreea, Eugenia, Debora, Francesco, and in particular Francesca for sharing with me the office and the experience of writing down three years of work. It would have been harder alone. Each one of them helped me whenever I needed making me better professionally and personally.

Thanks to Pierluigi and Emilia for their kindness towards me, and Daniela for sharing my enthusiasm looking at TEM images.

Thanks to Professor Pagliusi who has been working with us on the project to organize the nanoparticles in the liquid crystalline medium.

My warm thanks to professor Luis M. Liz Marzán, Scientific Director of CIC biomaGUNE and leader of BioNanoplasmonics group, who allowed me to work in his group for six months. Thanks a lot to all "Plasmontiger" members for sharing with me their expertises, in particular Leo and Guille. I appreciated it very much guys! Thanks to Wiktor for supervising my experiments giving me great tips.

Lastly I would like to thank my family and all people who supported me along this path.

A glance at the Thesis: scope and limitations

The present book collects the principal results obtained during the three-year PhD course at the Doctorate School of Physical, Chemical, Materials Science and Technologies (Cosenza, Italy). The research work, performed at the Inorganic Materials Laboratory (MAT_IN Lab) of the University of Calabria under the supervision of Prof. Massimo La Deda, and partially at the BioNanoPlasmonics Laboratory from the Centre for Cooperative Research in Biomaterials-CIC biomaGUNE (San Sebastian, Spain), in collaboration with Prof. Luis Liz-Marzán, concerns with **the synthesis and characterization of gold nanoparticles**.

As well known, metallic nanoparticles with a size smaller than the wavelength of the incident radiation, show resonance phenomena with the magnetic field collectively called Localized Surface Plasmon Resonance (LSPR). LSPR properties are extremely interesting because they depends on, and consequently there are controlled by, *metal*, *size*, *shape* and *environment*. In this way, an accurate synthetic method capable of control size and shape, allow to control nanoparticles plasmonic properties. Ultimately, **the plasmon energy can be determined through the shape, which in turn is determined by synthetic procedure.**

LSPR, moreover, can cooperate with other actors that interact with the electromagnetic field. In this way, plasmonic nanoparticles can "talk" with **chromophores**, increasing their absorption cross section, or, if they are emissive, interesting phenomena take place from the correlation between plasmonic field and de-excitation radiative paths.

More interestingly, LSPRs of two or more **assembled nanoparticles** can couple themselves. The way they interact depends on the nanoparticles shape and on the environment. **Anisotropic shaped nanoparticles**, *i.e.* rod-like one, manifest various assembling modes, which determine the properties of the plasmonic-coupled fields. On the other side, an **ordered medium**, acting as arrangement template, can pilot *if* and *how* plasmonic fields couple.

All this aspects, synthesis, morphological characterization, plasmonic optical study, assembly and coupling of **various functionalized gold nanorods**, have been performed, and the results are very encouraging to employs the prepared nanomaterials in various applications, from innovative energy collectors to phototherapeutical cancer-targeted agents.

The Thesis in a nutshell

Chapter 1 – Introduction. A brief review of the essential concepts necessary to introduce the reader has been made. In particular, the synthetic methods to obtain gold nanorods have been illustrated, and the assembling process of these anisotropic nanoparticles has been described, including direct assembly (*i.e.* governed by interparticle forces) or indirect assembly (*i.e.* triggered by a template or an external field). The optical properties of individual and assembled nanorods have been illustrated, with particular emphasis regarding the plasmon coupling.

Chapter 2 – Gold Nanorods Preparation. Here we present synthesis, morphological and optical characterization of gold nanorods prepared *via* seed-mediated method. In addition, original surfactant coating agent has been substituted with other cover molecules, and solubility in various solvents was explored. In particular, we overcoated gold nanorods by a silica shell that deserve a deep study due to its tailorability. Finally, the control of the gold nanoparticles shape through synthetic parameters has been illustrated by preparing gold nanotriangles and gold nanospheres.

Chapter 3 – Silica shell on Gold Nanorods. Taking into account the high tailorability of the silica shell that cover gold nanorods, we discuss the synthetic strategies to control shell thickness and its effects on the plasmonic bands.

Chapter 4 – Functionalization of the Silica shell. Another important feature of the gold nanorods silica shell is the possibility to functionalize it. In particular, a high-luminescent Ir(III) complex has been embedded into the shell, and the exceptional “dialogue” between the radiative deactivation paths of the complex excited-states and the gold core plasmonic field, has been recorded.

Chapter 5 – Nanoparticles coupling. When two nanorods are placed in a close proximity, the plasmon resonances carried by the two nanorods will interact to form different collective plasmon modes. Due to the geometrical anisotropy and the synthetically tailorable plasmon energy of nanorods, coupled nanorods exhibit extremely rich spectral responses. Here we have explored methods to assembly nanorods by using a functionalization of nanoparticles or a nanorods dispersion into organized medium, and the spectral response has been analyzed.

CONTENTS

I. INTRODUCTION

I.1. Origin of surface plasmon resonance in noble metal nanoparticles

I.2. Synthesis of anisotropic gold nanoparticles: seed-mediated growth approach

I.3. Self-assembly of nanoparticles

I.4. Optical properties of individual gold nanorods

I.5. Plasmon coupling in assemblies of metal nanoparticles

I.1. Origin of surface plasmon resonance in noble metal nanoparticles

The electrons in the metal (d electrons in silver and gold) are free to travel through the material. The mean free path in gold and silver is about 50 nm, therefore in particles smaller than this, no scattering is expected from the bulk. Thus, all interactions are expected to be with the surface. When the wavelength of incident light is much larger than the nanoparticle size it can set up standing resonance conditions, as represented in Fig. I.1. [1].

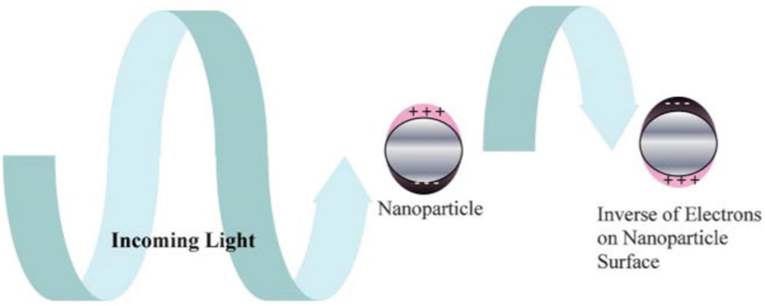

Fig. I.1. Origin of surface plasmon resonance due to coherent interaction of the electrons in the conduction band with light [1]

Light in resonance causes the free-electrons in the metal to oscillate. As the wave front of the light passes, the electron density in the particle is polarized to one surface and oscillates in resonance with the light's frequency causing a standing oscillation. The resonance condition is determined by absorption and scattering spectroscopy and is found to depend on the shape, size, and dielectric constants of both the metal and the surrounding material. This is referred to as the *local surface plasmon resonance (LSPR)*, since it is located at the surface. As the **shape** or **size** of the nanoparticle changes, the surface geometry changes causing a shift in the electric field density on the surface. This causes a modification in the oscillation frequency of the electrons, generating different cross-sections for the optical properties including absorption and scattering.

The **dielectric constant of the surrounding material** will have an effect on the oscillation frequency due to the varying ability of the surface to accommodate electron charge density from the nanoparticles. Changing the capping agent and solvent will change the dielectric constant, determining the shift of the plasmon resonance due to the local nature of its effect on the surface of the nanoparticle. Chemically bonded molecules can be detected by the observed change they induce in the electron density on the surface, which results in a shift in the surface plasmon absorption maximum. This is the basis for the use of noble metal nanoparticles as *sensitive sensors*.

Mie originally calculated the surface plasmon resonance by solving Maxwell's equations for small spheres interacting with an electromagnetic field. Gan was able to extend this theory to apply to ellipsoidal geometries. Modern methods using the discrete dipole approximation allow one to calculate the surface plasmon resonance absorption for arbitrary geometries. Calculation of the longitudinal plasmon resonance for gold nanorods generates an increase in the intensity and wavelength maximum as the **aspect ratio** (length divided by width) increases. Thus, the plasmon resonance can be tuned across the visible region by changing the aspect ratio. The increase in the intensity of the surface plasmon resonance absorption leads to an enhancement of the electric field, exploited in many applications [2].

Many shapes of noble metal nanoparticles have been synthesized [3]. Nanorods [4] have attracted the most attention for the large number of synthetic methods available, the high monodispersity possible, and the rational control over the aspect ratio, which is primarily responsible for the change in their optical properties. Nanorods have been shown to have two plasmon resonances [5] one due to the **transverse oscillation** of the electrons, around 520 nm for gold, and the other due to the **longitudinal plasmon resonance** at longer wavelengths, as shown for various aspect ratios in Fig. I.2.

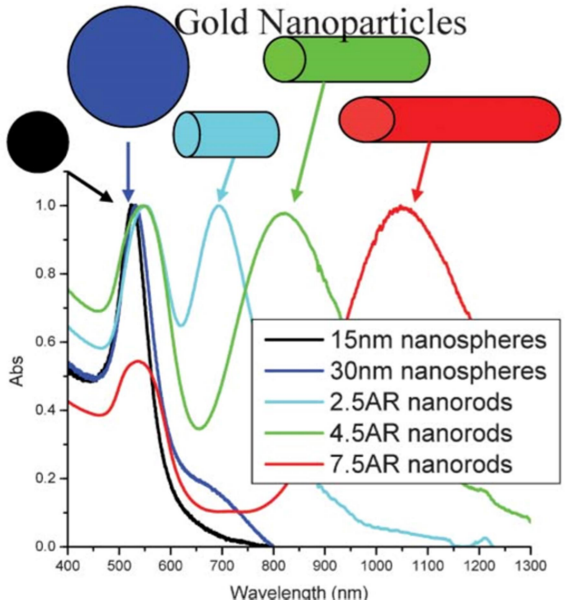

Fig. I.2. Gold nanoparticles: absorption of various sizes and shapes [5]

The transverse surface plasmon resonance does not depend on the aspect ratio and it is at the same wavelength as the plasmon resonance of spheres. The longitudinal surface plasmon resonance increases with larger aspect ratios. The anisotropy has been shown to generate large control over the

optical absorbance for all shapes generated. Triangular nanoparticles have been generated by photochemical means and chemical growth. The edges and corners are very important with triangular nanoparticles. Snipping of the edges produces a visible blue shift in the plasmon resonance, which can be modelled theoretically. Disks also display a similar plasmon resonance absorption dependence on their aspect ratio.

I.2. Synthesis of anisotropic gold nanoparticles: seed-mediated growth approach

The size and shape-controlled synthesis of metal nanoparticles is important in present day advanced materials, as almost every property within the nanometer regime are size and shape dependent [6]. Common methods for size control employ **capping agents** [7], such as surfactants, ligands, polymers, or dendrimers, to confine the growth in the nanometer regime. These methods commonly produce spherical particles due to the low surface energy associated with such particles. Structures other than spheres form as a result of specific interaction of the capping agents with different growing faces of the particles [8].

A shape control of nanoparticles has been most successfully achieved using a **template**. Templates provide a constrained environment during the nanoparticle growth and thus shapes are tuned according to the template. Commonly used templates are porous alumina [9], polycarbonate membranes [10], carbon nanotubes [11] and micelles [12]. In practice, the presence of templates does not produce 100% shape monodispersity; rather, a significant fraction of thermodynamically favourable spheres is also formed. In addition, soft templates such as micelles may not be stable under the experimental conditions (*e.g.*, boiling), and thus the template may not function [13]. A common reason for the failure of the template mechanism is the change in template microstructures by reactants.

Seed-mediated growth approach. Mechanism of conventional nanoparticle synthesis proceeds through successive nucleation and growth steps, both extremely sensitive to physical and chemical parameters [14]. In some of the solution-phase metal nanoparticle synthesis procedures, the control of *nucleation* and *growth steps* are done by changing the reducing agent or stabilizer concentration. In doing so, the size and shape of nanoparticles can be controlled. For solution-phase gold nanoparticle (AuNP) synthesis, it has been observed an initial slow nucleation followed by a nucleation burst associated with autocatalytic surface growth [15]. Through a physical separation of the nucleation process from the growth process, it was possible to control these steps to prepare different sized spherical particles; this method is known as ***seed-mediated growth approach***. By using this growth strategy in the presence of a rod-shaped micelle, [16] a template-mediated shape control can be reached.

The basic principle of shape-controlled synthesis involves **two steps**: *first,* the preparation of small-size spherical AuNPs, and *second*, growth of the prepared spherical particle in rod-like micellar environment (Fig. I.3). This procedure, that take place in aqueous solution at or near room temperature, begins with the synthesis of AuNPs by chemical reduction of $Au^{(III)}$ salt such as

tetrachloroauric acid ($HAuCl_4$) with a strong reducing agent such as *sodium borohydride* ($NaBH_4$) in presence of a *capping agent*, to prevent particle coalescence. The gold spheres thus generated are 3±5 nm in diameter and serve as seeds on which to grow more anisotropic nanostructures. These seeds are then added to a solution containing more $Au^{(III)}$ salt, a weak reducing agent, such as *ascorbic acid* and a rodlike micellar template such as *cetyltrimethyl ammonium bromide* (CTAB). The seeds serve as nucleation sites for gold nanorods (AuNRs) growth; under these conditions, no metal salts are reduced to metal unless the seeds are present. Consequently, minimal additional nucleation occurs during particle growth. Typical product dimensions are 10-20 nm diameter short axis and aspect ratios up to 20 for AuNRs.

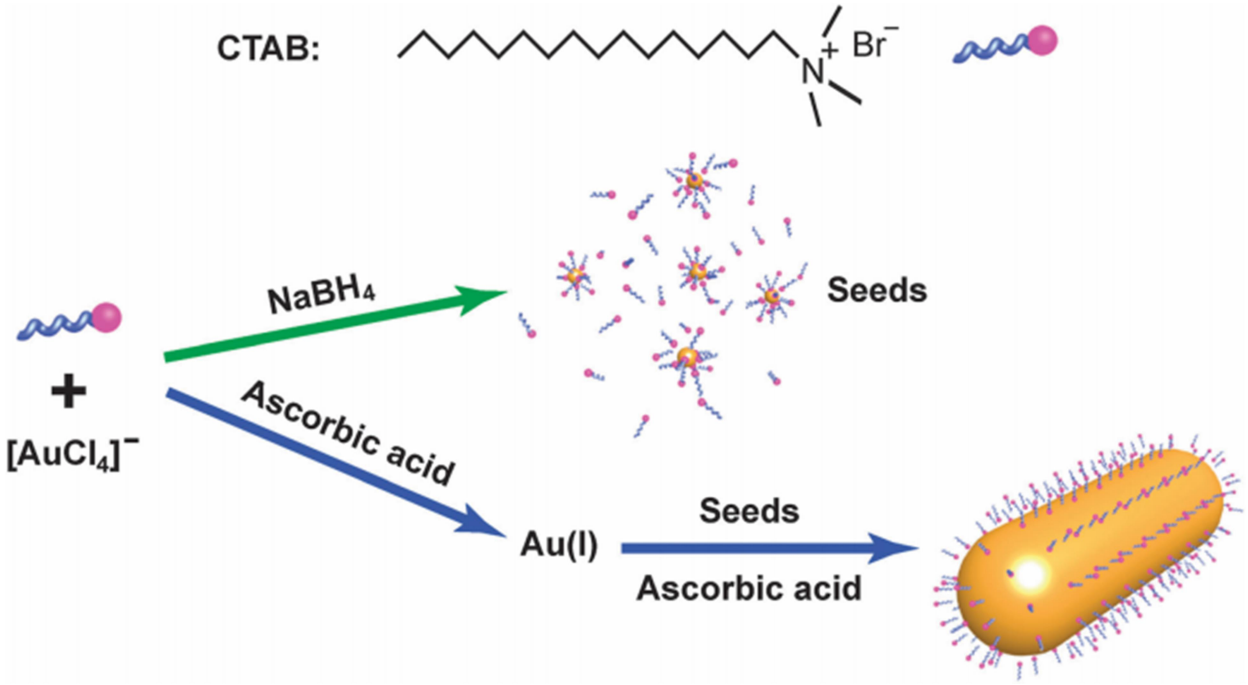

Fig. I.3. Schematic illustration of the seed-mediated method for the growth of Au nanorods [17]

The presence of additives, such as *5-bromosalicylic acid*, in the reaction media can fine-tune the morphology of the resulting nanorods [18].

A small amount of $AgNO_3$ is added for shape induction. The presence of silver salt is essential for producing and controlling the aspect ratio of rods. In absence of Ag^+, fewer rods (~10-20 % of the total particles) form and their aspect ratios are higher and have a wide distribution, ranging from ~5-15. Murphy *et al.* [19] proposed that the Ag^+ forms AgBr (Br^- from the CTAB), and because ascorbate is a weak reducing agent, it cannot reduce the silver ion. The mechanism by

which Ag^+ assists in controlling gold particle shape is not completely understood; however, it was hypothesized that Ag^+ adsorbs at the Au particle surface in the form of AgBr and restricts growth. The adsorption of AgBr at the Au particle surface appears to stabilize the spheroids and rods. In absence of Ag^+ the spheroids formed, but due to their instability, converted to spheres.

Size control. **Surfactants** are considered dynamic templates that in a precise concentration, called critical concentration, and temperature, form micelles. These are compartments of nanometer size able to confine the nanocrystals growth and control and limit physically their enlargement. A layer of surfactant covers the surface of the formed nanoparticles. In fact, acting like surface complexing agent it prevents the irreversibly aggregation of nanoparticles [20]. According to Scarabelli *et al*. [21] [18], the final size it is also dependent by the amount of seed solution added to the growth solution and by the pre-reduction time.

*Shape control***.** The growth inside micellas not only confer a size control, but also a degree of shape control. It is studied that surfactants are able to adhere with different bonding strengths to the various facets of the nanocrystals and induce their preferential development along those crystallographic directions which grow fastest [20]. The surface covering plays a crucial role in the morphology of the product, each capping agent being selective for a specific shape [22]. Canbek *et al.* [23] demonstrated that the final shape of the nanoparticles depends also on the capping of the seeds. In particular, seeds with size around 3 nm and positive charge, coming from CTAB covering, are the best choice to synthesize nanorods with high yield. On the other hand seeds with size around 7 nm and negative charge which comes from sodium citrate have to be preferred if the spherical shape is the challenge.

Another important contribution on shape control is given by silver ions and halides in seed-mediated synthesis. Liz-Marzán and other groups [24] studied how they can be used to control particle shape and surface facet structure. It is clear that the halidates direct the anisotropic shape and that halide counterion plays a crucial role in the growth processes of anisotropic gold nanoparticles, but it is not yet clear which halide-metal interaction are primarily responsible for shape control [17]. Many study are trying to demostrate that halide ions may direct the anisotropic growth of metal nanocrystals modulating the redox potentials of the metal ions, acting as face-specific capping agents, and or controlling the extent of silver underpotential deposition at the nanocrystal surface. According to the literature [25] bromide is the right choice to obtain well-defined gold nanorods and iodide for nanoplates shapes. Iodide seems to prevent gold nanorods formation.

CTAB: stabilizing and directing agent for rod-like nanoparticles. CTAB, composed by a hydrophilic cationic head group and a hydrophobic tail, is used as stabilizing and directing agent for the growth of anisotropic shape. CTAB forms complexes $Au^{(I)}$ and stabilizes metal nanoparticles forming a bilayer around them (Fig. 1.4) [23].

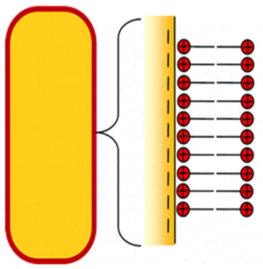

Fig. I.4. CTAB bilayer on the surface of gold nanorods

CTAB is present on the whole nanorods surface as a bilayer through electrostatic interactions of the ammonium head group.

It is demonstrated that using CTAC (*cetyltrimethyl ammonium chloride)* instead of CTAB no nanorods are formed. This is because increasing the CTAB concentration (from 0.3 E-3 M to 0.1 M) spherical micelles transit towards elongated micelles, while CTAC forms always spherical micelles [23].

On this basis were performed various seeded growth method protocols to achieve different shapes. For example, Scarabelli *et al.* [21] proposed a successful synthesis and purification protocol to obtain well monodispersed gold nanotriangles covered with CTAC. Gold nanotriangles show interesting plasmonic properties with possible application in many fields. The synthetic protocol is based on the seed-mediated growth originally proposed by Mirkin and co-workers [26]. CTAC and iodide anions are requested to achieve the triangular shape. Adopted protocols involve three crucial steps: synthesis of CTAC-coated Au seeds, fast addition of the generated seeds to a final growth solution, and purification of the products from CTAC. Thanks this synthetic procedure the shape-yield increase up to 95%. This successful way to eleminate synthetic byproducts is based on the action of the depletion force. On this basis, Park *et al*. [27] demonstrated a robust and efficient procedure of shape and size selection of Gold nanoparticles (AuNPs) through the formation of reversible flocculates by surfactant micelle induced depletion interaction. AuNP flocculates form at a critical surfactant micelle molar concentration (*C*m*), where the number of surfactant micelles is sufficient to induce an attractive potential energy between the AuNPs. Since the magnitude of this potential depends on the interparticle contact area of AuNPs, separation is achieved even for the

NPs of the same mass with different shape by tuning the surfactant concentration and extracting flocculates from the sediment by centrifugation or gravitational sedimentation. The refined NPs are redispersed by subsequently decreasing the surfactant concentration to reduce the effective attractive potential. These concepts provide a robust method to improve the quality of large scale synthetic approaches of a diverse array of NPs, as well as fine-tune interparticle interactions for directed assembly, both crucial challenges to the continual realization of the broad technological potential of monodispersed NPs.

Bastus et al. [28] synthesized citrate-stabilized gold nanospheres following a kinetically controlled seeded growth strategy via the reduction of $HAuCl_4$ by sodium citrate, improving the Frens method and, by adjusting the reaction conditions: temperature, gold precursor, seed particle concentration and pH, it is guaranteed a homogeneous growth and inhibited any secondary nucleation.

Silver ions and anisotropic growth. Murphy [29] suggested three mechanism to interpret the role of silver in the seeded growth gold nanorods synthesis (Fig. I.5).

1. *The complex* $CTA^+ - Br^- - Ag^+$ could be able to avoid the growth along the longitudinal faces promoting, therefore, the growth at the AuNR caps.
2. *CTAB micelles* become cylindrical in the presence of silver ions, bromide ions, and the gold seed. Gold monomer then adds to the seed, while the CTAB micelle acts as a soft template controlling the shape.
3. *A silver monolayer* could deposit on the longitudinal faces of the AuNR, blocking the growth on these faces favouring the formation of structures like rod (silver under-potential deposition). Generally, the source of silver ions used in to the synthesis is silver nitrate. It promotes, during formation of gold nanorods, the anisotropy increasing the yield of the final product.

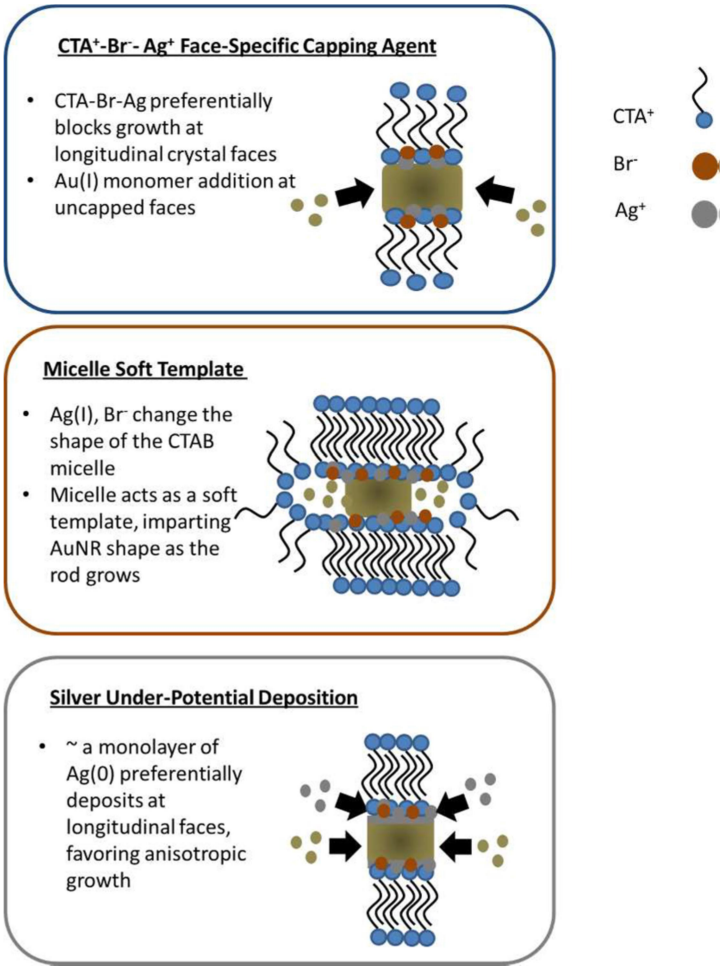

Fig. I.5. Models of Ag^+ action in seeded growth of AuNRs, according to literature [29].

Capping agents. Gold nanoparticles in general and gold nanorods in particular cannot stay "naked"; according to the surrounding environment, it is possible to cover them with different capping agents. It is possible alter the chemical behaviour, such as solubility, by changing the surface covering of nanoparticles. CTAB ensures the stability of nanoparticles in water [18], polyethylene glycol thiol (PEG-SH) in water and organic solvent [30]. Doping the layer of PEG-SH with dodecanethiol (DDT) [31], nanoparticles become selectively soluble in organic solvent like chloroform.

A winning move to confer stability and functionality to gold nanorods is improving the coating. On this perspective various research groups, such as Liz-Marzán (the first one), starting from Stober method [32], Tracy [33], tuned technique for coating gold nanorods with silica shells. Silica shell is a tuneable, protective and versatile covering. The thickness of the shell, which can controlled, influence the optical properties of nanorods.

I.3. Self assembly of nanoparticles

Self-assembly refers to the process by which nanoparticles organize themselves by a direct specific interactions and or indirectly, through their environment. It is typically associated with thermodynamic equilibrium, the organized structures being characterized by a minimum in the system's free energy, although this definition is too broad [34]. Self-assembly reflects features of individual components as shape, surface properties, charge, polarizability, magnetic dipole, mass, etc. responsible of the interactions between them. It is based on the evolution towards an equilibrium state with the consequent formation of ordered structures. In fact, essential in self-assembly is that the building blocks organize into ordered, macroscopic structures, either through *direct* interactions (*e.g.* by interparticle forces), or *indirectly* using a template (including the surface where NRs are deposited) or an external field. Generally, due to their anisotropic shape, gold nanorods can be interact themselves by an end-to-end or side-by-side arrangement, as reported in Fig. I.7.

a) b)

Fig.I.6. End-to-end (a), side-by-side (b) arrangement of AuNRs

Among the large number of stimuli easily accessible in nature or even in the chemistry lab, one can identify temperature, light, solvent polarity, or even ion concentration as suitable triggers for the assembly processes. The intermolecular forces involved, which can be modulated by the above listed stimuli, are related to hydrophobic interactions, hydrogen bonding, molecular dipole interactions, or π-π stacking.

There have been mainly four self-assembly strategies: ***solvent evaporation-induced assembly, assembly through small thiol molecules, assembly through biological molecules and polymers and assembly using templating method.***

Solvent evaporation-induced assembly

CTAB bilayer, formed around AuNRs, makes them positively charged. CTAB can induce electrostatic repulsion or interchain attraction, by van der Waals attraction, between different AuNRs when they approach each other. This apparent disagreement can be overcome if we consider that in aqueous environment an equilibrium between CTAB in free micelles and CTAB bilayered on NRs surfaces takes place. When an external stimulus such as purification depletes water solution from free CTAB, to restore the perturbed equilibrium, CTAB molecules leave AuNRs bilayer. In this way, CTAB aliphatic chain is exposed to the aqueous environment, which consequent interchain attraction. This balance between electrostatic repulsion and van der Waals attraction, results in an assembling of the AuNRs.

To trigger the assembly process, a small amount of the solution containing AuNRs is usually dropped on a flat substrate. As the solvent is progressively evaporated, AuNRs will be carried toward the edge of the droplet by the outward solvent flow due to the capillary force. The concentration of AuNRs at the edge therefore becomes higher and the spacing between different AuNRs is reduced. The counterbalances among the van der Waals attraction, electrostatic repulsion, and capillary forces thereafter lead to the formation of a mesophases-like organization of AuNRs, once the NR concentration at the edge increases up to a certain point [35].

El-Sayed et al. [17] and Murphy et al. [36] conducted the pioneering works using the solvent evaporation-induced assembly approach to fabricate ordered AuNRs superstructures. The obtained superstructures are similar to smectic-A liquid-crystalline phases with AuNRs aligned parallel with each other in a layer-by-layer manner. The mechanism governing the parallel alignment could be originated by the capillary force along the length of a nanorod which is larger than that along its width.

The **concentration** of the sample tremendously determines the nanoparticles organization [35]; in fact, an increasing of the sample concentration induces a high degree of organization. Fig.I.7 reports TEM images of drop-casted AuNR@CTAB solutions with different concentration: the organization degree increases from low (a) to high (c) concentration. Later studies have shown that the obtained AuNRs superstructures are strongly dependent not only on their concentration, but also on their **aspect ratio**. Increasing concentration, NRs with small (<7) or large (>7) aspect ratios show a transition from an isotropic arrangement towards a smectic-like or a nematic-like arrangement, respectively (Fig.I.8). In addition, the tuning of the aspect ratios, allows to obtain various superstructures, such as honeycomb structures, higher-order smectic two-dimensional structures, lower-order one-dimensional ribbon structures (Fig.I.9).

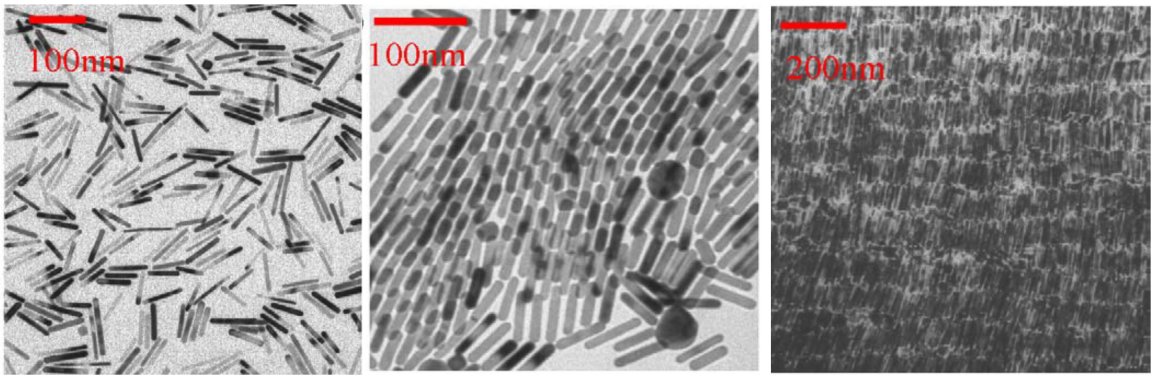

a) b) c)

Fig.I.7. TEM images of drop-casted AuNR@CTAB derived from solutions with different concentration: the organization degree increases from low (a) to high (c) concentration [35].

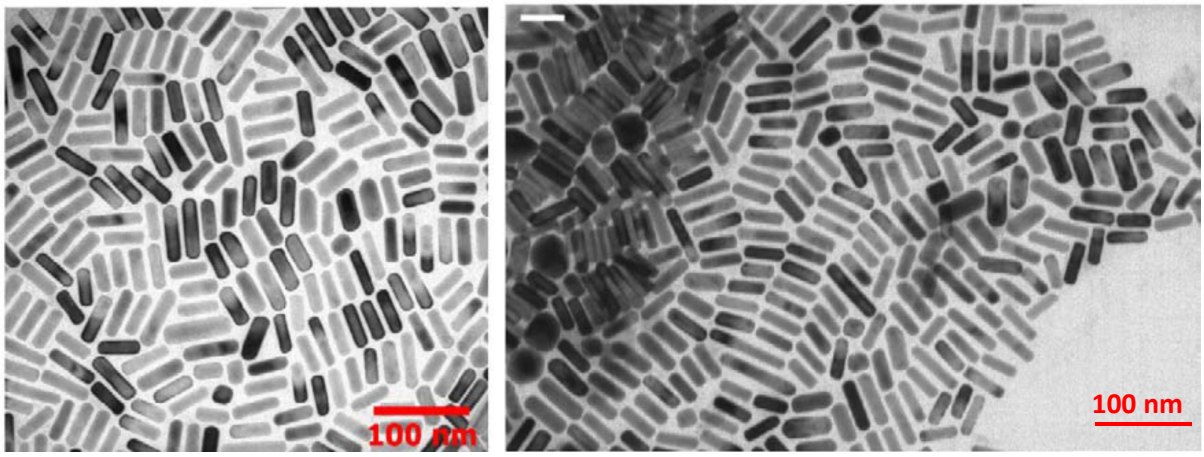

a) b)

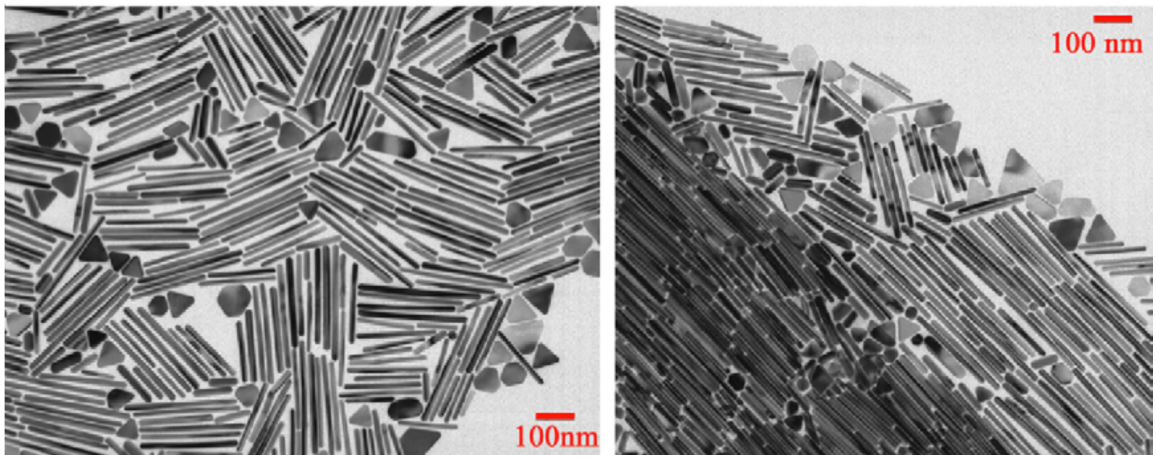

c) d)

Fig.I.8. TEM images of gold NRs assembly. a) Isotropic (b) and smectic-like assembly achieved increasing the concentration of NRs with aspect ratio 3. (c) Isotropic (d) and nematic-like assembly achieved increasing the concentration of NRs with aspect ratio 14 [35].

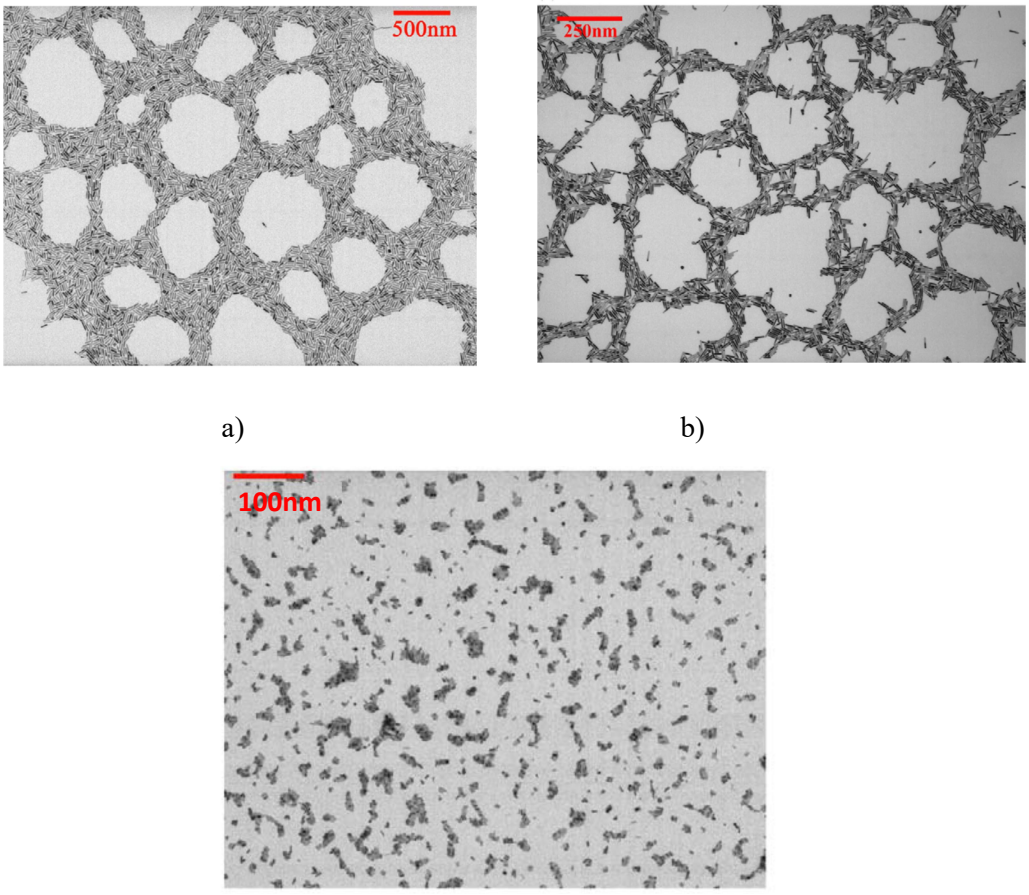

Fig.I.9. The cellular network structure formed by gold NRs with different aspect ratios: (a) aspect ratio of 4 and (b) aspect ratio of 6, (c) ribbon assembly of NRs [35]

The **CTAB concentration** is believed to affect the coverage of the CTAB molecules on AuNRs, which, as already observed, can perturb the assembly process via the van der Waals attraction, electrostatic repulsion, and molecular interchain attraction. So, the concentration of CTAB in solution has been shown to be an important parameter that governs the final NR superstructures [35].

Hamon *et al.*[37], proposed to exchange CTAB cover of AuNRs with a different surfactant, such as MUDOL (1-mercaptoundec-11-yl)hexa(ethylene glycol) to improuve the assembly. In fact, CTAB-coated AuNRs possess a **positive surface charge** (ζ = +40 mV), inducing a highly repulsive forces. Instead, the zeta potential of MUDOL-coated AuNRs was significantly lower (ζ = +10 mV) and self-assembly occurred at low AuNRs concentrations.

Shape and size **homogeneity** of the AuNRs is an important point in determining the assembling degree [38]. Increasing the homogeneity, the assembling degree improuves (Fig. I.10.a);

this is due to the high affinity of nanoparticles with the same morphology, that as consequence, tend to assemble (Fig. I.10.b). This process is driven by the depletion force, that arises when large particles are placed in a solution of smaller ones, and sterically constrained to avoid them [39] [27].

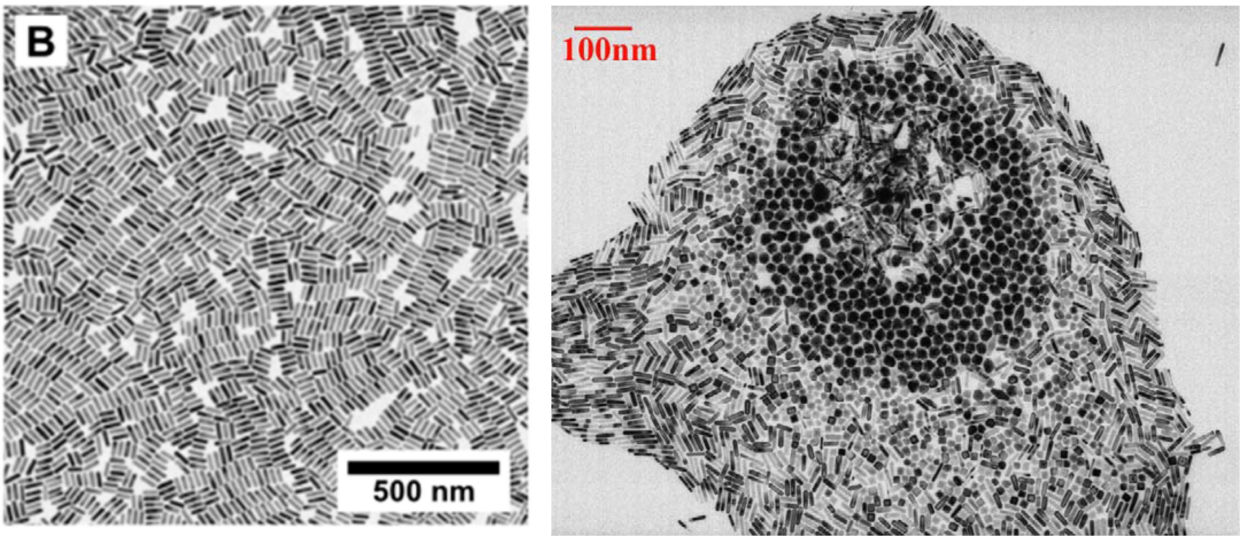

a) b)

Fig. I.11 a) TEM image of AuNR@CTAB with a high shape yield; b) TEM image of of 3 different shapes of nanoparticles assembled separately [35] [38]

Assembly through small thiol molecules

In addition to the roles previously reported, functionalization of AuNRs is often needed for their assembly into a variety of superstructures and the inclusion of new functionalities. Small thiol molecules can be employed as linkers to assemble AuNRs into oligomers or long chains [40]. Molecules containing thiol groups are widely used to functionalize Au surfaces due to the formation of strong Au–S bonds. The end or side surfaces of Au nanorods can be selectively functionalized for end-to-end or side-by-side assembly with dithiol molecules or thiol-containing bifunctional molecules. Bifunctional molecules as 3-mercaptopropionic acid and 11-mercaptoundecanoic acid induce the assembly of AuNRs through intermolecular hydrogen bonding [41]. In this case, the assembly and disassembly can be controlled by changing the pH value of the solution: low pH is responsible of strong hydrogen-bond interactions while repulsive electrostatic interactions are observed at high pH.

Assembly through polymers and biological molecules

Kumacheva *et al.* [42] have provided the details on polymer-induced assembly of AuNRs, realized by functionalising AuNRs with a polymeric ligands. When the affinity of the polymer for the solvent is low, an attractive interaction among AuNRs is produced. The assembly of polymer-tethered AuNRs can be manipulated by varying the position of the polymeric ligands on the NRs surfaces region, the volume ratio between the nanorod and the polymer blocks, and the solvent selectivity according to simulation results. The length of the polymer chain can also be varied to control the assembly of AuNRs. End-to-end or side-by-side assembly of AuNRs have been achieved by selectively attaching polymers to the side and end surfaces of the NRs, respectively, as showed in Fig.I.12.

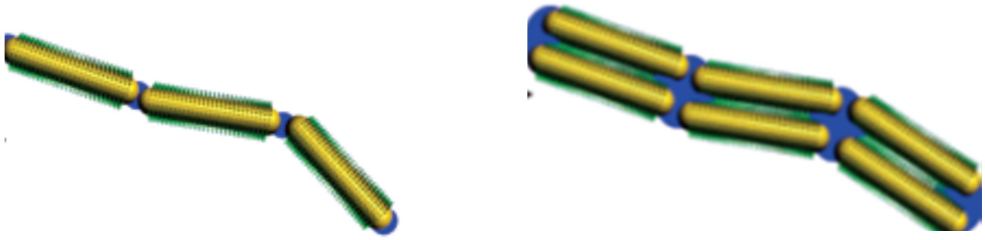

a) b)

Fig.I.12. End-to-end (a) or side-by-side (b) assembly of AuNRs have been achieved by selectively attaching polymers (indicated with blue) to the side and end surfaces of the NRs, respectively [42].

Thiol-terminated biological molecules have been often utilized to assemble AuNRs. The assembly is achieved through biological ligands [42], such as avidin and biotin, antibody–antigen, aptamer–protein, oligonucleotides–metal ions, and DNA sequence recognition. DNA hybridization enables DNAs to act as templates to direct the assembly of AuNRs.

Assembly using templating method

In geometrical terms, templates can be considered as surface-modified substrates (in 1D, 2D, or 3D), containing active sites, which selectively induce nanoparticle deposition. The template is considered as *any* object serving as a scaffold onto which different particles can be arranged into a structure with a morphology that is complementary to that of the template. On this point of view a variety of elements, such as single molecules, microstructures (*e.g.* carbon nanotubes) or block copolymers, can become templates. Recently, an additional distinction between soft and hard templates has been proposed. [34] Soft templates possess a spatial distribution of specific reactive

sites with affinity toward certain particles, resulting in a controlled periodicity of the assembled particles with a positional order, and eventual formation of hierarchical structures (*e.g.* DNA). On the contrary, a hard template, even if it define an order of the final structure, the control that it provides over periodicity is rather poor.

According to Murphy [43], Lacaze [44], Kumacheva [45[and other, **liquid crystals** are successfully templates for nanoparticles assembly. Liquid crystal (LC)–nanoparticle (NPs) composites have drawn significant attention and are now one of the hot topics in LC research. The assembly of NPs in LC has been extensively studied particularly with the aim of forming ordered and predicable arrays that utilises the unique properties of NPs, as well as the collective properties of NP arrays.

The relationship between nanoscience and liquid crystals is so deep that a new term ‘‘liquid crystal nanoscience’’ has come into common use. Mobile at the molecular level, liquid crystalline phases are self-organized at the nanoscale into one-, two-, or three-dimensional nanostructures. In addition, because liquid crystals are composed of anisotropic molecules (rod-like, disk-like, bent-core), are very sensitive to external physical fields. Thus their spatial ordering as well as their physical properties can be tuned in a desirable way. LCs are very welcoming to nanoparticles (and in particular anisotropical shaped NPs) which are mixed with them, or are perfect to be embedded into other materials/confinements [46].

Various experts, like Lacaze, focused their attention on **topological defects** of liquid crystal matrices. They showed that NPs can be trapped and accumulated into defect cores, reducing the molecular disorder and the free energy of the LC phase [44]. Films of smectic LC deposited onto a solid substrate induce planar anchoring of the LC director, while a homeotropic (normal) anchoring was generated at the air interface. This produces a distorted texture, the so-called 'oily streaks', containing periodic curvature walls and disclination lines, perpendicular to the planar anchoring. Lacaze used films of smectic 8CB (4-n-octyl-4'-cyanobiphenyl) deposited onto a MoS_2 substrate to produces the 'oily streaks', in which were successfully trapped nanospheres (Fig.I.13) [47] and nanorods [48].

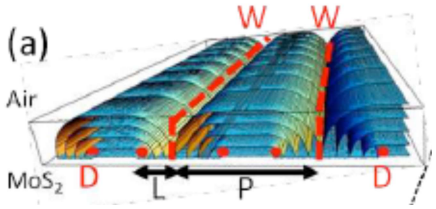

Fig.I.13. Schematic illustration of a linear array of straight parallel oily streaks in which only smectic layers are represented, with disclination lines (D) and curvature walls (W) [47].

Cipparrone [49] reported a strategy to assemble and manipulate nanoparticles in defect lines arrays created in liquid crystal, exploiting periodic arrangements of twisted domains with opposite handedness. The defect lines self-organize in a planar cell guided by a polarization hologram recorded in one aligning substrate that provides planar periodic alignment. Depending on the relationship between the cell thickness and the hologram pitch Λ, the array period can be either Λ or $2\,\Lambda$.

Liquid crystals can also be considered as a model of cell membranes [46]. A number of biophysics experiments considering the interactions of gold nanoparticles with such model systems have been studied. Lyotropic liquid crystals have been found to be the most suitable systems for modelling of living objects. Recently, a lyotropic mesophase has been used as a selective filter for gold nanoparticles, giving new insight toward the understanding of complicated biological structures.

I.4. Optical properties of individual gold nanorods

LSPRs, the surface electromagnetic modes associated with the confined collective oscillations of the conduction electrons, are the most exceptional properties of metal nanostructures. Under resonant excitation, noble metal nanostructures concentrate free-space electromagnetic waves within the near-field regions (<100 nm) close to their surfaces. This unique property enables noble metal nanostructures with various splendid effects, such as extremely large electric field enhancements, nanoantenna characteristics, huge light scattering and absorption, and striking photothermal conversion capabilities. In addition, the **plasmonic properties of metal nanostructures are strongly affected by their geometries**. For example, the plasmon wavelengths, where the strong light absorption or scattering occurs, of spherical metal nanocrystals are determined by their diameters, giving rise to the vivid colours of their colloidal solutions. Elongation of metal nanocrystals lowers their geometrical symmetry and thereby enriches their plasmonic properties. Compared to their spherical counterparts, Au nanorods exhibit anisotropic plasmon responses that are determined by the electron oscillation dynamics along different directions. In addition, such an anisotropic behaviour also enables various intriguing plasmon coupling properties, which depend strongly on the arrangements of AuNRs. Under the inspiration by all of these fascinating characteristics, tremendous research progress has been made on studying the plasmonic properties of AuNRs during the past few years [17].

Gold nanorods with cylindrical symmetry usually exhibit two plasmon modes, a longitudinal LSPR mode associated with the electron oscillations along the length direction and a transverse LSPR mode arising from the transverse electron oscillations. Due to the longer path of the electron movements, the longitudinal mode is located at the red side of the transverse one. Both modes are dipolar resonances and can be efficiently excited by external plane waves.

The plasmonic responses of metal nanostructures can be precisely simulated by various rigorous numerical algorithms, such as finite-difference time-domain (FDTD) methods, boundary element methods (BEMs), and discrete dipole approximation (DDA). However, these numerical procedures cost large amounts of computational resources without capturing the underlying physics. On the other hand, for metal nanostructures with sizes much smaller than the incident wavelength, quasistatic theories can be employed for describing the plasmonic properties associated with dipolar modes. Within the framework of quasistatic approximation, the electromagnetic field is treated to be the same throughout the entire particle. It is then solely determined by the scalar potential. Gans theory [50] is the most famous quasistatic theory for calculating the light scattering and absorption of nanocrystals with an ellipsoidal shape.

From Gans theory, one can clearly see that the scattering or absorption cross-sections and plasmon wavelengths vary with the size and shape of Au nanorods. By progressively increasing the aspect ratio of the nanorod with a fixed diameter, the extinction cross-sections of both the longitudinal and transverse plasmon modes will be enlarged (Fig. I.14).

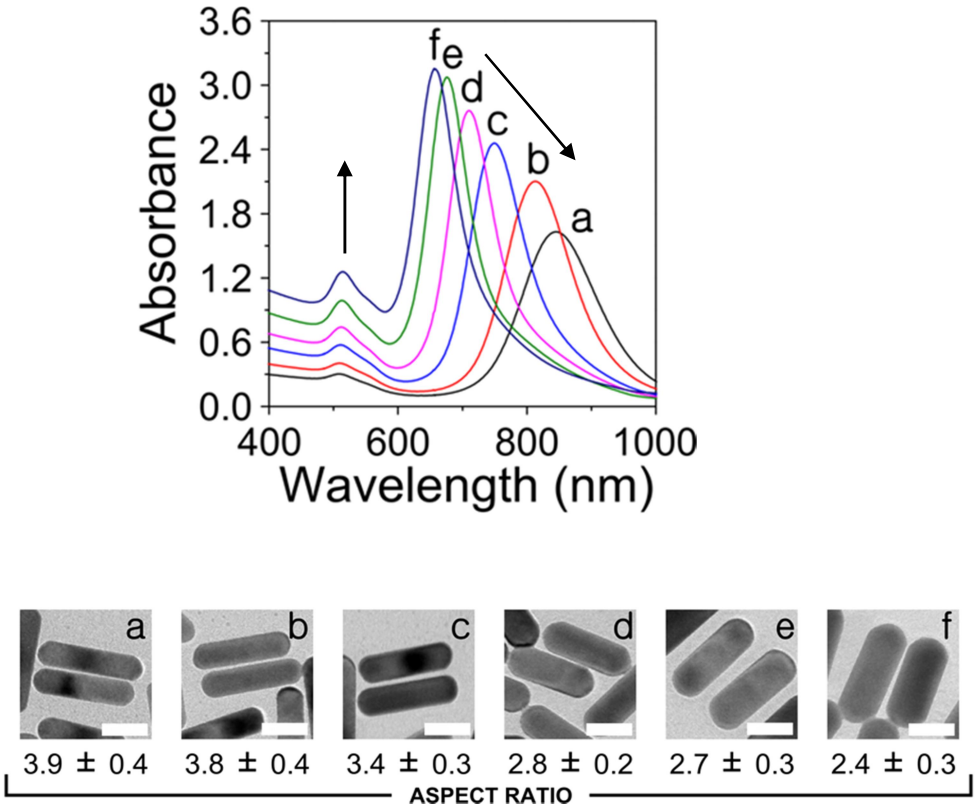

Fig. I.14. Extinction spectra of AuNRs with different aspect ratios, correlated with TEM images [18].

In addition, the plasmon wavelengths of these two modes will also be changed. For the transverse mode, its wavelength exhibits a small blue shift when the aspect ratio is increased [17]. On the contrary, the longitudinal mode of the nanorod exhibits a much more sensitive behavior. It red-shifts by up to several hundred nanometers for the same change in the aspect ratio. The much larger dependence of the longitudinal plasmon wavelength on the aspect ratio results from the higher polarizability of the nanorod at the longitudinal plasmon resonance. The polarizability usually determines how easily a nanocrystal can be polarized. Nanocrystals with higher polarizabilities can induce more polarization charges, leading to larger plasmon shifts as their

geometry is changed. Moreover, the longitudinal plasmon wavelength is nearly linearly dependent on the aspect ratio of the nanorod (Fig. I.15). Such a linear behavior is expected from Gans theory by considering the nearly linear dependence of the real part of the Au dielectric function on the wavelength in the visible range [51].

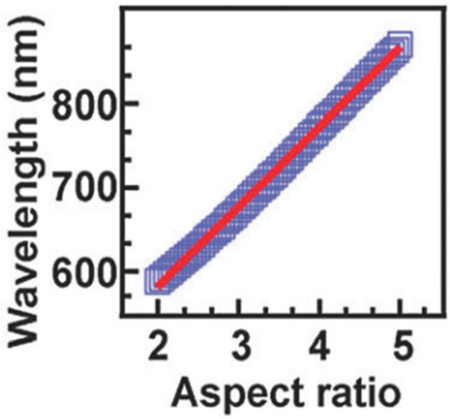

Fig. I.15. Dependence of the longitudinal plasmon wavelength on the aspect ratio.

As predicted by the Gans theory, the scattering cross-section of the nanorod is a quadratic function of the particle volume while the absorption cross-section exhibits a linear dependence. Therefore, the scattering, absorption, and extinction cross-sections of AuNRs show nonlinear dependences on the diameter of the nanorod even if their aspect ratio is fixed (Fig. I.16).

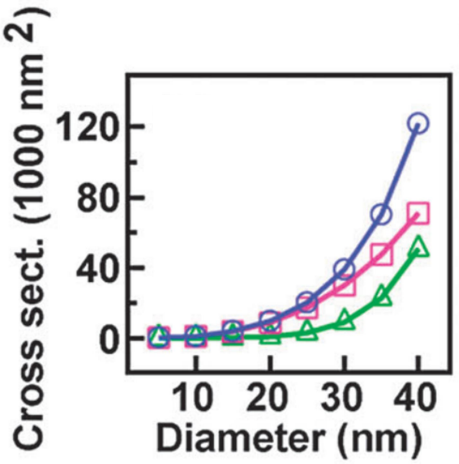

Fig. I.16. Extinction (circles), scattering (triangles), and absorption (squares) cross-sections versus the diameter calculated according to Gans theory. The aspect ratio is 2.4.

The electric field distribution around the nanorod can be computed from the gradient of the electric potential, whereby the electric field enhancement can be obtained. Regions with high curvatures, such as the two ends of the nanorod, can concentrate electrons at higher volume densities and therefore lead to higher electric field enhancements (Fig. I.17) [52].

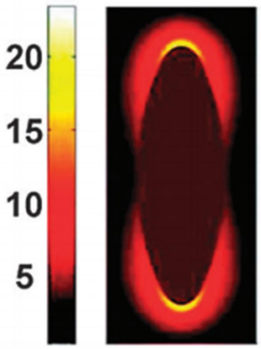

Fig. I.17. Electric field enhancement contour of an AuNR with aspect ratio of 3

The electric field enhancement is also a function of the nanorod geometry. By extracting the maximum electric field enhancement around the nanorod at the longitudinal plasmon resonance, one can clearly see that the field enhancement grows monotonically with the aspect ratio of the nanorod (Fig. I.18) [53].

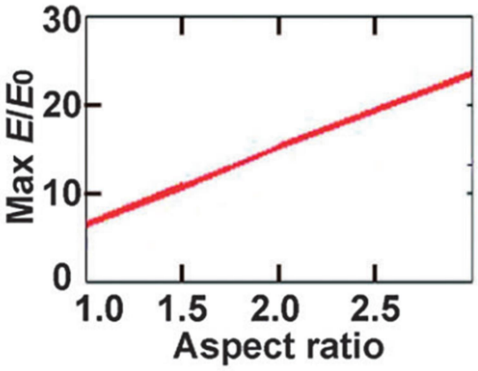

Fig. I.18. Change of the maximum electric field enhancement as a function of the aspect ratio at the longitudinal plasmon resonance

This dependence arises from the red shift of the longitudinal plasmon resonance into regions far away from the interband transition of gold, which reduces the damping of the plasmon

resonance [54]. Rigorous numerical calculations have shown that the electric field enhancement can also be affected by the head curvature as well as the volume of the nanorod [55].

Once the plasmon resonance is excited, it will decay rapidly mainly by the generation of electron–hole pairs, thermalization with the lattice through Joule heating, and emission of photons (Fig. I.19).

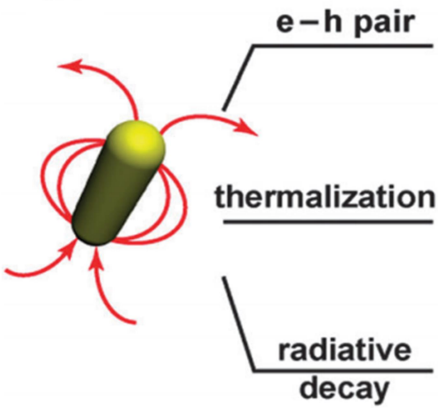

Fig. I.19. Schematic showing the major plasmon damping pathways of a single Au nanorod. [49]

These three decay channels govern the plasmon damping dynamics and thereby the linewidth of the plasmon resonances. Feldmann *et al*. have shown that plasmon damping is drastically reduced in Au nanorods compared to that in Au nanospheres, which is due to the suppression of the electron– hole pair formation through interband transitions [53].

Besides the geometry, the electron density is also an important factor that affects the plasmon resonances of AuNRs, although not much attention has been paid to it. From Gans theory, one can derive the longitudinal plasmon wavelength of a nanorod as:

$$\lambda_{\text{plasmon}} = \lambda_p \sqrt{\varepsilon_\infty + \left(\frac{1}{L} - 1\right)\varepsilon_{\text{m}}} \qquad (1)$$

$$\lambda_{\text{p}} = \sqrt{\frac{2\pi^2 c^2 m^* \varepsilon_\infty}{Ne^2}} \qquad (2)$$

In eqn (1), ε_∞ is the high-frequency dielectric constant of gold, L is the depolarization factor along the length axis of the nanorods and ε_m is the dielectric constant of the surrounding medium . In eqn (2), c is the speed of light, m* is the electron effective mass in gold, e is the elemental charge, and N is the conduction electron density. The expressions above show clearly that the longitudinal plasmon wavelength of AuNRs can be strongly affected by the change in the electron density. An increase in the number of free electrons will result in a blue shift of the plasmon resonance due to the enhanced restoring force (Fig. I.20).

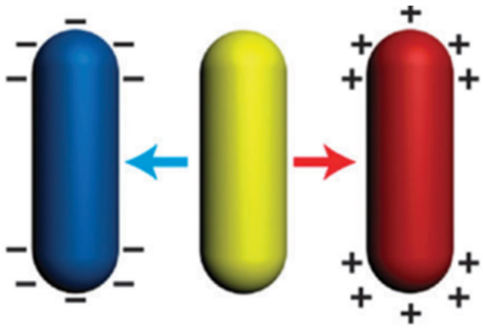

Fig. I.20. Schematic of charging of a single Au nanorod.

Mulvaney et al. have studied the effect of electron injection by adding reducing agents in Au nanorod solutions [56]. Addition of a reducing agent can introduce extra electrons to the nanorods, leading to blue shifts of the longitudinal plasmon resonance.

Refractive index-dependent plasmon resonance. The plasmon resonance of AuNRs is highly sensitive to the surrounding dielectric environment. This can be readily understood from eqn (1), which shows that the plasmon peak of AuNRs varies with $(\varepsilon_m)^{1/2}$. This dependence can be understood from a physics point of view. *Increase of the dielectric constant*, or in other words, the refractive index, of the environment surrounding the nanorod can induce more polarization charges around the nanorod. Under external electromagnetic excitation, there will be an increased screening of the Coulombic restoring force, that acts on the free electrons of the nanorod. The reduced restoring force therefore *results in a red shift in the plasmon resonance*. If we consider nanorods dissolved in solution, the simplest way to modify the environmental refravtive index is to change the ***solvent***. According to this, red-shift of plasmonic band the can be more clearly seen from the extinction spectra of AuNRs in solutions with different refractive indices (Fig. I.21) [56]

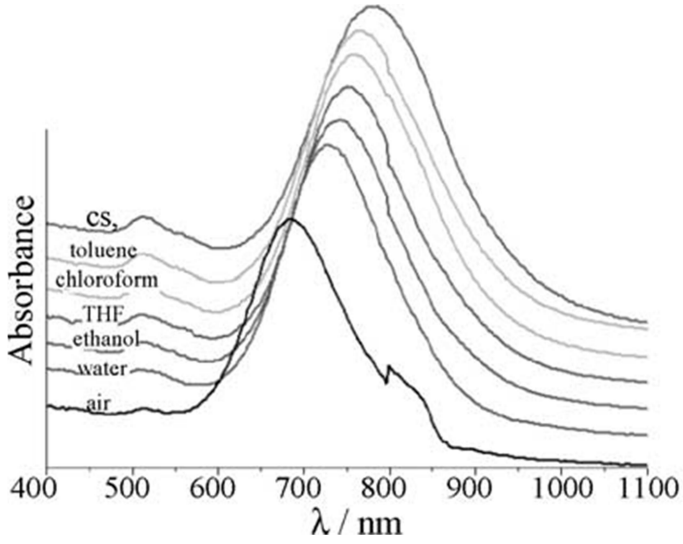

Fig. I.14. Longitudinal nanorods plasmon band position tuned by the solvent [56]

The longitudinal plasmon modes red-shift with increasing refractive indices. The plasmon shift of the longitudinal mode can be up to 120 nm for an increment of 0.4 in the refractive index. Furthermore, the longitudinal plasmon shift follows a linear relationship with the refractive index (Fig. I.22). This linear relationship has been corroborated by a number of experimental measurements [56].

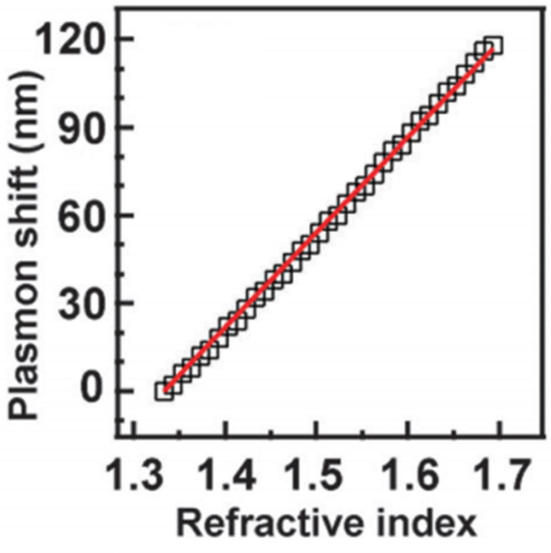

Fig. I.22. Dependence of the longitudinal plasmon shift on the refractive index of the solution

The refractive index-induced plasmon shift has received increasing attention due to its potential for designing ultrasensitive biomedical sensors [57] [58] [59]. One important parameter that determines the sensing performance of metal nanocrystal-based plasmonic sensors is the *refractive index sensitivity*, which is defined as the plasmon shift per refractive index unit. The extent of the red shift of the plasmon resonance is governed by the amount of the polarization charges, which is determined by the local electromagnetic field distribution around the nanocrystal and the polarizability of the nanocrystal. These two factors are the functions of the material and geometry of the metal nanocrystal. The index sensitivities of AuNRs were found [49] to generally increase as their plasmon wavelengths become longer. This finding indicates that the index sensitivities are generally larger for AuNRs with longer plasmon wavelengths. Such a characteristic can be ascribed to the fact that the dispersion of the real part of the dielectric function of gold is larger in the longer-wavelength region. Therefore, the plasmon shift will be larger for nanorods with longer plasmon wavelengths.

Longitudinal plasmonic band is tuned by ***capping agent*** too. It causes the shift of the plasmon resonance due to the local nature of its effect on the surface of the nanoparticle [56]. In particular, the plasmonic band of nanorods, with the same solvent, doesn't change position if covered with CTAB rather than PEG. Gold surface covered with molecules without a significant thickness is affected by the refractive index of the solvent. Different is the behaviour nanorods covered with SiO_2 capable of shielding the gold surface from the external environment. The silica thickness, that it is possible to control, influences the optical properties of nanorods. After coating with silica, the longitudinal LSPR peak of AuNR@SiO_2 solution red-shifts compared to AuNR@CTAB solution because refractive index of the mesoporous silica shell is higher (1.45) than refractive index of water (1.33). Increasing the thickness of the shell the longitudinal band shift towards low wavelength as shown in fig. I.23 [60].

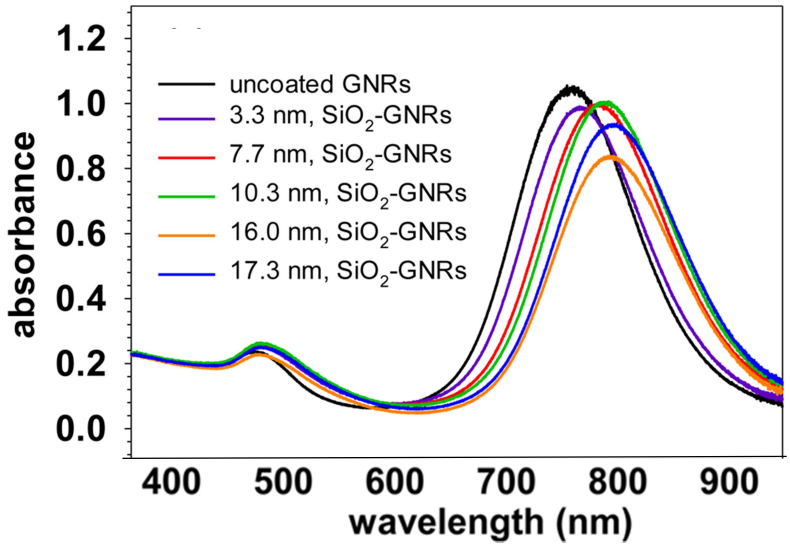

Fig. I.23. Extinction spectra of AuNR@SiO_2 with increasing shell thickness [33]

Plasmonic photothermal conversion. Decay of the plasmon resonances in Au nanocrystals through thermalization with the lattice will generate heat, which can thereby cause temperature rises in the surrounding environment. This ability of converting light into heat through the excitation of plasmonic resonances has made Au nanocrystals excellent candidates for killing cancer cells, [61] controllable gene release [62] and delivery of drugs [63]. AuNRs offer additional merits as photothermal conversion agents. Their plasmon wavelengths can be synthetically tuned into the near-infrared region where organic tissues show small light absorption [64]. Furthermore, compared with other light-absorption species, such as organic dye molecules, semiconductor nanocrystals, and spherical Au nanoparticles, AuNRs exhibit much stronger light absorption at their plasmon resonances [65]. Therefore, in recent years, studies of the photothermal conversion properties of AuNRs and their related applications have gained much interest.

The photothermal conversion efficiency of plasmonic metal nanocrystals is the most critical factor for photothermal conversion-based applications. As the photothermal conversion of metal nanocrystals is governed by the competition between the radiative and non-radiative decays of the plasmon resonance, the photothermal conversion efficiency is straightforwardly expected to be strongly dependent on the geometries and plasmonic properties of metal nanocrystals. Photothermal conversion will be highest for AuNRs with longitudinal plasmon wavelengths very close to the incident laser wavelength [66]. Under this condition, the incident laser can efficiently excite the plasmon resonance of the nanorods, through which its energy can be effectively converted into heat. Both experimental measurements and theoretical simulations have shown that the photothermal

conversion efficiency decreases as the particle volume of Au nanocrystals gets larger. Its origin is ascribed to the reduced radiative decay of the plasmon resonance in small nanocrystals, whereby the absorbed light energy is mainly converted into heat.

I.5. Plasmon coupling in assemblies of metal nanoparticles

When metal nanoparticles are close to one another, their surface localized plasmonic resonances are coupled through electrostatic interaction. The plasmon coupling, which causes an enhancement of the plasmonic field, opens opportunities for tailoring the applications of plasmonic materials [17]. The plasmon coupling has been found to be strongly dependent on the inter-particle spacing, but it is necessary to take into account the contribution of the nanoparticle coating agent. The coverage, infact, can modulate the plasmon field in different ways: it can drive the nanoparticles' assembling in a precise structural order [67] or avoid the plasmon interaction, increasing a lot the distance between nanoparticles. On this perspective, by using a tuneable coating agent like silica is possible to estimate the maximum distance between nanoparticles necessary for the plasmon interaction. [68]

Gold nanorods, for their anisotropic shape, can be assembled along two orientations: end-to-end or side-by-side, showed in Fig.I.24.

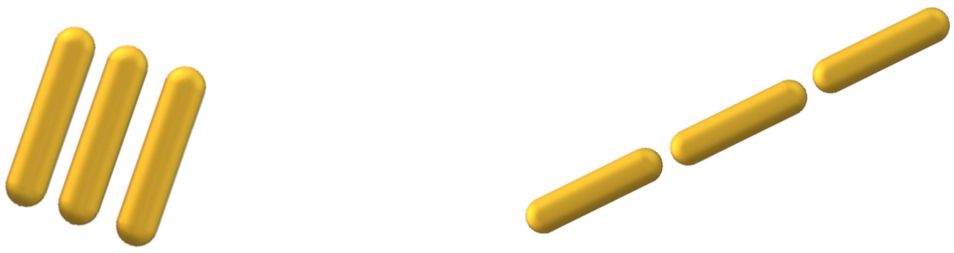

a) Side-by-side arrangement

b) End-to-end arrangement

Fig.I.24. End-to-end (a) and side-by-side (b) nanorods arrangement

The plasmon resonances carried by the two nanorods will interact to form different collective plasmon modes. The extinction spectrum of gold nanorods changes according to the assembling arrangement. Precisely, the longitudinal plasmon band is found to shift to lower energies for end-to-end assembly, instead, a shift to higher energies is found for the side-by-side orientation. The effectivness of the plasmon coupling increases with decreasing internanorod distance and an increase in the number of the interacting nanorods, as showed in Fig.I.25. For both side-by-side and end-to-end assemblies, the strength of the longitudinal plasmon coupling increases with increasing nanorod aspect ratio as a result of the increasing dipole moment of the longitudinal plasmon [69],

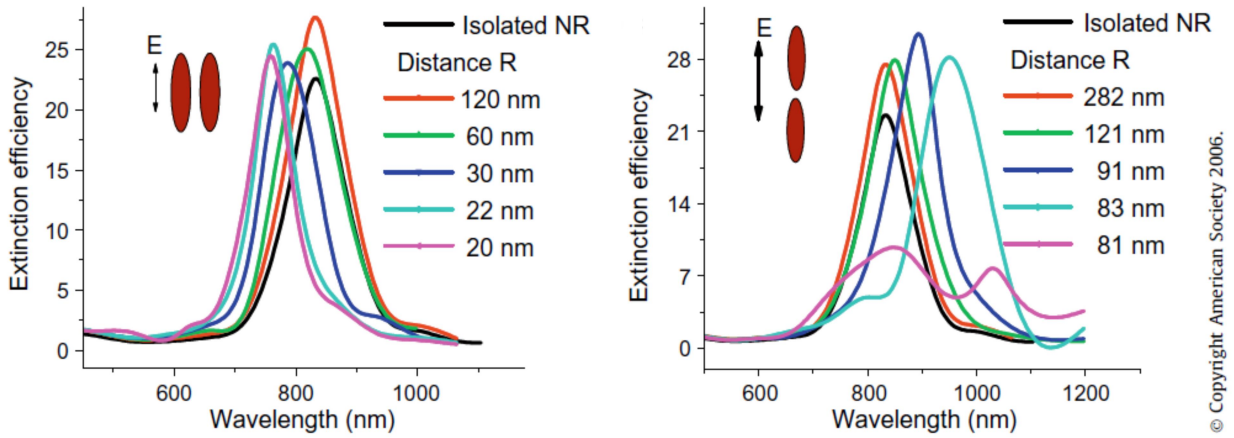

a) b)

b) **Fig.I.25.** Extinction spectra at different internanorod center-to-center distance of side-by-side arranged AuNRs (a) and end-to-end arranged AuNRs (b) [69].

The plasmon coupling of metallic nanoparticles is clearly detected in assembled nanospheres; in this case, a simple linear arrangement of nanospheres leads to the formation of a rod-like shape. From a spectroscopic point of view this implies the appearance of a new band at lower energy than typical nanospheres plasmonic band [Fig. I.26] [70]. In the case of metallic nanorods, an assembly of a couple of nanoparticles, is comparable to a single nanorod with a different aspect ratio: a greater aspect ratio is obtained in the case of an end-to-end arrangement; a lower in the case of a side-by-side. Consequently, in the extinction spectra of an end-to-end assembled AuNRs, longitudinal plasmonic band is red-shifted respect to the isolated AuNRs, while in a side-by-side assembled AuNRs this band appears blue-shifted.

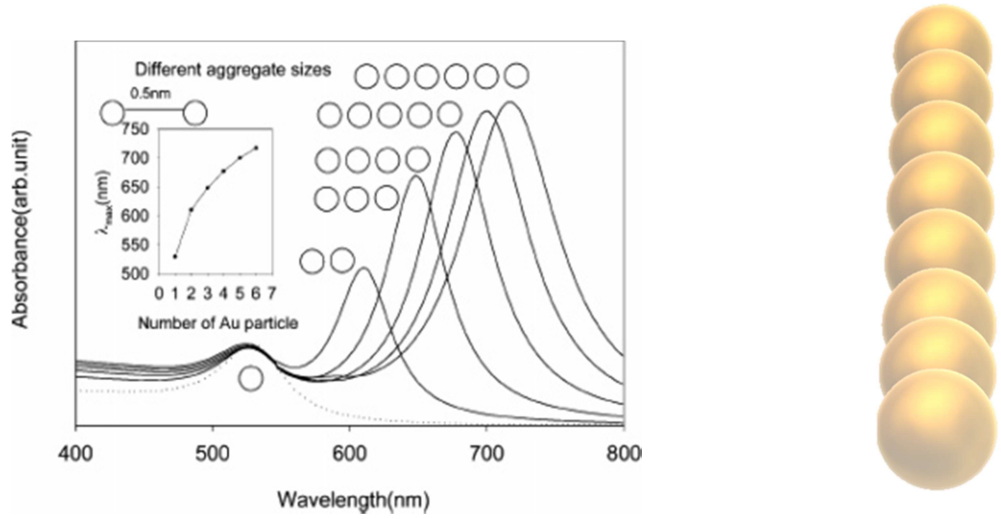

Fig. I.19. Linear assembling of gold nanospheres leads to a rod-like spectral behaviour

REFERENCES

1. a) E. Hao, G. Schatz and J. Hupp, J. Fluoresc., **2004**, 14, 331; b) K. L. Kelly, E. Coronado, L. L. Zhao and G. C. Schatz, *J. Phys. Chem. B*, **2003**, 107, 668
2. S. Eustis and M. A. El-Sayed, *Chem. Soc. Rev*., **2006**, 35, 209
3. a) C. Burda, X. Chen, R. Narayanan and M. A. El-Sayed, *Chem. Rev*., **2005**, 105, 102; b) Y. Xia, P. Yang, Y. Sun, Y. Wu, B. Mayers, B. Gates, Y. Yin, F. Kim and H. Yan, *Adv. Mater.*, **2003**, 15, 353–389; c) M. P. Pileni, *Nat. Mater*., **2003**, 2, 145; d) R. C. Jin, Y. W. Cao, C. A. Mirkin, K. L. Kelly, G. C. Schatz and J. G. Zheng, *Science*, **2001**, 294
4. a) C. J. Murphy, T. K. Sau, A. M. Gole, C. J. G. Orendorff, J. L. Gou, S. E. Hunyadi and T. Li, *J. Phys. Chem. B*, **2005**, 109; b) S. Link and M. A. El-Sayed, *J. Phys. Chem. B*, **1999**, 103, 8410; c) S. Link and M. A. El-Sayed, *Int. Rev. Phys. Chem*., **2000**, 19, 409; d) S. Link M. A. El-Sayed, *Annu. Rev. Phys. Chem*., **2003**, 54, 331
5. a) M. A. El-Sayed, Acc. *Chem. Res*., **2001**, 34, 257; b) S. Eustis, Mostafa A. El-Sayed, *Chem. Soc. Rev*., **2006**, 35, 209
6. a) J. A. Creighton, D. G. Eadon, *J. Chem. Soc., Faraday Trans*. **1991**, 87,3881; b) G. Schmid, *Chem. Rev*. **1992**, 92; c) A. Henglein, *J. Phys.Chem*. **1993**, 97, 5457; d) S. Nie, S. R. Emory, *Science*, **1997**, 275, 1102; e) V.Russier, M. P. Pileni, *Surf. Sci*. **1999**, 425, 313; f) N. R. Jana, T. K. Sau, T. Pal, J. *Phys. Chem. B,* **1999**, 103, 115; g) S. Link, M. A. El-Sayed, *J. Phys.Chem. B,* **1999**, 103, 8410
7. a) G. Frens, *Nature,* **1973**, 241, 20; b) D. G. Duff, A. Baiker, P. P. Edwards, *Langmuir,* **1993**, 9, 2301; c) M. T. Reetz, W. Helbig, *J. Am. Chem. Soc.,***1994**, 116, 7401; d) D. V. Leff, P. C. Ohara, J. R. Heath, W. M. Gelbart, *J. Phys. Chem*., **1995**, 99, 7036; e) J. H. Fendler, F. C. Meldrum, *Adv. Mater*., **1995**, 7, 607; f) Y. Volokitin, J. Sinzig, L. J. de Jongh, G. Schmid, I. I. Moi-seev, *Nature*, **1996**, 384, 621
8. a) T. S. Ahmadi, Z. L. Wang, T. C. Green, A. Henglein, M. A. El-Sayed, *Science*, **1996**, 272, 1924; b) J. M Petroski, Z. L. Wang, T. C. Green, M. A.El-Sayed, *J. Phys. Chem. B,* **1998**, 102, 3316; c) J. S. Bradley, B. Tesche, W. Busser, M. Maase, M. T. Reetz, *J. Am. Chem. Soc*., **2000**, 122, 4631
9. a) B. R. Martin, D. J. Dermody, B. D. Reiss, M. M. Fang, L. A. Lyon, M. J. Natan, T. E. Mallouk, *Adv. Mater*., **1999**, 11, 1021; b) B. M. I. van derZande, M. R. Bohmer, L. G. J. Fokkink, C. Schonenberger, *Langmuir,* **2000**, 16, 451
10. a) C. R. Martin, *Chem. Mater*., **1996**, 8, 1739; b) V. M. Cepak, C. R. Mar-tin, *J. Phys. Chem. B*, **1998**, 102, 9985; c) C. Schonenberger, B. M. I. vander Zande, L. G. J. Fokkink,

M. Henny, C. Schmid, M. Kruger, A. Bach-told, R. Huber, H. Birk, U. Staufer, *J. Phys. Chem. B,* **1997**, 101, 5497

11. a) J. Sloan, D. M. Wright, H. G. Woo, S. Bailey, G. Brown, A. P. E.York, K. S. Coleman, J. L. Hutchison, M. L. H. Green, *Chem. Commun*., 1999,699; b) T. Kyotani, L. F. Tsai, A. Tomita, *Chem. Commun*., **1997**, 701; c) A.Govindaraj, B. C. Satishkumar, M. Nath, C. N. R. Rao, *Chem. Mater*., **2000**, 12, 202; d) B. K. Pradhan, T. Kyotani, A. Tomita, *Chem. Commun*., **1999**, 1317
12. a) M. P. Pileni, T. Gulik-Krzywicki, J. Tanori, A. Filankembo, J. C. Dedieu, *Langmuir*, **1998**, 14, 7359; b) M. P. Pileni, B. W. Ninham, T. Gulik-Krzywicki, J. Tanori, I. Lisiecki, A. Filankem, *Adv. Mater*., **1999**, 11,1358; c) L. M. Qi, J. M. Ma, H. M. Cheng, Z. G. Zhao, *J. Phys. Chem*., *B* **1997**, 101, 3460; d) M. Li, M. H. Schnablegger, S. Mann, *Nature,* **1999**, 402,393; e) B. R. Heywood, S. Mann, *Adv. Mater*., **1994**, 6,9
13. a) B. R. Heywood, S. Rajam, S. Mann, *J. Chem. Soc., Faraday Trans*., **1991**,87, 735; b) D. Wash, S. Mann, Nature **1995**, 377, 320; c) J. D. Hopwood, S. Mann, *Chem. Mater*. ,**1997**, 9, 1819; d) G. D. Rees, R. Evans-Gowing,S. J. Hammond, B. H. Robinson, *Langmuir*, **1999**, 15, 1993; e) A. Filan-kembo, M. P. Pileni, *J. Phys. Chem. B*, **2000**, 104, 5865
14. a) M. Q. Zhao, L. Sun, R. M. Crooks, *J. Am.Chem. Soc*., **1998**, 120, 4877; b) M. J. Hostetler, J. E. Wingate, C. J. Zhong.J. E. Harris, R. W. Vachet, M. R. Clark, J. D. Londono, S. J. Green, J. J.Stokes, G. D. Wignall, G. L. Glish, M. D. Porter, N. D. Evans, R. W. Murray, *Langmuir,* **1998**, 14, 17; c) G. W. Busser, J. G. van Ommen, J. A. Lerch-er, *J. Phys. Chem. B*, **1999**, 103, 1651; d) T. Terani shi, M. Miyake, *Chem.Mater*., **1998**, 10, 594; e) T. Teranishi, M. Hosoe, T. Tanaka, M. Miyake, *J. Phys. Chem. B*, **1999**, 103, 3818
15. N. R. Jana, L. Gearheart, C. J. Murphy, *Chem. Mater*., **2001**, 13, 2313
16. M. Törnblm, U. Henrikesson, *J. Phys. Chem. B*, **1997**, 101, 6028
17. H. Chen, L. Shao, Q. Lia and J.Wang, *Chem. Soc. Rev*., **2013**,42, 2679
18. L.Scarabelli, M. Grzelczak, L. M. Liz-Marzán, *Chem. Mater.,* **2013**, 25, 4232
19. N. R. Jana, L. Gearheart, C. J. Murphy, *Adv. Mater*., **2001**, 13, 1389
20. P.D.Cozzoli, L.Manna, Synthetic Strategies to Size and Shape Controlled Nanocrystals and Nanocrystal Heterostructures in Bio-Application of Nanoparticles, *Springer*-Verlag New York, **2007**, 620,1
21. L.Scarabelli, M. Coronado-Puchau, J. J. Giner-Casares, J. Langer, L. M. Liz-Marzán, *ACS Nano*, **2014**, 8, 5833
22. Y. Xia, Y. Xiong, B. Lim, S. E. S. Angew, *Chem. Int. Ed*., **2009**, 48, 60

23. Zeliha Cansu Canbek. Crystal Engineering of Anisotropic Gold Nanoparticles through Modulation of Seed Size and Crystal Structure. Theoretical and/or physical chemistry. Université de Versailles-Saint Quentin en Yvelines, **2014**.
24. S. E. Lohse, N. D. Burrows, L. Scarabelli, L. M. Liz-Marzán, C.J. Murphy, *Chem. Mater.*, **2014**, *26*, 34
25. D. K. Smith, N. R. Miller, B. A. Korge, *Langmuir*, **2009**, 16, 9518
26. M.R.Langille, M.L.Personick, J. Zhang, C.A. Mirkin., *J. Am. Chem*. Soc. **2012**, 134, 14542
27. K. Park, H. Koerner, R. A. Vaia, *Nano Lett*., **2010**, 10, 1433
28. N. G. Bastus, J. Comenge, V. Puntes, *Langmuir*, **2011**, 27, 11098
29. S. E. Lohse and C. J. Murphy, *Chem. Mater*., **2013**, 25, 1250
30. L. Jiang, H. Mundoor, Q. Liu, I. I. Smalyukh, *ACS Nano*, **2016**, 10, 7064
31. A. B. Serrano-Montes, D. Jimenez de Aberasturi, J. Langer, J. J. Giner-Casares, L. Scarabelli, A.Herrero, L. M. Liz-Marzán, *Langmuir*, **2015**, 31, 9205
32. I. Pastoriza-Santos, J. Perez-Juste, L. M. Liz-Marzán, *Chem. Mater*., **2006**, 18, 2465
33. W. Wu and J. B. Tracy, *Chem. Mater*., **2015**, 27, 2888
34. M. Grzelczak, J. Vermant, E. M. Furst, L. M. Liz-Marzán, *ACS NANO*, **2010**,4, 3591
35. V. Sharma, K. Park, M.Srinivasarao, *Materials Science and Engineering*, **2009**,65, 1
36. N. R. Jana, L.A. Gearheart, S. O. Obare, C. J. Johnson, K.J. Edler, S. Mann, C. J. Murphy, *J. Mater. Chem*., **2002**, 12, 2909
37. C. Hamon, S. Novikov, L. Scarabelli, L. Basabe-Desmonts, L. M. Liz-Marzán, *ACS NANO*, **2014**, 8, 10694
38. L. Scarabelli, A. Sánchez-Iglesias, J. Pérez-Juste, L. M. Liz-Marzán, *J. Phys. Chem. Lett*. **2015**, 6, 4270
39. K. J. M. Bishop, C. E. Wilmer, S. Soh, B. A. Grzybowski, *Small,* **2009**, 5, 1600
40. P. Pramod, K. G. Thomas, Adv. Mater., **2008**, 20, 4300.
41. a) Z. Sun, W. Ni, Z.Yang, X. Kou, L. Li, J. Wang, *Small,* **2008**, 4, 1287; b) W. Ni, R.A. Mosquera, J. Perez-Juste, L. M. Liz-Marzán, *J. Phys. Chem. Lett*., **2010**, 1, 1181
42. Z. Nie, D.Fava, M. Rubinstein, E. Kumacheva, *J. Am. Chem. Soc*., **2008**, 130, 3683
43. a)K. Caswell, J. N. Wilson, U. H. F. Bunz and C. J. Murphy, *J. Am. Chem. Soc*., **2003**, 125, 13914; b) C. G. Wang, Y. Chen, T. T. Wang, Z. F. Ma and Z. M. Su, *Chem. Mater*., **2007**, 19, 5809; c) S. J. Zhen, C. Z. Huang, J. Wang and Y. F. Li, *J. Phys. Chem.C*, **2009**, 113, 21543; d) M. R. Jones, R. J. Macfarlane, B. Lee, J. Zhang, K. L. Young, A. J. Senesi, C. A. Mirkin, *Nat. Mater*., **2010**, 9, 913

44. Lacaze, E., Merchiers, O., Borensztein, Y. et al. *Rend. Fis. Acc. Lincei*, **2015**, 26(Suppl 2): 183
45. Y. Lia, E. Princea, S. Choa, A. Salarib, Y.Mosaddeghian Golestanic, O. D. Lavrentovichc, Eugenia Kumachevaa, *Proc Natl Acad Sci* U S A. **2017**, 114,2137
46. H. Qi, T. Hegmann, *Liquid Crystals Today*, **2011**, 20, , 102
47. D. Coursault, J. Grand, B. Zappone, H. Ayeb, G. Lévi, N. Félidj, E. Lacaze, *ACS Nano* 24, **2012**, 1461
48. B. Rožič, J.Fresnais, C. Molinaro, J. Calixte, S. Umadevi, S. Lau-Truong, N. Felidj, T.Kraus, F. Charra, V. Dupuis, T. Hegmann, C. Fiorini-Debuisschert, B. Gallas, E. Lacaze, *ACS Nano*, **2017**, 11, 6728
49. a) D. Lysenko, P. Pagliusi,C. Provenzano,Y. Reznikov, K. Slyusarenko, G. Cipparrone, Appl. Phys. Lett., 2013, 103, 151913; b) D. Kasyanyuk, P. Pagliusi.A. Mazzulla, V. Reshetnyak, Y. Reznikov, C. Provenzano,M. Giocondo, M. Vasnetsov, O. Yaroshchuk, G. Cipparrone, Scientific *Reports* 2016, 17, 20742
50. H. Chen, L. Shao, Q. Lia and J.Wang, *Chem. Soc. Rev*., **2013**,42, 2679
51. J. Perez-Juste, I. Pastoriza-Santos, L. M. Liz-Marzán, P. Mulvaney, *Coord. Chem Rev*, **2005**, 249, 1870
52. P. B. Johnson and R. W. Christy, *Phys. Rev. B: Solid State*, **1972**, 6, 4370
53. J. Zuloaga, E. Prodan and P. Nordlander, *ACS Nano*, **2010**, 4, 5269
54. C. Sonnichsen, T. Franzl, T. Wilk, G. von Plessen and J. Feldmann, *Phys. Rev. Lett*., **2002**, 88, 077402
55. a) X. S. Kou, W. H. Ni, C.-K. Tsung, K. Chan, H.-Q. Lin, G. D. Stucky and J. F. Wang, *Small*, **2007**, 3, 2103. b) H. J. Chen, L. Shao, K. C. Woo, T. Ming, H.-Q. Lin and J. F. Wang, *J. Phys. Chem. C*, **2009**, 113, 17691
56. a) C. Novo and P. Mulvaney, *Nano Lett*., **2007**, 7, 520; J. Perez-Juste, I. Pastoriza-Santos, L. M. Liz-Marzán, P. Mulvaney, *Coord. Chem. Rev.*, **2005**, 249, 1870
57. a) C. X. Yu and J. Irudayaraj, *Biophys. J*., **2007**, 93, 3684. b) C.-D. Chen, S.-F. Cheng, L.-K. Chau and C. R. C. Wang, *Biosens. Bioelectron*., **2007**, 22, 926. c) J. Burgin, M. Z. Liu and P. Guyot-Sionnest, *J. Phys. Chem. C*, **2008**, 112, 19279. d) Y. Khalavka, J. Becker and C. Sonnichsen, *J. Am. Chem. Soc*., **2009**, 131, 1871. e) H. J. Chen, X. S. Kou, Z. Yang, W. H. Ni and J. F. Wang, *Langmuir*, **2008**, 24, 5233
58. J. N. Anker, W. P. Hall, O. Lyandres, N. C. Shah, J. Zhao and R. P. van Duyne, *Nature Mater.*, **2008**, 7, 442.
59. K. M. Mayer and J. H. Hafner, *Chem. Rev*., **2011**, 111, 3828

60. L. Jiang, H. Mundoor, Q. Liu, I. I. Smalyukh, *ACS Nano*, **2016**, 10, 7064
61. a) E. B. Dickerson, E. C. Dreaden, X. H. Huang, I. H. El-Sayed, H. H. Chu, S. Pushpanketh, J. F. McDonald and M. A. ElSayed, *Cancer Lett*., **2008**, 269, 57. b) G. von Maltzahn, A. Centrone, J.-H. Park, R. Ramanathan, M. J. Sailor, T. A. Hatton and S. N. Bhatia, *Adv. Mater.*, **2009**, 21, 3175. c) J. Y. Chen, D. L. Wang, J. F. Xi, L. Au, A. Siekkinen, A. Warsen, Z.-Y. Li, H. Zhang, Y. N. Xia and X. D. Li, *Nano Lett*., **2007**, 7, 1318. d) A. M. Gobin, M. H. Lee, N. J. Halas, W. D. James, R. A. Drezek and J. L. West, *Nano Lett*., **2007**, 7, 1929.
62. a) S. E. Lee, G. L. Liu, F. Kim and L. P. Lee, *Nano Lett*., **2009**, 9, 562. b) C.-C. Chen, Y.-P. Lin, C.-W. Wang, H.-C. Tzeng, C.-H. Wu, Y.-C. Chen, C.-P. Chen, L.-C. Chen and Y.-C. Wu, *J. Am. Chem. Soc*., **2006**, 128, 3709
63. a) A. G. Skirtach, C. Dejugnat, D. Braun, A. S. Susha, A. L. Rogach, W. J. Parak, H. Mo¨hwald and G. B. Sukhorukov, *Nano Lett*., **2005**, 5, 1371. b) M. Bikram, A. M. Gobin, R. E. Whitmire and J. L. West*, J. Controlled Release*, **2007**, 123, 219. c) M. S. Yavuz, Y. Y. Cheng, J. Y. Chen, C. M. Cobley, Q. Zhang, M. Rycenga, J. W. Xie, C. Kim, K. H. Song, A. G. Schwartz, L. V. Wang and Y. N. Xia, *Nat. Mater*., **2009**, 8, 935
64. R. Weissleder, *Nat. Biotechnol*., **2001**, 19, 316
65. P. K. Jain, K. S. Lee, I. H. El-Sayed, *J. Phys. Chem. B*, **2006**, 110, 7238
66. H. J. Chen, L. Shao, T. Ming, Z. H. Sun, C. M. Zhao, B. C. Yang and J. F. Wang, *Small*, **2010**, 6, 2272
67. Z. Nie, D. Fava, M. Rubinstein, E. Kumacheva, *J. Am. Chem. Soc*., **2008**, 130, 3683-3689
68. S. Vial, I. Pastoriza-Santos, J. Pèrez-Juste, L. M. Liz-Marzán, *Langmuir*, **2007**, 3, 4606
69. P. K. Jain, S. Eustis, M. A. El-Sayed, *J. Phys. Chem. B **2006***, 110, 18243
70. S. K. Ghosh and T. Pal, *Chem. Rev.,* **2007**, 107, 4797

II. GOLD NANORODS SYNTHESIS

II.1 Gold nanorods covered with CTAB: synthesis, morphological and optical characterization

II.2 Playing with the gold nanorods surface: covering exchange and overcoating

II.3 Shape control of gold nanoparticles: nanotriangles and nanospheres

II.1 Gold nanorods covered with CTAB: synthesis, morphological and optical characterization

The growth of the AuNRs capped with CTAB (AuNR@CTAB) was conducted in aqueous environment using a seed-mediated method.

The *first step* is the preparation of the **seed solution:** the metal salt, tetrachloroauric acid ($HAuCl_4$), is mixed with CTAB. At this point sodium borohydride, ($NaBH_4$), a strong reducing agent, is added instantaneously under vigorous stirring. The metal reduction is complete (from $Au^{(III)}$ to $Au^{(0)}$). The colour of the solution become brown.

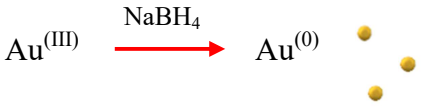

The *second step* is the preparation of the **growth solution**. It consists of water $HAuCl_4$ and CTAB solution mixed with a weak reducing agent, 5-bromosalicylic acid (5-BrSA), for the pre-reduction from $Au^{(III)}$ to $Au^{(I)}$. In this step, elongated micelles of CTAB are formed, that act as templating agents for the successive AuNRs growth. Here, no nucleation process takes place. According to Scarabelli *et al.* [1], by adding to a CTAB water solution 5-BrSa, as aromatic additive, it intercalates within the CTAB bilayer improving stiffness and symmetry of the growing particles. Furthermore, a water solution of silver nitrate ($AgNO_3$) is added to direct the anisotropic rod-like shape.

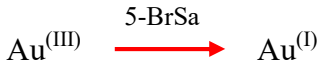

There is a correlation between the aspect ratio and the pre-reduction time. For shorter pre-reduction time (more $Au^{(III)}$ than $Au^{(I)}$ in solution) the aspect ratio value increases, for longer pre-reduction time (more $Au^{(I)}$ than $Au^{(III)}$ in solution) the aspect ratio value decreases. The longitudinal band shifts from red to blue with decreasing of the aspect ratio value. The pre-reduction of $Au^{(III)}$ to $Au^{(I)}$ is monitored following the drop in absorbance at 396 nm band of $Au^{(III)}$ (Fig.II.1).

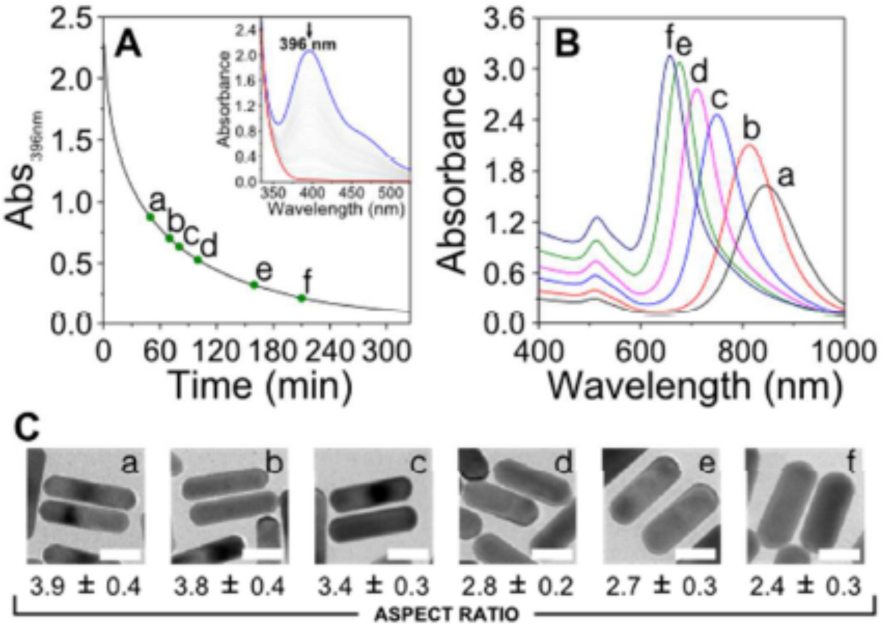

Fig. II.1. A) Kinetic study of the pre-reduction step (inset: full UV−vis spectra), B) Extinction spectra of Gold Nanorods with different aspect ratios, correlated with TEM images in C) [1]

The *third step* consists in mixing the seed solution with growth solution by adding, at a defined pre-reduction time, a second weak reducing agent, *i.e.* ascorbic acid (AA). In this step, disporoportion reaction: $3Au^{+} \rightarrow 2\,Au(0) + Au^{3+}$ occurs onto the metal surface; the resulting Au^{3+} ions were reduced by ascorbic acid to Au^{+} , driving the reaction, and, in this way, the nanorods growth continues.

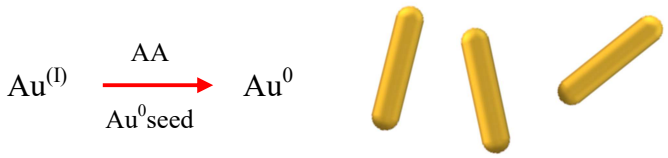

This bimodal reducing agent system consisting of the combination of salicylic acid and ascorbic acid allows a good gold reduction control at any stage of nanorod formation, achieving an improvement on morphology control. [1]

The *fourth step* consists of a centrifuge purification to eliminate unreacted reagents, prior to check the optical features. In particular, by measuring the absorbance at 400 nm, which corresponds to the interband transition of the metallic gold, it can determined the amount of $Au^{(0)}$ regardless of particles size and shape [2]. In this way, by taking into account the metallic gold density and the

average volume of nanoparticles (calculated by TEM images), it is possible to estimate the AuNRs molar concentration.

Preparation of the seed solution. 25 µL of 5.0E-2 M $HAuCl_4$ water solution was added to 4.7 mL of 0.1 M CTAB water solution, 300 µL of a freshly prepared 1.0E-2 M $NaBH_4$ water solution was then injected under vigorous stirring. Excess borohydride was consumed by keeping the seed solution for 30 min at room temperature prior to use (Fig. II.2)

Fig. II.2. The seed solution

Preparation of the growth solution. 45 mg of 5-BrSA was added to 50 mL of 0.05E-2 M CTAB water solution. After complete dissolution, 480 µL of 1.0E-2 M $AgNO_3$ water solution was added. The solution was mildly stirred for 15 min at room temperature, and then 500µL of 5.0E-2 M $HAuCl_4$ water solution was added to the mixture, starting the pre-reduction step.

Final step. At the selected pre-reduction time, 130 µL of 0.1 M AA water solution was added under vigorous stirring, followed by 80 µL of seed solution. After 30 s, the stirring was stopped and the mixture was left undisturbed at room temperature for at least 4 h (Fig. II.3). The sample were finally centrifuged (9000 rpm, 20 min, 30 °C).

Fig. II.3. Gold nanorods colloidal solution

Morphological and optical characterization. Fig. II.4 reports the results obtained following the illustrated synthetic protocol. The pre-reduction time was fixed when the absorbance at 397 nm was measured around 0.8, and then AA was added, obtaining AuNR@CTAB with longitudinal plasmonic peak at 794 nm, transversal plasmonic peak at 513 nm, and aspect ratio=4 (calculated from TEM images). TEM images show nanoparticles homogeneous in shape and size. The extinction spectrum in solution confirms this: more the longitudinal band is symmetric (with a limited broadening) more the sample is homogeneous. [2]

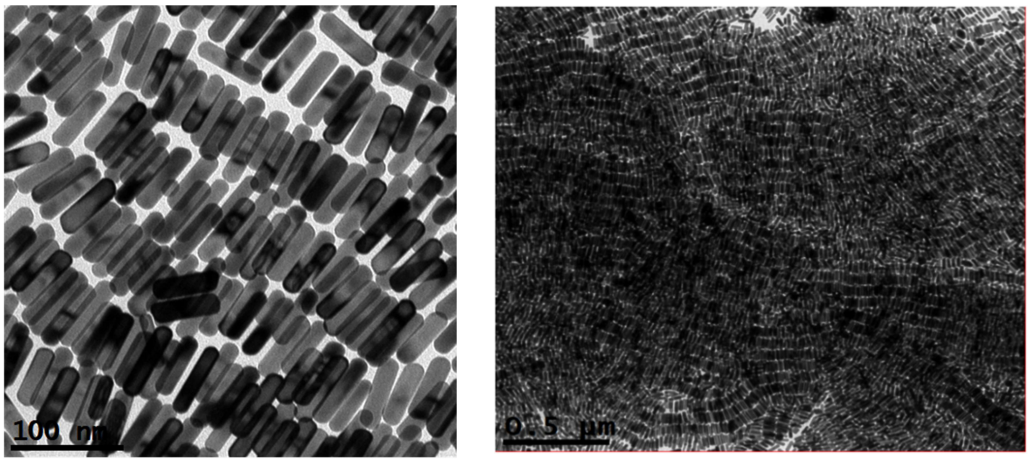

(a) (b)

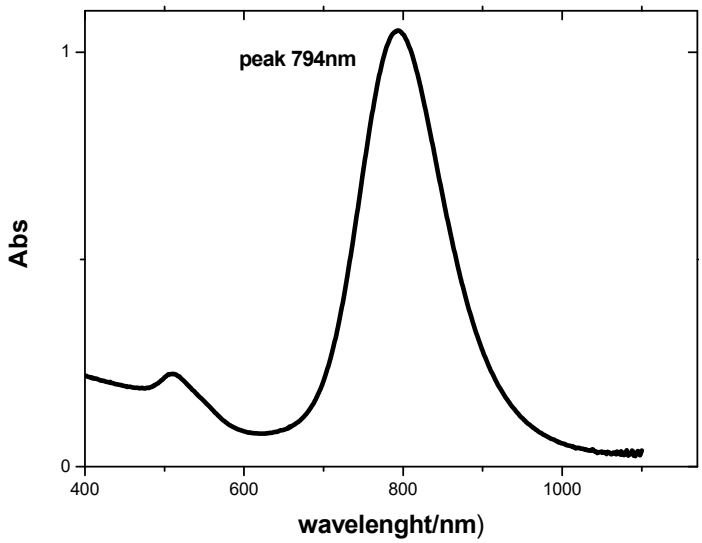

(c)

Fig. II.4. TEM images (a), (b) and extinction spectrum (c) of AuNR@CTAB prepared according to the illustrated protocol (Abs_{397} = 0.8).

Increasing the pre-reduction time, by adding ascorbic acid when the absorbance at 397 nm is around 0.7, the aspect ratio of AuNR@CTAB decreases from 4 to 3.3 and, consequently, the longitudinal band blue shifts from 794 nm to 766 nm (Fig. II.5).

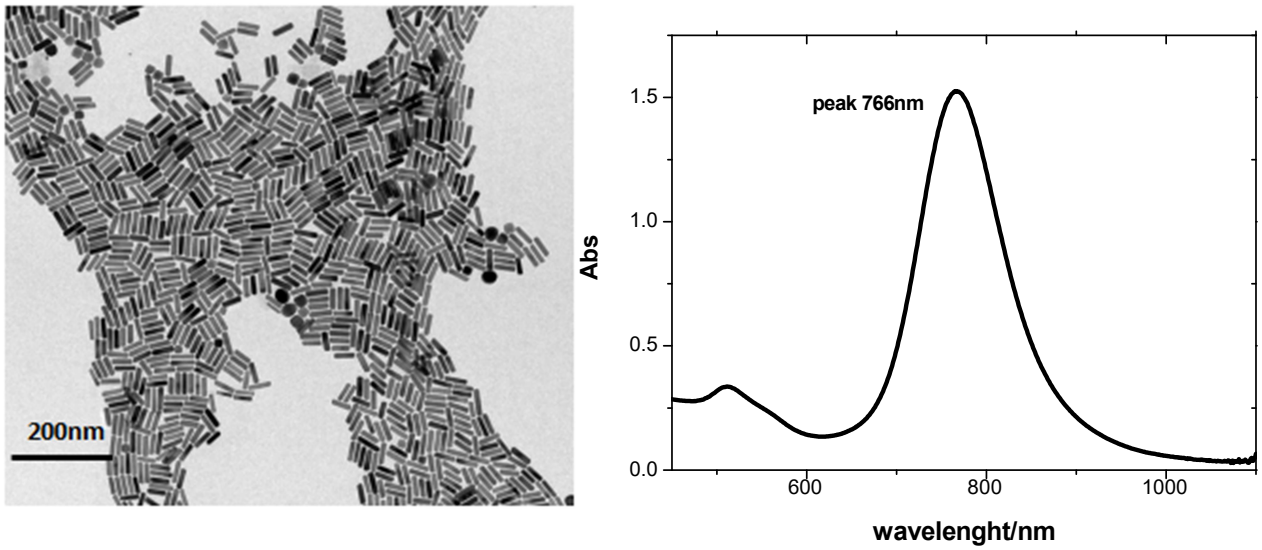

(a) (b)

Fig. II.5. TEM images (a), (b) and extinction spectrum (c) of AuNR@CTAB prepared according to the illustrated protocol (Abs_{397} = 0.7)

A fine control of the aspect ratio. Beside the pre-reduction time control, another way to modulate the aspect ratio of nanorods is to variate the amount of ascorbic acid and seed solution when $Au^{(III)}$ is completely reduced to $Au^{(I)}$ (the growth solution became colourless). In Fig. II.6 are reported two exempla of the obtained AuNR@CTAB achieved by adding 35 μL or 95 μL of ten time diluted seed solution to 25 μL of AA 0.01 M and 2.5 mL of growth solution. The aspect ratio is 3.0 in the first case and 3.8 in the second, while a relevant red-shift of the longitudinal band is observed by comparing the two samples.

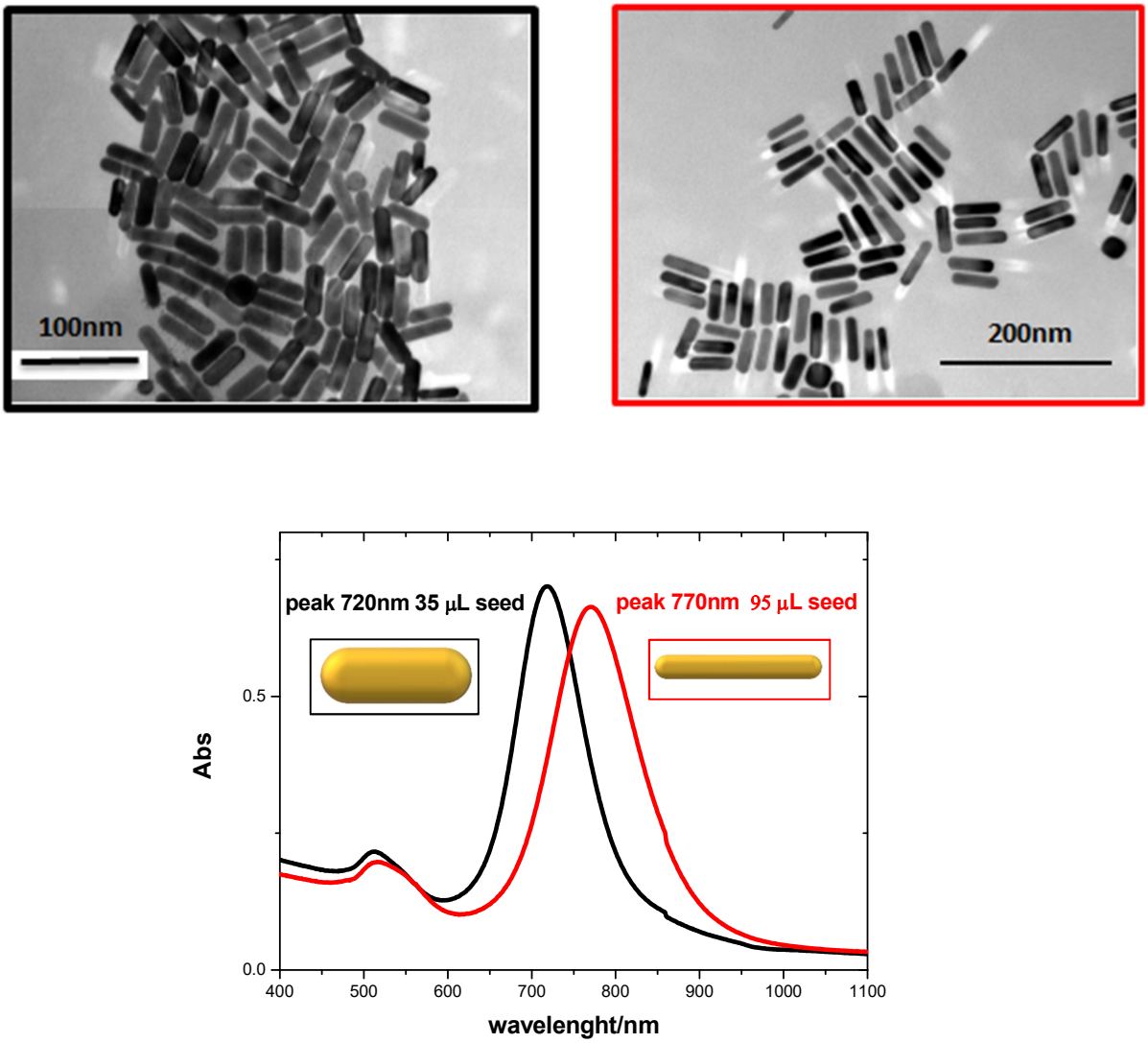

Fig. II.6. AuNR@CTAB obtained by adding different amount of seed solution (35 µL, black board; 95 µL red board) to growth solution, when pre-reduction is completed

A more fine aspect ratio control, has been reached by varying in a narrower range the seed amount, as reported in Fig. II.7. The extinction spectra show that increasing the amount of seed solution the longitudinal plasmonic peak shifts from 754 nm to 781 nm, with consequent increasing of the aspect ratio.

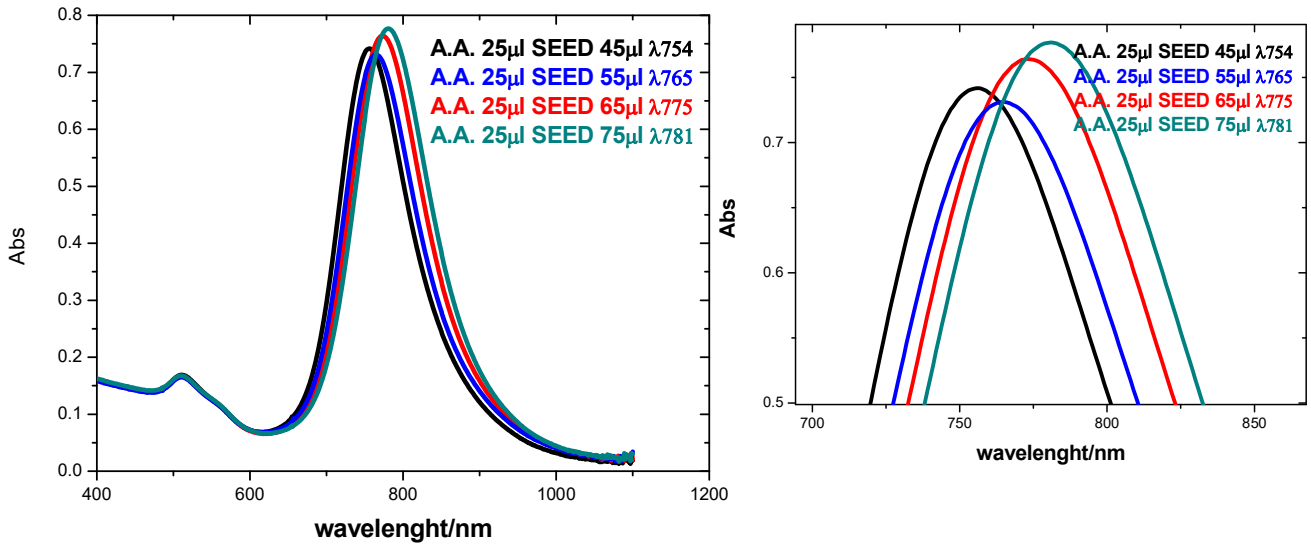

Fig. II.7. Extinction spectra obtained by varying the AA/seed solution ratio in a narrower range. On the right, a zoom of the peaks is reported

Role of CTAB and $AgNO_3$ concentration in AuNR@CTAB synthesis. We reproduced the previous procol modifying CTAB and $AgNO_3$ concentrations, in order to investigate their contribution in the formation of the shape like rod. In particular, reducing the CTAB concentration of the growth solution from 0.05M to 0.025M, nanorods with high polydispersity are formed, as shown in the TEM image below (Fig. II.8)

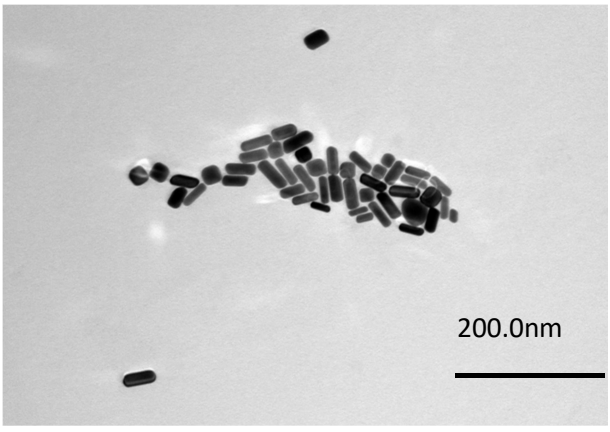

Fig.II.8. TEM image of AuNR@CTAB with high polydispersity

Regards to the $AgNO_3$, we evidenced that by reducing its amount, elongated shape of nanoparticles are formed, similar to bipyramids (Fig. II.9.a), while, if $AgNO_3$ is absent, various shapes are observed (Fig.II.9.b).

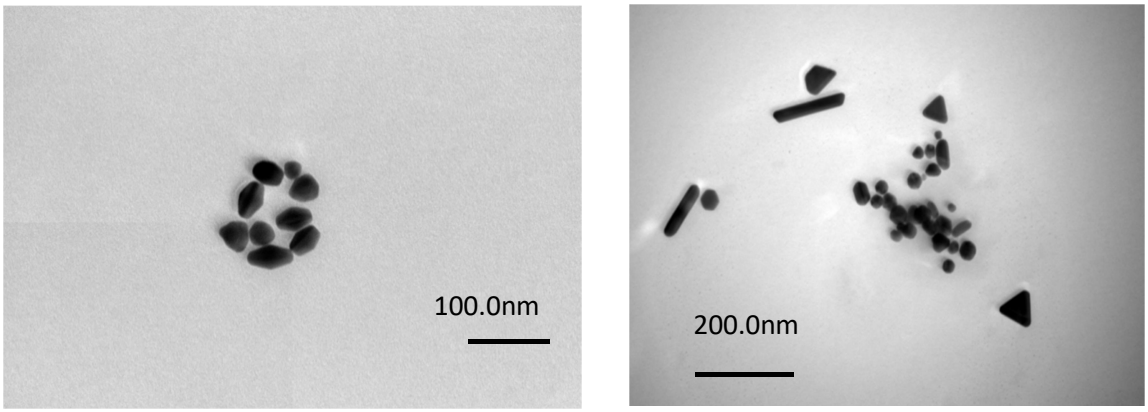

a) b)

Fig.II.9. TEM image of gold bypiramids (a); TEM image of gold nanoparticles with various shape (b)

Final remarks. According to morphological and photophysical analysis, AuNR@CTAB shown above are homogeneous in shape and size. The longitudinal band is symmetric with a FWHM value around 100 nm, and, according to the literature [2], these parameters are indicative of the homogeneity of the product. In order to obtain a good sample (homogeneous without by-products), many factors have to be considered. The quality of the water supply used for the synthesis is one of the main sources of irreproducibility. Milli-Q water should be deionized and filtered but not distilled. As a consequence, the presence of contaminant traces cannot be excluded. Mass spectrometry is an appropriate tool to check water quality, and HPLC-grade water can be purchased as a quality standard. Another important water-related parameter is pH, which can dramatically influence the aspect ratio of your nanorods. It should be noted that pH may be different even after Milli-Q purification, meaning that reoptimization may be required, typically through systematic tuning of $AgNO_3$ concentration [2].

High-quality seed solution is necessary to obtain high-quality nanorods. Ideally, the seeds should be monodisperse and display the same crystallographic habit, which in practice is achieved by adding a strong reducing agent in excess as fast as possible and under vigorous stirring. If the seed are not monodisperse the transversal band will be broadened (Fig. II.10) for the presence of by-products (such as spheres or cubes) into the sample.

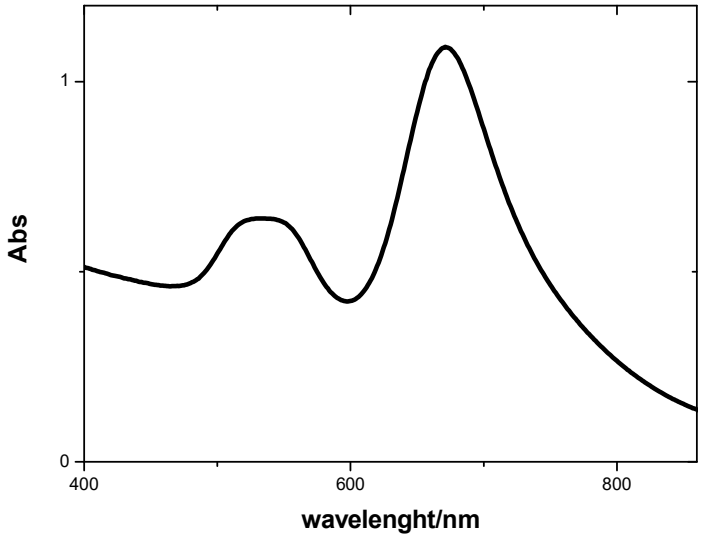

Fig. II.10. Extinction spectrum of an AuNR@CTAB sample with the presence of by-products derived from a inhomogeneities of the seed size

In some case, the longitudinal band appears broadened (Fig. II.11); this is due to a different size of nanorods in solution. By centrifugation it is possible separate nanorods by size: the heavier will be on the bottom of the tube, the smaller in the supernatant. The separation it is generally achieved centrifuging at 4500 rpm for 10 minute.

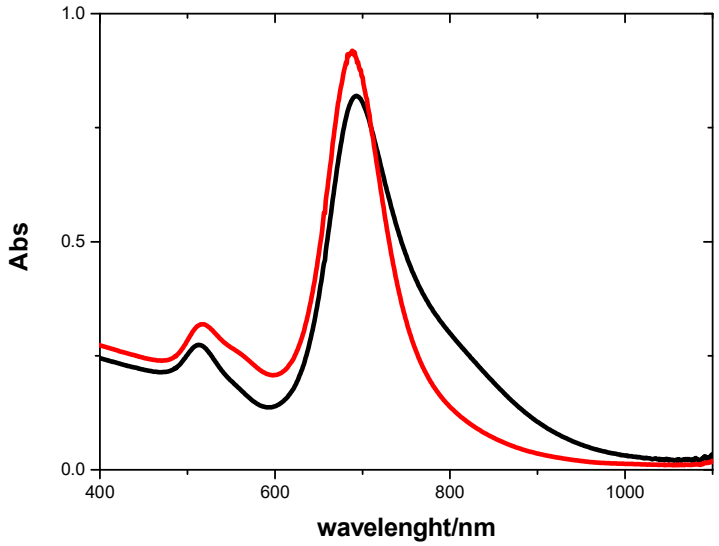

Fig. II.11. Extinction spectra of NR@CTAB before (black line) and after (red line) centrifugation

II.2 Playing with the gold nanorods surface: covering exchange and overcoating

Gold nanorods functionalization (§ I.3) modulates their solubility, making nanoparticles soluble in a wide range of solvents, depending on its chemical nature. From this point of view, in order to take advantage of the tunable "surface chemistry", we synthesized, in addition to AuNR@CTAB, AuNRs covered with various caoting agents.

AuNRs@PEG-SH. Because AuNR@CTAB are soluble exclusively in water, to manage AuNRs in other solvent, we changed CTAB capping with thiol-functionlised poly(ethylene glycol), PEG-SH, modifying the protocol reported in the reference [3]. We solubilized 30 mg of O-(2-Mercaptoethyl)-O′-methylpolyethylene glycol (2000 Mn) in 1 mL of water, and added this solution to 50 mL of AuNR@CTAB water dispersed, with a concentration 0.5 E-3 M. The solution was left under stirring overnight. The day after we centrifuged the sample and dissolved the solid residue in methanol to have evidence of the exchange. (AuNR@CTAB are not soluble in methanol). As expected, the great affinity of the thiol group toward gold surface drives the substitution of the CTAB cover with PEG-SH.

Moreover, we dissolved the solid residue in other solvents, such as water and chloroform. Fig. II.12 shows the TEM image of AuNR@PEG-SH and the extinction spectra of the samples before and after the exchange in the used solvents.

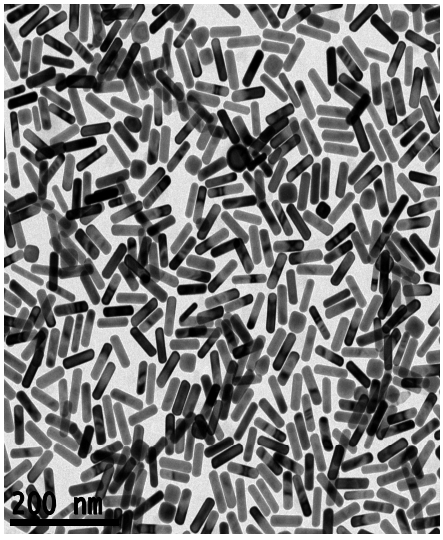

(a)

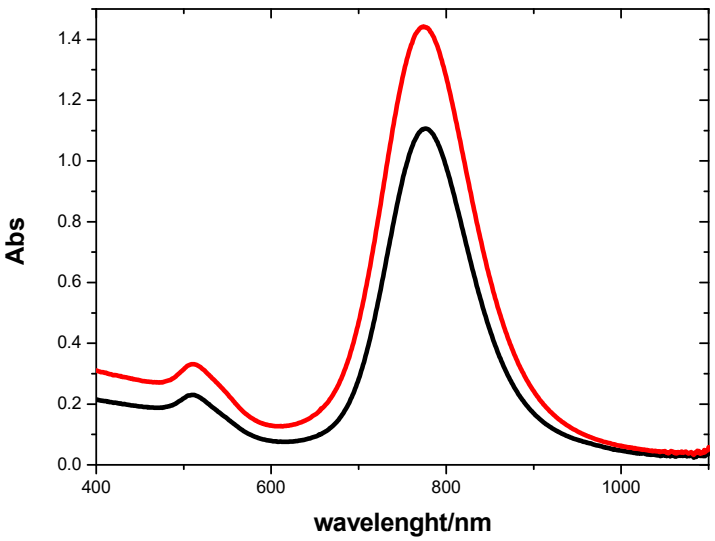

(b)

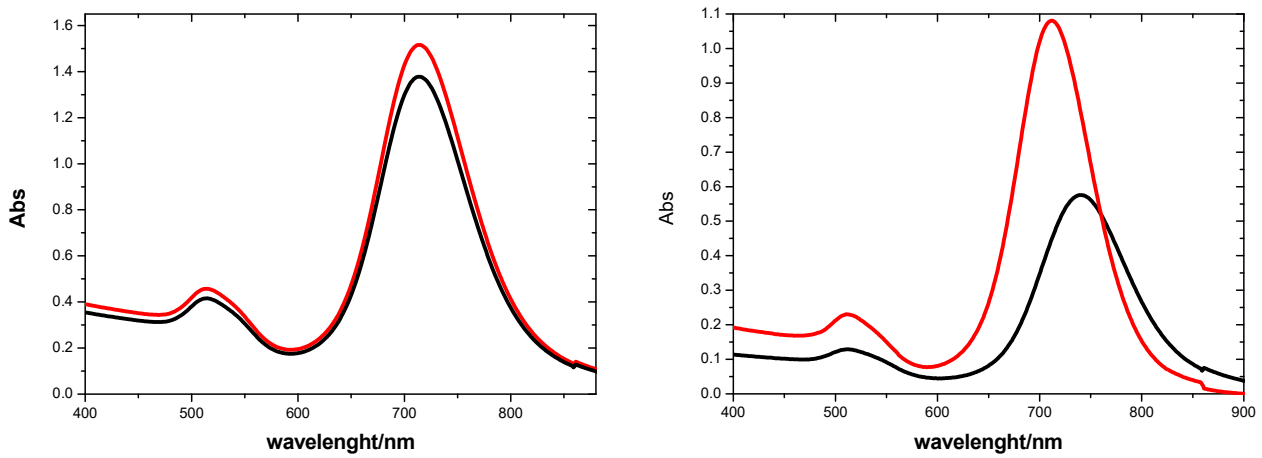

Fig. II.12. (a) TEM image of AuNR@PEG-SH; (b) extinction spectra of AuNR@CTAB in water (black line) and of AuNR@PEG-SH in methanol (red line); (c) extinction spectra of AuNR@CTAB in water (black line) and of AuNR@PEG-SH in water (red line); (d) extinction spectra of AuNR@CTAB in water (black line) and of AuNR@PEG-SH in chloroform (red line) .

By comparing the spectra, we note that the transversal band appears unvaried (fixed at 514 nm) by changing both solvent and coating, while the longitudinal band is almost unvaried by changing the coating in the same solvent (712 nm in fig. II.10.c), whereas this bands in AuNR@PEG-SH is red-shifted from methanol and water to chloroform, passing from 712 to 742 nm, following the increasing of the solvent refractive index (n_d^{20} =1.32 for MeOH; n_d^{20} =1.33 for water; n_d^{20} =1.44 for chloroform).

AuNRs@PEG-SH_DDT. We overcoated AuNR@PEG-SH with dodecanethiol (DDT) to improve their stability in chloroform. Because a substitution of the polymeric PEG-SH coating with a small molecule such as DDT could induce AuNRs aggregation (§I.3), a better way is doping the AuNR@PEG-SH with DDT [4].

We added 5 mL of a 0.1E-3 M DDT chloroform solution to a 5 mL of an aqueous solution of AuNR@PEG-SH 0.4E-3 M. Two phases were formed: water phase containing nanorods on the top and chloroform phase containing DDT on the bottom. Nanoparticles were transferred from water to chloroform after vigorous stirring: slowly, the water solution loses the pink colour while the organic phase become pink, due to the nanorods migration (Fig. II.13). The transfer, completed in an hour, was assisted by addition of concentrated HCl. Upon transfer to $CHCl_3$, the organosols were purified by centrifugation and washing to remove free DDT. Fig.II.14 show extinction spectrum in chloroform, and TEM of AuNR@PEG-SH_DDT. The position of transversal and

longitudinal plasmonic bands does not change compared to the spectrum of AuNR@PEG-SH in chloroform as shown in Fig. II.12 (d), as expected, because the solvent is the same in both samples.

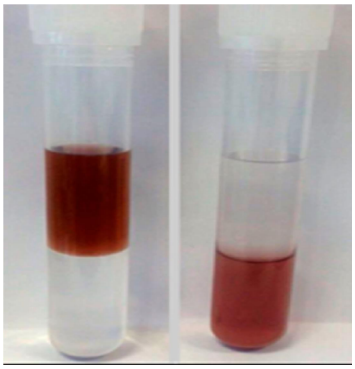

Fig. II.13. AuNRs from water (upper phase) into a solution of DDT in chloroform (lower phase)

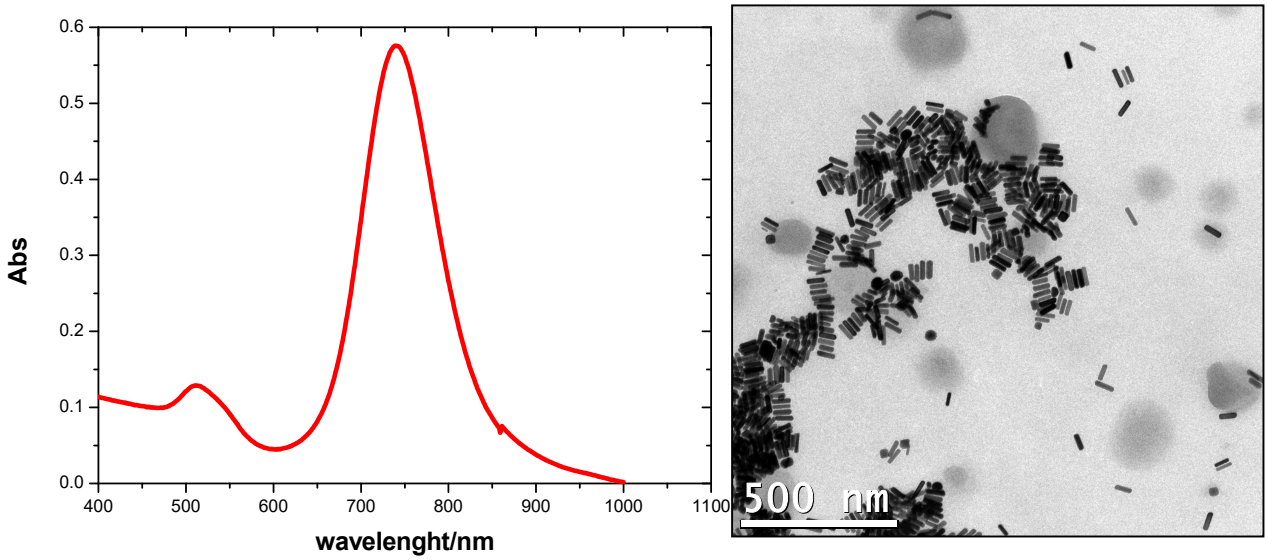

(a) (b)

Fig. II.14. AuNR@PEG-SH_DDT: (a) extinction spectrum in chloroform; (b) TEM image.

AuNR@L1. In order to study the AuNRs behaviour in liquid crystalline medium (4-Octyl-4'-Cyanobiphenyl, Fig. II.15.a) we covered AuNRs with a thiol-functionalised aromatic compound with a long tail (L_1 in Fig. II.13.b), soluble in the used liquid crystal. Similarly, in this case the great affinity of the thiol group toward gold surface drives the substitution of the CTAB cover.

We prepared 0.1 E-3 M solution of L_1 in THF (solution A), and a second solution 0.1 E-2 M of L_1 in chloroform (solution B). 5 mL of A were added to 5 mL of aqueous solution of AuNR@CTAB 1E-4 M under sonication. The AuNR@CTAB colour changed to pink. After 5

minutes of sonication we centrifuged the sample, and the solid residue were washed with acetone by centrifugation to eliminate THF residue. The precipitate were redispersed in chloroform solution B. Fig. II.16 shows the TEM image of the obtained AuNR@L_1 and the extinction spectra of the samples before and after the cover exchange.

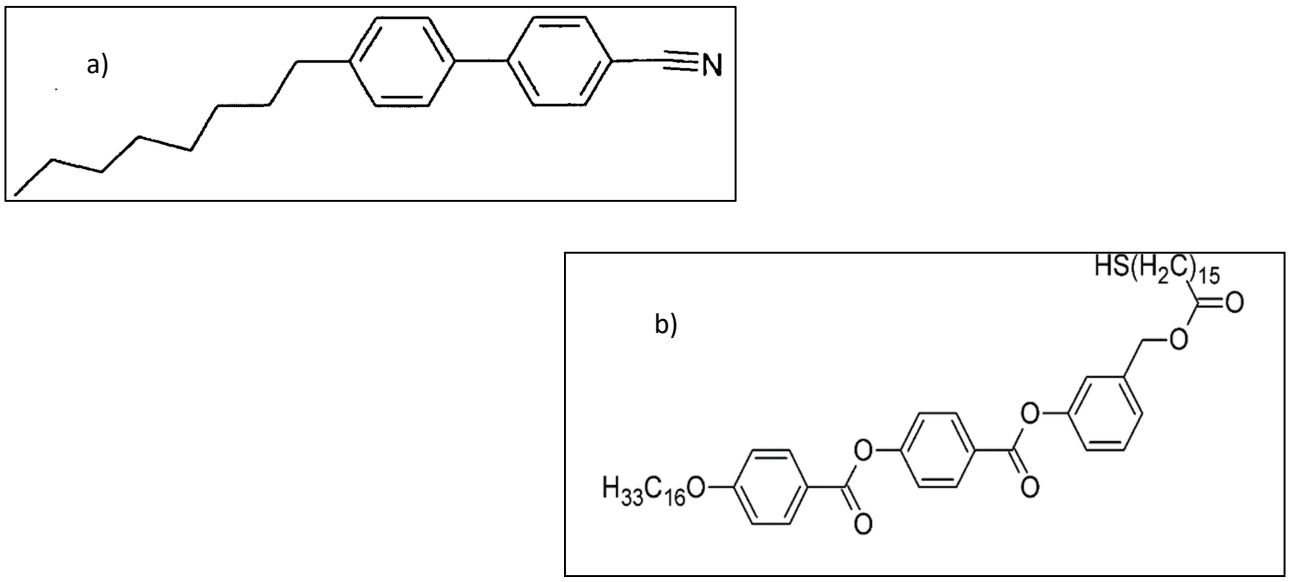

Fig. II.15. 4-Octyl-4'-Cyanobiphenyl (a) and L_1 (b) molecular structures.

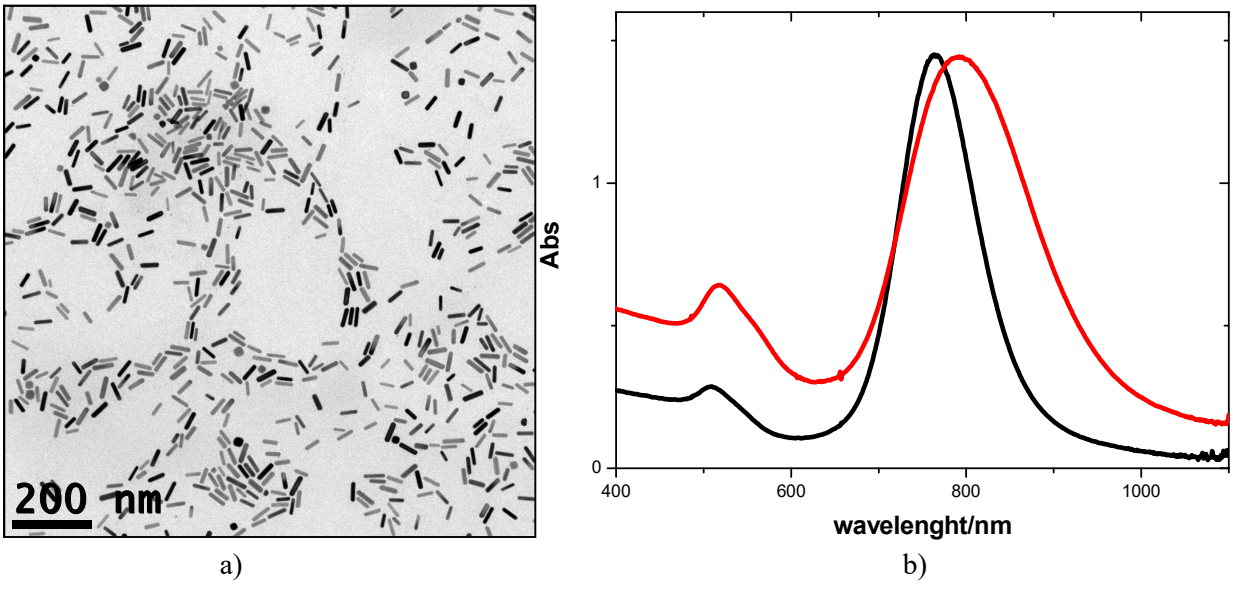

a) b)

Fig. II.16. (a) TEM image of AuNR@L_1; (b) extinction spectra of AuNR@CTAB in water (black line) and of AuNR@L_1 in chloroform (red line)

By comparing the spectra, longitudinal band redshifted after the change of both solvent and coating,passing from 765 nm to 792 nm, while the transversal band appears unvaried (fixed at 514 nm).

II.3 Shape control of gold nanoparticles

NANOTRIANGLES

The **seed-mediated growth method** is a tunable synthetic strategy for metal nanoparticles, in fact, less changes of the protocol translate into important differences in the morphology of the nanoparticles. [5] To this end, small variations introduced in the AuNR@CTAB synthetic protocol, allow to obtain gold nanotriangles (NTs).

The synthesis of gold nanotriangles covered with CTAC (AuNTs@CTAC), based on the seed-mediated method, was conducted in aqueous environment. The followed protocol [6] involves three consecutive steps.

The *first step* is the preparation of **seed solution**. The only change compared to seed solution used for AuNRs is the presence of CTAC instead of CTAB as covering of gold seed.

The *second step* consists in the preparation of **two growth solutions**, one (A) used to grow the CTAC-capped seeds into larger nanoparticles, while the second (B) used as the NTs growth batch. The metal salt reduction ($HAuCl_4$) takes place on the surface of the gold seeds with AA contribution. A water solution of sodium iodide (NaI) is added to the second solution to direct the anisotropic triangular shape.

The *third step* is the purification by addition of a selected amount of 25 wt % CTAC solution.

Preparation of the seed solution. 25 μL of 5.0E-2 M $HAuCl_4$ water solution was added to 4.7 mL of 0.1 M CTAC water solution, 300 μL of a freshly prepared 1.0E-2 M $NaBH_4$ water solution was then injected under vigorous stirring. Excess borohydride was consumed by keeping the seed solution for 30 min at room temperature prior to use (Fig. II.17)

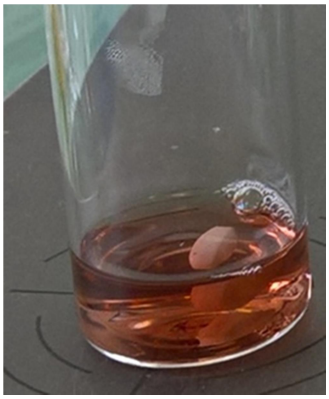

Fig. II.17 The seed solution

Preparation of the growth solution. **Solution A**: 6.4 mL of CTAC 0.1 M were added to 32 mL of Milli-Q water, followed by 160 µL of 5.0 E-2 M $HAuCl_4$ solution. **Solution B**: 313 mL of CTAC 5.0 E-2 M were added to 3.91 mL of 5.0 E-2 M $HAuCl_4$ solution, followed by 2.35 mL of 0.1 E-2 M NaI water solution. We shaked the solutions by hand after each addition. Then, 160 µL and 3.13 mL of 0.1 M AA solution were added to solutions A and B, respectively, and both solutions were manually stirred until a complete transparency of the solutions was achieved, indicating $Au^{(III)}$ to $Au^{(I)}$ reduction. Finally, 400 µL of ten times diluted seed solution was added to solution A. At this point, solution A was added to solution B. The AuNT@CTAC dispersion was left undisturbed at room temperature for 2 h. The colour, initially strongly pink, soon turns into purple. As reported in literature, the purple solution contains nanoparticles with different shape (cubes, spheres, nanotriangles). For this reason, the product of the synthesis needs to be purified by adding an amount of water CTAC solution (93.3 mL of 25 wt % CTAC solution), which triggers AuNTs flocculation; it was completed after two hours, the supernatant was then removed and the precipitated particles were redispersed in 5.0 E-2 M CTAC solution, obtaining AuNT@CTAC blue solution (Fig. II.18).

Fig.II.18 AuNT@CTAC purified colloidal solution

Morphological and optical characterization. Fig. II.19 reports the results obtained following the illustrated synthetic protocol. The extinction spectra of AuNT@CTAC present a principal plasmonic peak at 620 nm; in particular, Fig. II.19.a reports the spectrum prior purification showing a shoulder at 520 nm, for the presence of byproducts in solution. After purification (fig. II.19.b), the shoulder is much less visible, attesting the homogeneity of the sample in shape and size. This aspect is confirmed by TEM image (fig. II.19.c), which allow to measure an average NTs length of 50 nm.

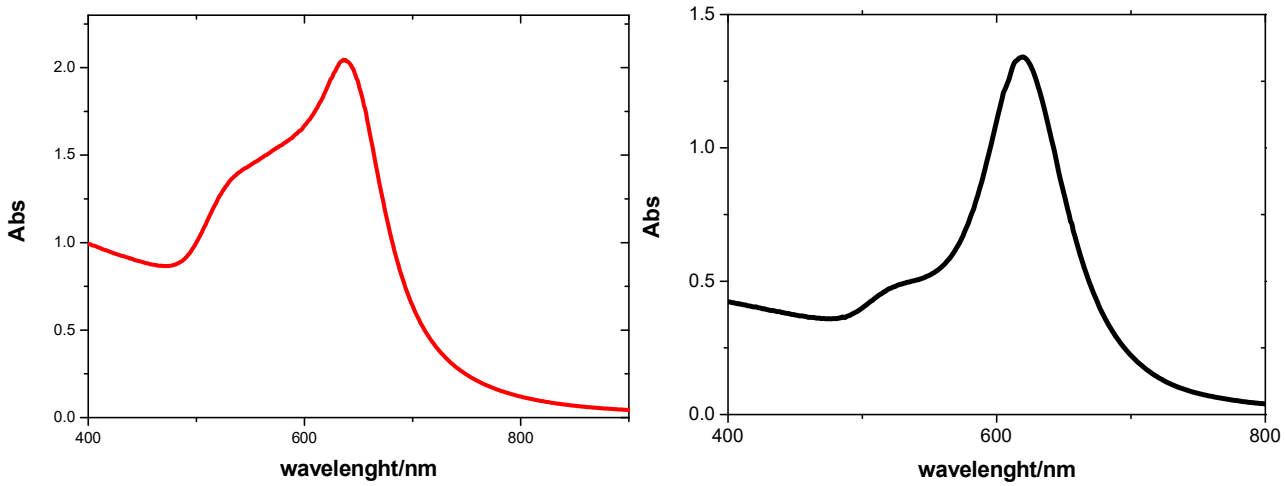

a) b)

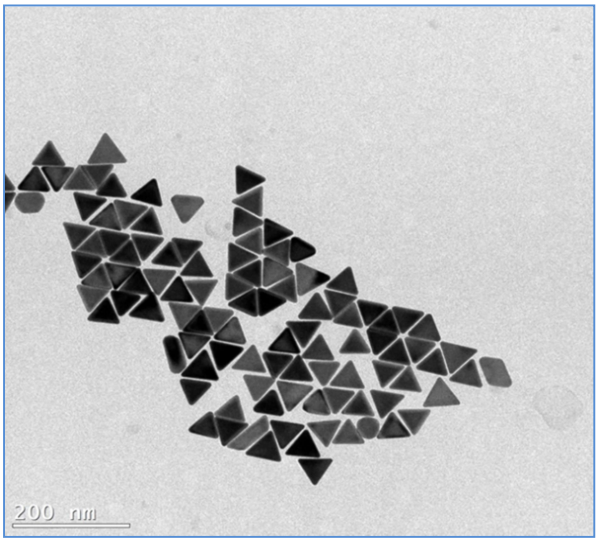

c)

Fig II.19. Extinction spectra of AuNT@CTAC water solution, prior purification (a) and after (b). TEM image of the purified NTs.

NANOSPHERES

Following the seeded growth strategy, [7] we synthesized gold nanospheres covered with sodium citrate (AuNS@SC) and dispersed in water, according to the steps sketched in Fig. II.20

The first step is the **seed formation:** a water solution of sodium citrate, in a 250 mL three-necked round-bottomed flask, was heated with a heating mantle and stirred vigorously at reflux. After boiling had commenced, $HAuCl_4$ was injected. During 10 minutes the colour of the solution changed from yellow to bluish grey and then to soft pink. Sodium citrate reduces $Au^{(III)}$ to $Au^{(0)}$ and cover the seed to prevent the aggregation**.** Immediately, the reaction was cooled until the temperature of 90° C. The decrease of the temperature allows the inhibition of a new nucleation and favouring the consequent overgrown of the pre-synthesized seeds.

The second step is the **growth process** achieved by sequentially addition of sodium citrate and $HAuCl_4$ solution in order to allow an isotropically growth the AuNPs. Size control is achieved by UV-Vis spectroscopical analysis, by withdrawing an aliquot of the reacting solution, and checking the position of the plasmonic band: a size increase corresponds to a red-shift of the peak, according to the table correlation reported in literature.

The third step is the purification of the sample by centrifuge.

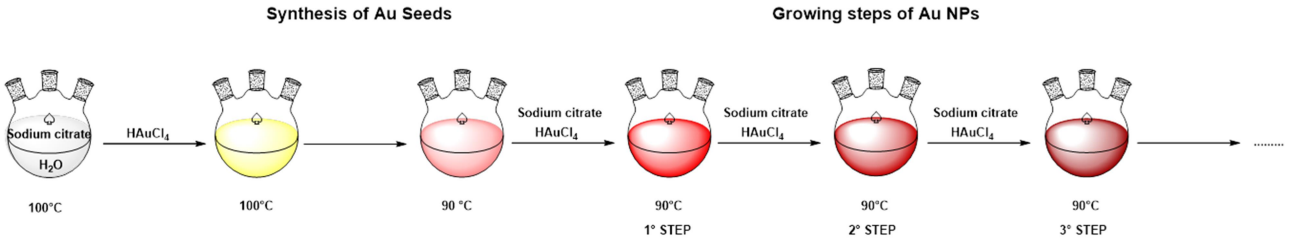

Fig.II.20 Steps of the synthesis: from seed formation to AuNS@SC growth.

Procedure. 1 mL of $HAuCl_4$ 0.025 E-3 M was added to a boiling water solution of sodium citrate (150 mL, 0.22 E-4 M). When the temperature was stabilized at 90° C, 1 mL of sodium citrate (0.06 E-2 M) and 1 mL of a $HAuCl_4$ solution (0.025 E-3 M) were sequentially injected. After 30 min, aliquots of 2 mL were withdrawn for UV-Vis characterization. By repeating this process 3 times, it is possible to reach AuNSs until 30 nm in diameter.

In order to increase quickly the size, the sample was diluted by extracting 55 mL of the sample and adding 53 mL of hot MQ water followed by 2 mL of 0.06 E-3 M sodium citrate. When the temperature is stabilized at 90° C 1 mL of $HAuCl_4$ is added. By repeating the process 4 times

the NSs diameter is around 65 nm. By repeating the additions again, it is possible to increase the diameter of the NSs.

Morphological and optical characterization. Fig. II.21.a reports the extinction spectra of the withdrawn aliquots from the reacting vessel at various growth steps (withdraw every 30 minutes before adding gold salt and citrate): as the size increases (fig. II.21.b), plasmonic band red shifts. Fig. II.21.c shows TEM image of the AuNS@SC at the final size of 67 nm diameter. Furthermore, measurements through dynamic-light scattering apparatus provides a value of 90 nm with a polydispersion index (PdI) of 0.15.

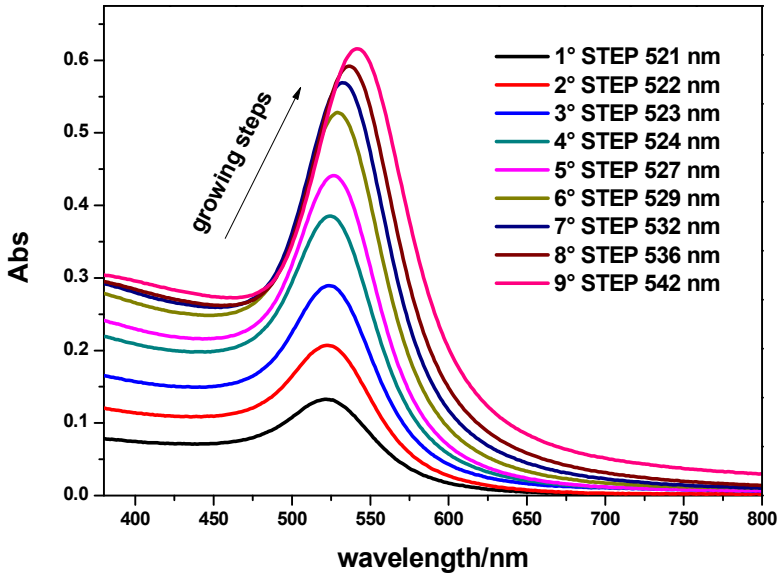

a)

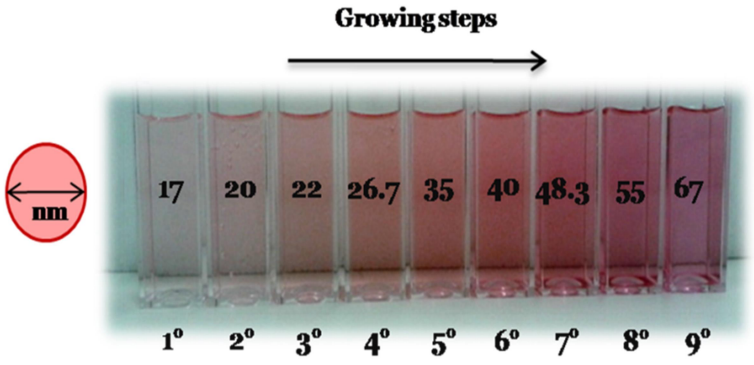

b)

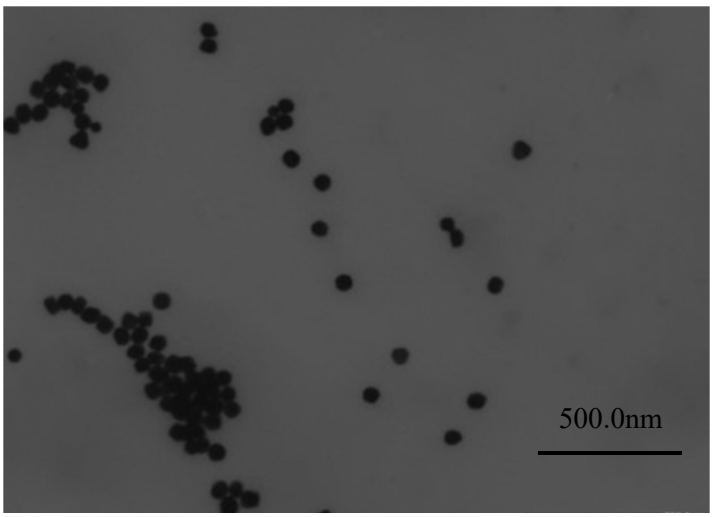

c)

Fig.II.21. Extinction spectra (a) of the withdrawn aliquots from the reacting vessel at various growth steps (b), TEM image of the AuNS@SC at the final size of 67 nm diameter (c)

The disadvantage of this synthetic procedure is that involves a considerable amount of time. In order to reduce the reaction time we used a microwave as the heat source that can produce high quality nanoparticles in a short time period. The time between consecutive additions of gold salt and sodium citrate is reduced to 10 minutes compared to 30 minutes. The parameters (*i.e.* spectral shape and band position, PdI, etc) of the AuNS@SC obtained through the two different heating methods, are identical.

AuNS@SC are well soluble in water; in order to manage AuNPs in organic solvents we changed citrate coating with polymeric one (*e.g.* polyvinylpyrrolidone, PVP). By measure the surface of nanospheres and considering that 60 molecules of PVP occupied 1 nm^2, it's possible know the amount of PVP necessary to cover the surface of nanospheres. [8] The calculated amount of PVP is added to the aqueous solution of AuNS@SC and left overnight under mild stirring. The solubility of the nanoparticles was positively tested in EtOH, confirming the successful change of the covering.

REFERENCE

1. L. Scarabelli, M. Grzelczak, L. M. Liz-Marzán, *Chem. Mater*., **2013** , 25, 4232
2. L. Scarabelli, A. Sánchez-Iglesias, J. Pérez-Juste, L. M. Liz-Marzán, *J. Phys. Chem. Lett*., **2015**, 6, 4270
3. Q. Liu, Y. Yuan, I. I. Smalyukh, *Nano Lett*., **2014**, 14, 4071
4. A. B. Serrano-Montes, D. Jimenez de Aberasturi, J. Langer, J. J. Giner-Casares, L. Scarabelli, A. Herrero, L. M. Liz-Marzán, *Langmuir*, **2015**, 31, 9205
5. S. E. Lohse, N. D. Burrows, L. Scarabelli, L. M. Liz-Marzán, and C. J. Murphy, *Chem. Mater.,**2014**, 26,* 34
6. L. Scarabelli, M. Coronado-Puchau, J. J. Giner-Casares, Ju. Langer, L. M. Liz-Marzán, *ACS Nano*, **2014**,8, 5833
7. N. G. Bastus, J. Comenge, V. Puntes, *Langmuir*, **2011**, 27, 11098
8. A. De Luca, M.Ferrie, S. Ravaine, M. La Deda, M. Infusino, A. R. Rashed, A. Veltri, A. Aradian, N. Scaramuzza, G. Strangi, *J. Mater. Chem.*, **2012**, 22, 8846

III. SILICA SHELL ON GOLD NANORODS

III.1 Synthetic strategy and thickness control

III.2 Obtained results

III.3 Discussion

III.4 Conclusions

III.1 Synthetic strategy and thickness control

Various research groups have focused their attention on the dielectric properties of AuNRs cover shell to tune light scattering properties of gold nanoparticles [1]; in particular, many synthetic protocols have been developed to cover AuNRs with silica shell, because this dielectric material is chemically functionalizable and its thickness can be tuneable.

The silica coating strategy is based on a pH-controlled condensation of tetraethylorthosilicate (TEOS) precursor onto CTAB-capped AuNRs. Hydrolysis and condensation of TEOS require basic conditions, generally reached by adding to the sample ammonia or strong bases such as NaOH. CTAB surfactant deposited onto AuNRs is a structure-directing agent [2] that facilitates the formation of mesostructured silica shell around the NRs. Because CTAB molecules adsorbed on AuNRs act as templates for the growth of the silica shell, it is necessary to maintain this coverage during TEOS condensation; nevertheless, the addition of NaOH can dislodge CTAB molecules from the gold surface (on which they are held by electrostatic interactions) due to the presence of the Na^+ hard ions. To overcome this, methods for coating silica onto CTAB-capped AuNRs suggest the addition of a CTAB solution to the reaction vessel, to restore the CTAB molecules that are gradually detached from the NRs surface.

Hydrolysis and condensation of a silicate precursor

The silica source in the gold nanoparticles coating process is tetraethylorthosilicate (TEOS) (Fig. III.1).

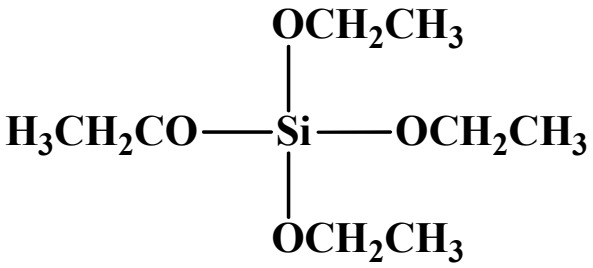

Figure III.1. Structure of TEOS, the metal alkoxides starting material.

The hydrolysis reaction, that produces silanol groups, occurs by nucleophilic attack of water to the silicon atom. The reaction is resumed in Scheme III.1.

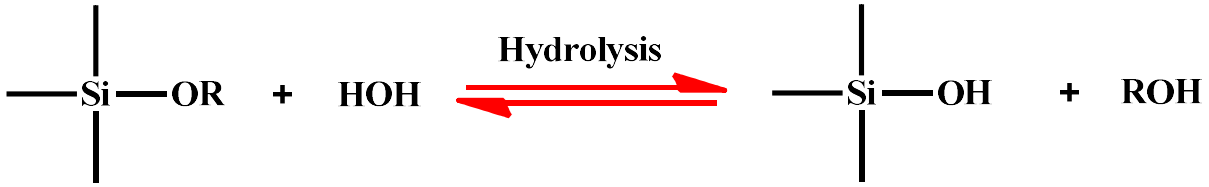

Scheme III.1. The first occurring reaction: a catalysed hydrolysis of TEOS to produce silanol moiety.

Depending on the amount of water and catalyst present (acidic or basic) hydrolysis may proceed to completion, so that all of the OR groups are replaced by OH groups.

Following the hydrolysis reaction, the condensation reaction occurs immediately. The silanol groups reacts with either the hydroxyl group of another hydrolysis intermediate (water condensation) or the ethoxy group of other TEOS (alcohol condensation) to form Si-O-Si bridges (Scheme III.2).

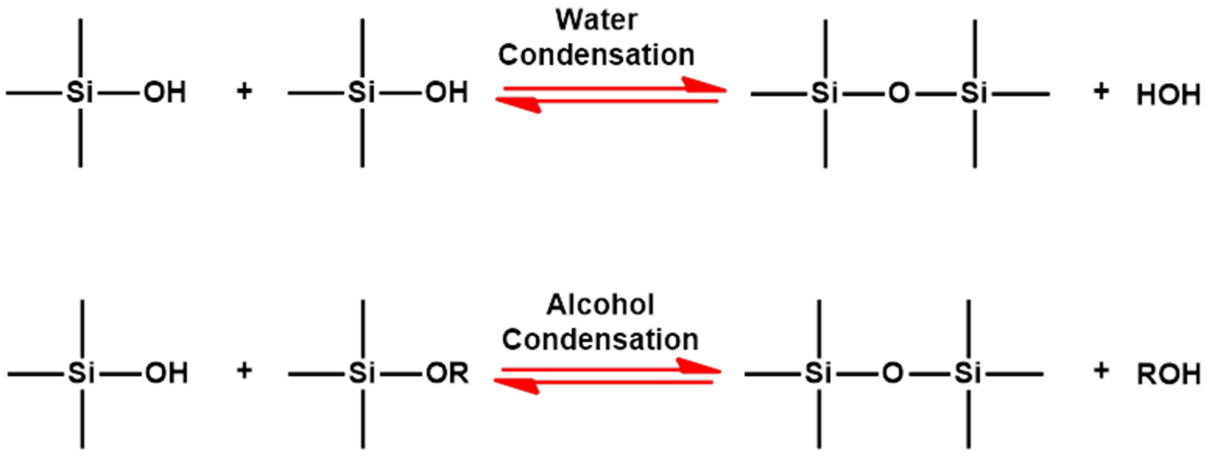

Scheme III.2. The second occurring reaction: silanol condensation to produce organic/inorganic hybrid polymer.

The competition between hydrolysis and condensation conditions gives the growth and coalescence of particles to different final geometries. This competition may be controlled by pH and salinity of solutions, because the speed and the surface charge are modified. In acid medium (pH > 1), the hydrolysis is fast respect to condensation, which determines the rapid formation of smaller monomers and consequently the formation of small particles whose size does not exceed the nanometre. These nanosized particles are incorporated then to form ramified polymeric clusters of weak density. On the contrary, in neutral or moderately basic solution, the condensation of the

silicon species is faster than the hydrolysis and the polymerization is then gradually supported by monomers. This mechanism leads to the formation of dense silica particles. The final size may reach several hundreds of nanometres and the surface is negatively charged. The electrostatic repulsion prevents the aggregation between particles, which remain in suspension within the solvent.

Thickness control of the silica shell

The common strategy to cover nanorods with silica provide to centrifuge an aqueous solution of CTAB-capped AuNRs (AuNR@CTAB) to remove excessive CTAB and other redundant chemicals before the growth of the silica shell. Successively, an amount of CTAB is added to this solution before adding an aqueous NaOH solution, under vigorous stirring. Finally, a TEOS methanol solution is added. The reaction is left under gentle stirring over night. Afterword the mixture is centrifuged and then redispersed in water. Because silica-coated AuNRs (AuNR@SiO_2) are not stable in water for a long time, if necessary, the sample is redispersed in alcoholic solvents.

Silica shell, being a more effective cover of metal surface respect to the CTAB cover, modifies the spectral position of the AuNR longitudinal SPR peak. In fact, after coating with silica, the longitudinal SPR peak of AuNR@SiO_2 solution red-shifts compared to AuNR@CTAB solution because refractive index of the mesoporous silica shell is higher (n_d^{20}=1.45) than refractive index of water embedding CTAB shell (n_d^{20}=1.33) [3]; increasing the silica shell thickness the longitudinal band redshifts consequently [4]. Moreover, silica shell usually embeds molecules like dyes, and its surface is chemically functionalizable [1].

Our goal was to cover AuNR@CTAB with a silica layer perfectly homogeneous and to modulate its thickness. We performed several studies varying some parameters such as TEOS and AuNRs concentration, as well as pH value and CTAB concentration.

III.2 Obtained results

Tracy Protocol (MTP). AuNR@SiO_2 were prepared by using the following modified Tracy protocol [5], hereafter indicated as MTP. The first step is the addition of an aqueous solution of CTAB (10 μL, 0.2 M) to 2 mL of an aqueous dispersion of AuNR@CTAB (0.3 E-3 M). After few seconds 20 μL of a 0.1 M NaOH aqueous solution were added under vigorous stirring, reaching a pH value of 8.5, followed by three additions, each of 12 μL, of TEOS 20% v/v in methanol under gentle stirring, at room temperature. After 14 h, the mixture was centrifuged in MilliQ water twice at 6000 rpm for 10 min and the sample was redispersed in 2 mL of MilliQ water.

The TEM images (Fig. III.2) shows the presence of silica shell around NRs with a thickness 24 nm x 12 nm, long axis x short axis, respectively. Extinction spectra (Fig. III.3) show that the plasmonic longitudinal band of AuNR@SiO_2 (peaked at 834 nm) is redshifted compared to that of AuNR@CTAB (which is peaked at 786 nm).

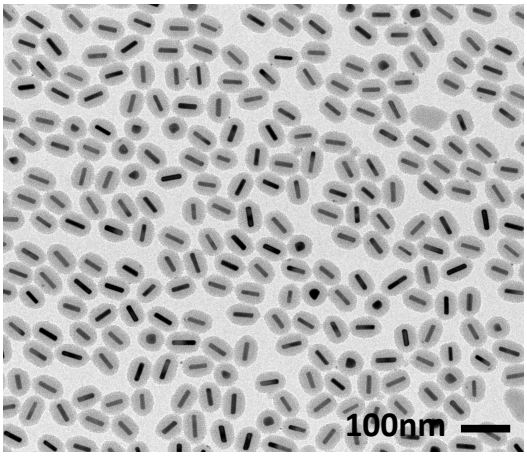

Figure III.2. TEM image of AuNR@SiO_2 prepared according the modified Tracy protocol (see text)

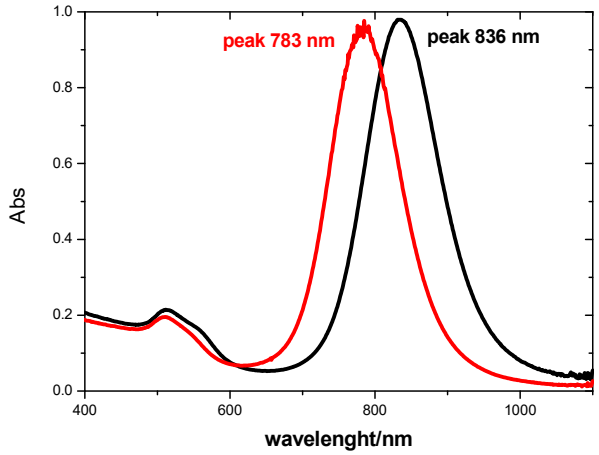

Fig. III.3. Normalized extinction spectra of AuNR@CTAB (red line) and AuNR@SiO_2 (black line) in water solution

Experimental parameters controlled during the silica coverage of AuNRs include pH, amount of the added CTAB solution, TEOS concentration, concentration of the starting AuNR@CTAB solution and the reaction time.

Firstly, we have optimized the pH value and CTAB solution concentration, to obtain a detectable and homogeneous silica shell, and then we have studied the correlation between [TEOS]/[AuNR@SiO_2] ration and the silica coverage.

pH. MTP requests an amount of NaOH corresponding to a pH value of about 8.5. We modified the amount of NaOH up to measure a pH value around 10, leaving unchanged the other parameters; as a result in few seconds AuNRs precipitated on the bottom of the vials.

In another experiment we lowered the NaOH amount down to reach a final pH value of 8; in this case, no precipitation was recorded, the procedure according to MTP was completed and the product analysed by TEM (Fig. III.4). AuNRs image showed the absence of an appreciable silica coating.

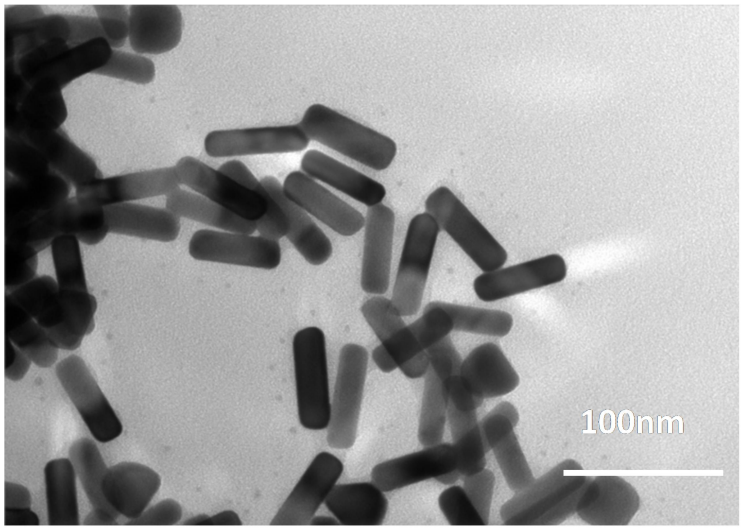

Figure III.4. TEM image of AuNRs prepared according MTP at pH=8

In the first case (pH=10), the alkalinity of the reaction environment causes a rapid TEOS polymerization creating a sort of cloud that incorporates a number of AuNRs, triggering their precipitation. In the second case (pH=8), the alkalinity of the reaction environment is insufficient to prompt a good TEOS polymerization, so the silica coverage of NR is poor. Concluding, pH=8.5 can be considered an optimal value.

CTAB concentration. As previously reported, the first step in MTP is the addition of an aqueous solution of CTAB 0.2 M to an aqueous dispersion of AuNR@CTAB. We lowered the CTAB concentration to 0.1M. The nanoparticles obtained were observed at TEM (Fig. III.5) and compared to the corresponding results obtained by using MTP (Fig. III.2): the silica coverage appears to be unchanged.

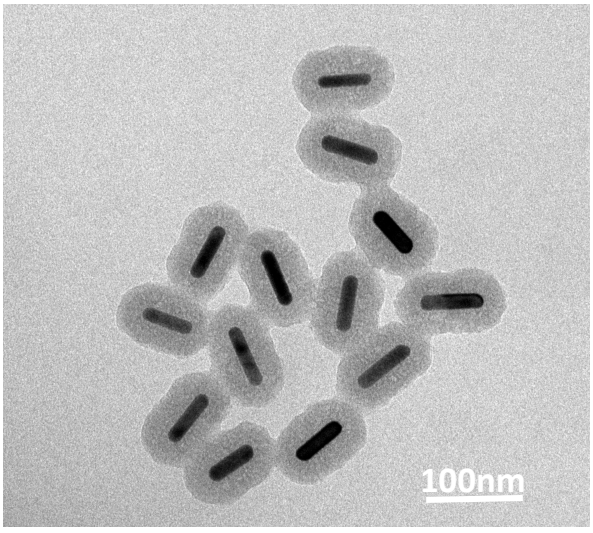

Figure III.5. TEM image of AuNR@SiO_2 prepared according MTP by reducing the CTAB concentration to 0.1 M.

Halving again the CTAB concentration down to 0.05 M, we obtained a disappointing result as shown in the TEM image of Fig. III.6, while reducing again the CTAB concentration down to 0.005 M, after few hours from the last TEOS addition, a burgundy cloud became to appear in the solution that in few seconds precipitated on the bottom of the vials.

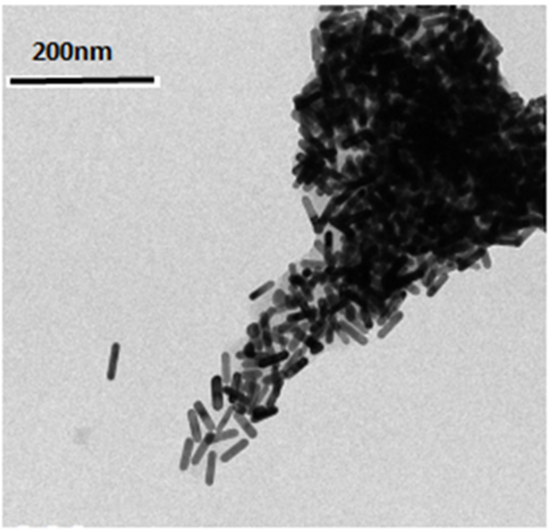

Figure III.6. TEM image of AuNR@SiO_2 prepared according MTP by reducing the CTAB concentration to 0.05 M.

Successively, we try to increase CTAB concentration up to 0.8 M. TEM images (Fig. III.7 a, b) show the expected AuNR@SiO_2 nanoparticles, but the silica coverage is not uniform on the gold surface, and the size of AuNR@SiO_2 appears inhomogeneous. These features can be attributed to the excessive CTAB concentration over the CMC (§ I.2), that hamper the formation of the templating micelles, leading to a disordered silica growth.

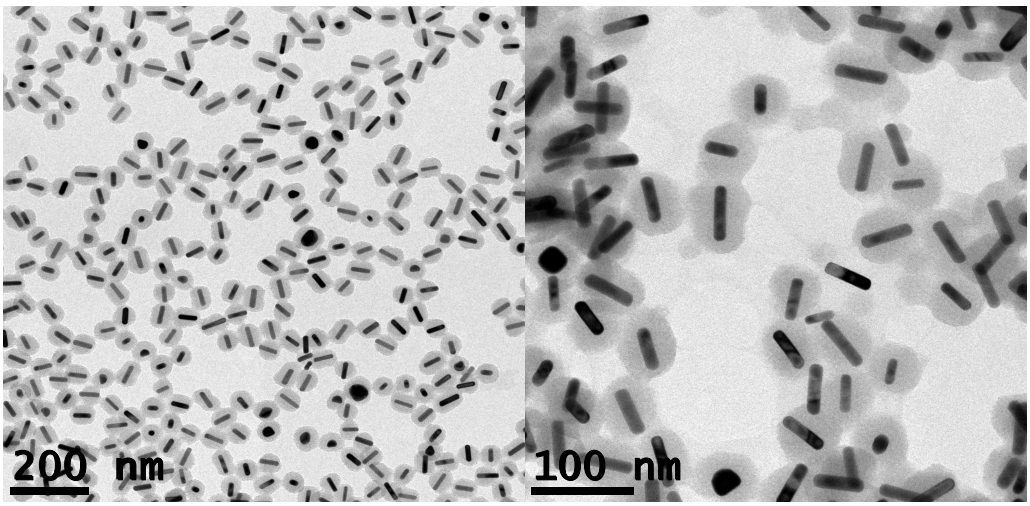

Figure III.7. TEM image of AuNR@SiO_2 prepared according MTP by increasing the CTAB concentration to 0.8 M.

TEOS concentration. According to the literature [1], the thickness of the silica can be modulated by varying the amount of TEOS and the reaction time. On this basis, we conduct different synthesis maintaining constant AuNR@CTAB concentration and the other parameters (as reported in MTP), and varying the amount of TEOS only. As previously reported, MTP provides a total amount of added

TEOS of 0.3 E-4 mol, by addition of 36 μL of a 20% v/v methanol solution.

We tested four protocols with different amount of TEOS, obtaining AuNR@SiO_2 samples with different silica thickness determined by TEM (Table III.1): Fig. III.8-III.11 report TEM image and the extinction spectrum for each sample.

Table III.1

Sample	***Withdrawn volume from TEOS 20% v/v solution…***	***…corresponding to an added TEOS amount of***	***Obtained silica thickness***
1	60 μL	0.5 E-4 mol	24 nm x 12 nm
MTP	*36 μL*	*0.3 E-4 mol*	*24 nm x 12 nm*
2	24 μL	0.2 E-4 mol	22 nm x 12 nm
3	12 μL	0.1 E-4 mol	16 nm x 12 nm
4	4 μL	0.3 E-5 mol	Not detectable

The silica thickness is reduced by reducing the TEOS amount, although a considerable reduction of TEOS does not correspond to a similarly thickness reduction. Extinction spectra show the typical red-shift as a result of the CTAB replacement with silica coverage. Interestingly, the red-shift extend is reduced by decreasing the TEOS amount; this can be attributed to an increased porosity of the shell, which incorporates a bigger water amount.

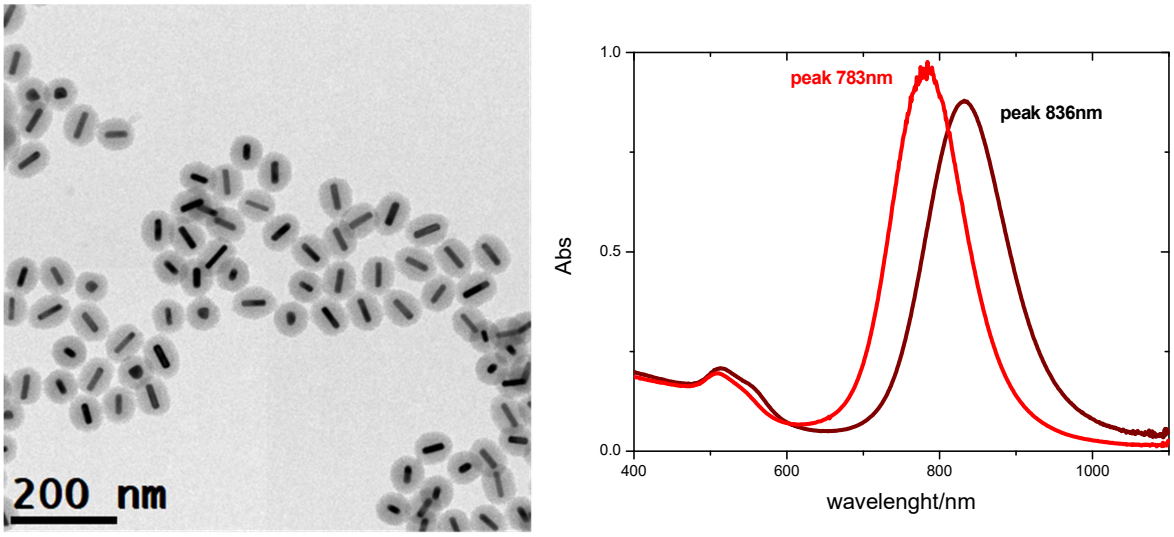

a) b)

Figure III.8. TEM image (a) and extinction spectrum (b) of the AuNR@SiO_2 in water (black line) from sample 1. Normalized extinction spectrum of AuNR@CTAB (red line) is also reported for comparison.

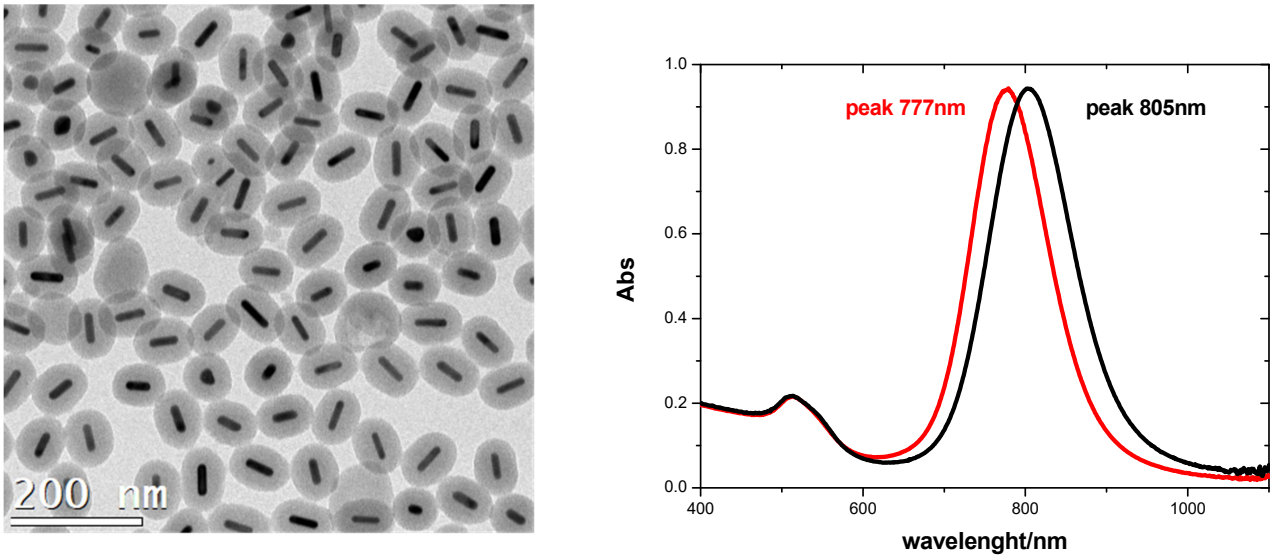

a) b)

Figure III.9. TEM image (a) and extinction spectrum (b) of the AuNR@SiO_2 in water (black line) from sample 2. Normalized extinction spectrum of AuNR@CTAB (red line) is also reported for comparison.

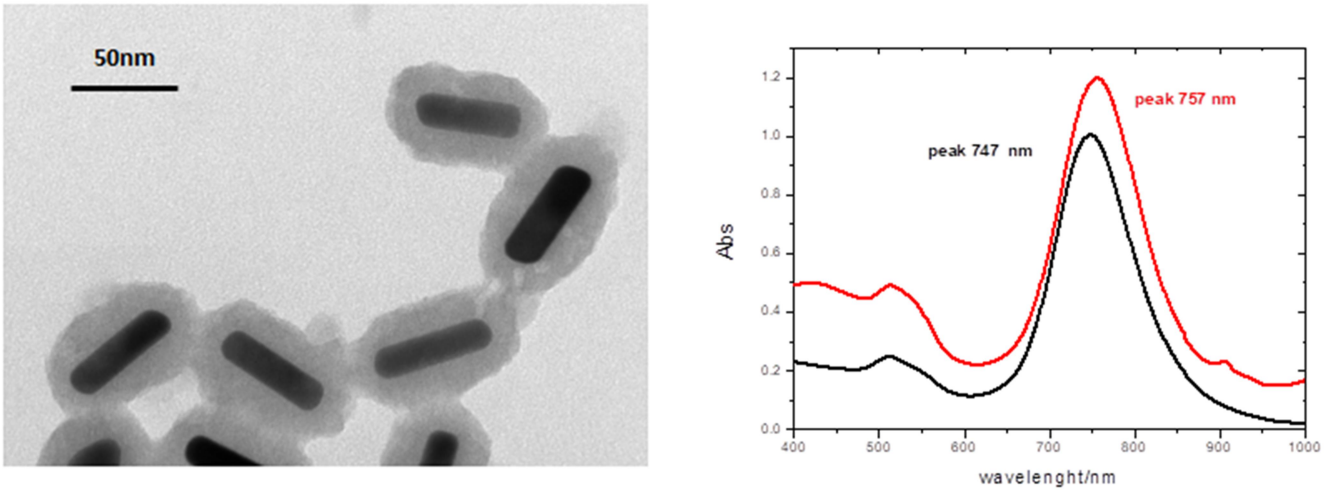

Figure III.10. TEM image (a) and extinction spectrum (b) of the AuNR@SiO_2 in water (black line) from sample 3. Normalized extinction spectrum of AuNR@CTAB (red line) is also reported for comparison.

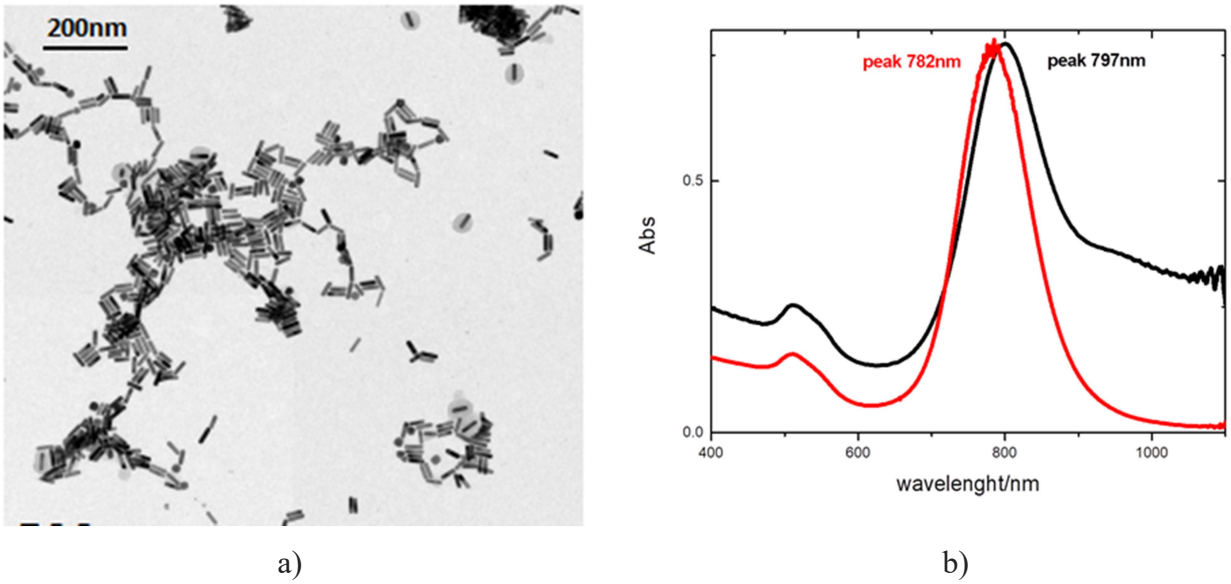

Figure III.11. TEM image (a) and extinction spectrum (b) of the AuNR@SiO_2 in water (black line) from sample 4. Normalized extinction spectrum of AuNR@CTAB (red line) is also reported for comparison.

AuNR@CTAB concentration. According to MTP, the concentration of the starting AuNR@CTAB water solution is 0.3 E-3 M. In order to test the effect of the AuNR@CTAB concentration on the silica thickness, we increased this concentration up to 3.0 E-3 M (sample MTP' in Tab. III.2). As expected, the silica thickness resulted significantly reduced respected to MTP products (12 nm x 7

nm *vs.* 24 nm x 12 nm, respectively), because the TEOS amount available for each AuNR is reduced.

To study the effect of a further increase of the AuNR@CTAB concentration, it is necessary to manage a considerable volume of nanoparticles. Taking into account that TEOS amount used to obtain sample 3 (Tab. III.1) allows to attain the thinner silica thickness, we fixed a TEOS amount of 0.1 E-4 mol (while MTP sets a 0.3 E-4 mol value); in this way, it is possible to use a little volume of AuNR@CTAB solution. Therefore, we prepared two samples, 3' and 3'', with the same TEOS amount but different AuNR@CTAB concentration (Table III.2), observing a different silica thickness: figures III.12-III.14 report TEM images and extinction spectra of the samples. In particular, spectra show the usual red-shift of the longitudinal NR band substituting CTB coverage with silica one, which is reduced according to the thinning of silica thickness.

Tab. III.2

Sample	**[AuNR@CTAB]/M**	**Silica Thickness**
MTP'	3.0 E-3	12 nm x 7 nm
3'	3.0 E-3	10 nm x 8 nm
3''	4.5 E-3	5 nm x 3.5 nm

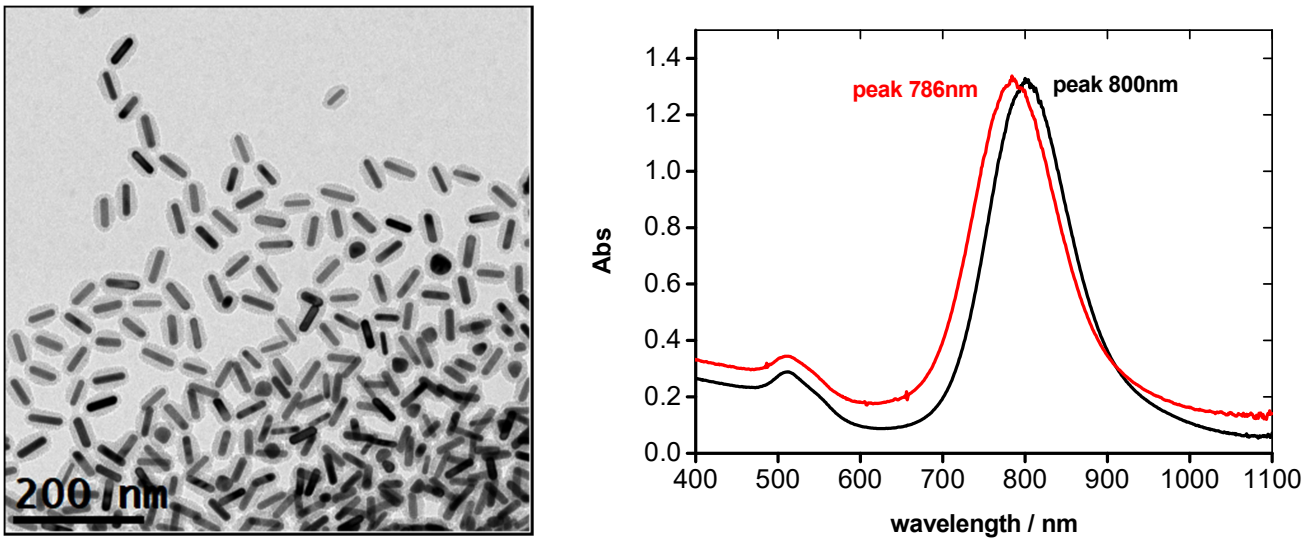

a) b)

Figure III.12. TEM image (a) and extinction spectrum (b) of the AuNR@SiO_2 in water (black line) from MTP' sample. Normalized extinction spectrum of AuNR@CTAB (red line) is also reported for comparison.

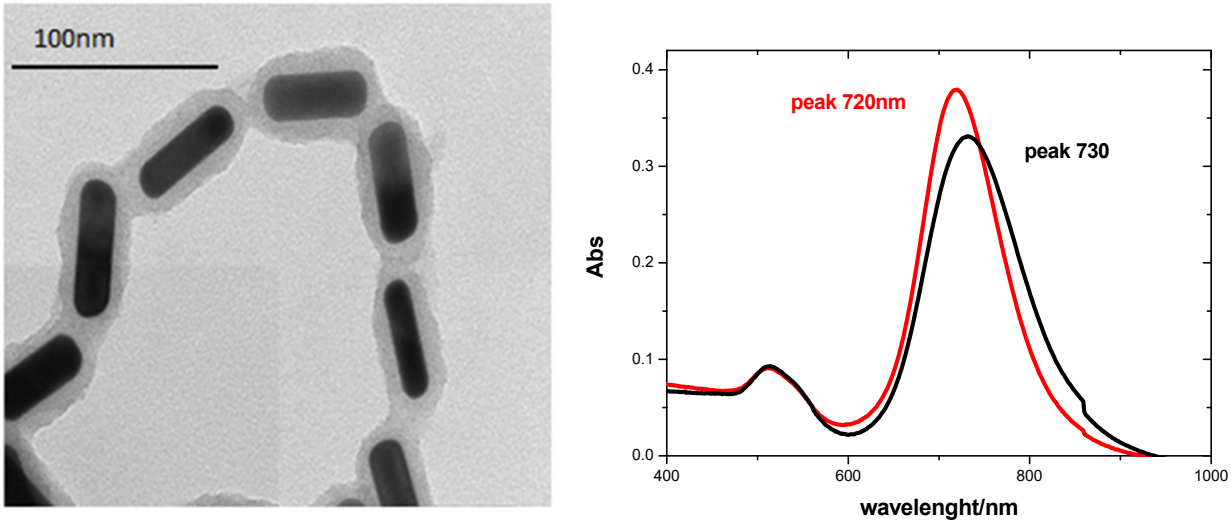

a) b)

Figure III.13. TEM image (a) and extinction spectrum (b) of the AuNR@SiO_2 in water (black line) from sample 3'. Normalized extinction spectrum of AuNR@CTAB (red line) is also reported for comparison.

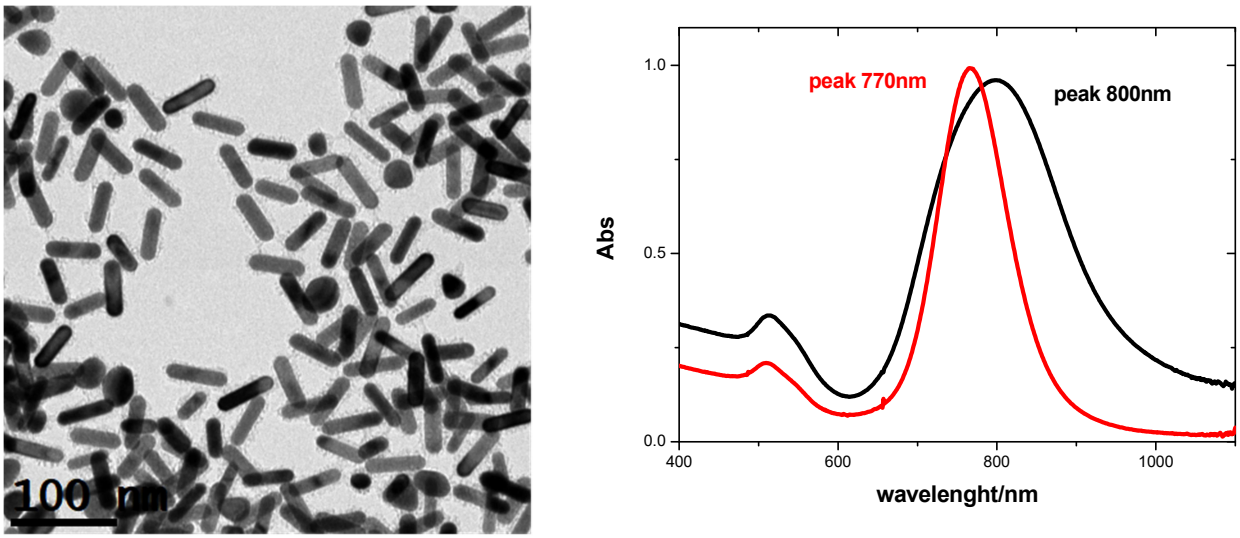

a) b)

Figure III.14. TEM image (a) and extinction spectrum (b) of the AuNR@SiO_2 in water (black line) from sample 3''. Normalized extinction spectrum of AuNR@CTAB (red line) is also reported for comparison.

Reaction time. Literature [5] reports that silica shell growth is rapid over the first hour but slows significantly during the second hour of reaction. According to MTP, the reaction time, *i.e.* the time range between the last TEOS addition and the purification step, is fixed at 14 h. To study the effect of the reaction time variation on the silica thickness, we synthesized AuNR@SiO_2 samples starting from three already illustrated recipes (MTP, 3 and 3'), and reducing the reaction time to 1h.
The obtained results are reported in Tab. III.3 and TEM images in Figures X15-17.

Tab. III.3

Used recipe	Silica thickness after 14 h reaction time	Silica thickness after 1 h reaction time
MTP	24 nm x 12 nm	15 nm x 13 nm
3	16 nm x 12 nm	13 nm x 12 nm
3'	10 nm x 8 nm	10 nm x 6 nm

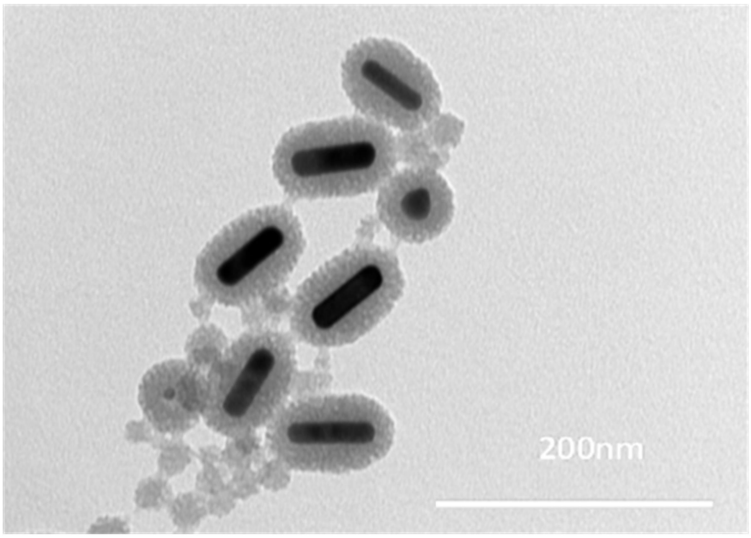

Figure III.15. TEM image of AuNR@SiO_2 prepared according MTP by reducing the reaction time**. It is visible unreacted silica presents also after centrifugation.**

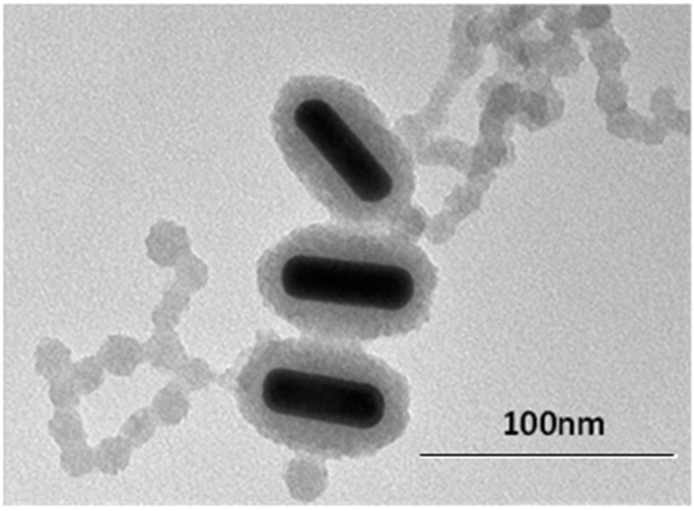

Figure III.16. TEM image of AuNR@SiO_2 prepared according the recipe used to prepare sample 3.

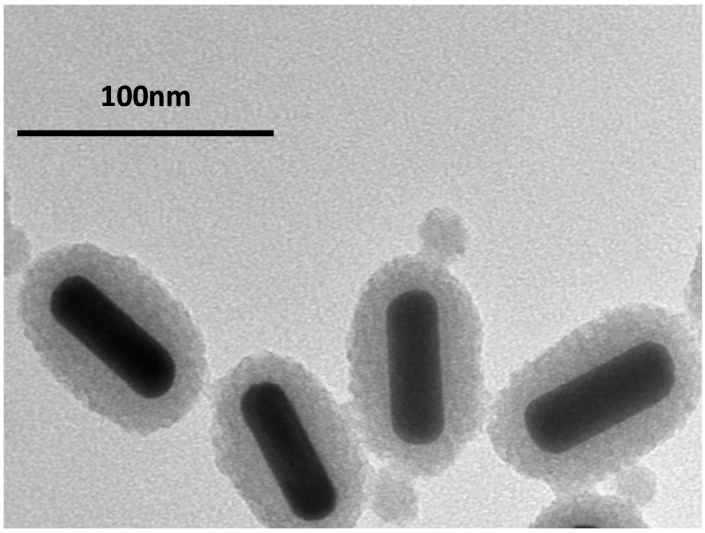

Figure III.17. TEM image of AuNR@SiO_2 prepared according the recipe used to prepare sample 3'.

III.3 Discussion

Various parameters control the thickness of silica shell around gold nanorods, but the obtained results show that the impact of the parameters is different, and small variations of someone can produce very important effects. For example, pH and CTAB concentration are hardly tunable, while TEOS concentration is little sensitive, because, as reported in Table III.1, important variations of this parameter do not cause relevant thickness variations; conversely, AuNR@CTAB amount appears to be more decisive to determine silica thickness (Table III.2).

In fact, what seems to be decisive in controlling the silica thickness is [TEOS]/[AuNR@CTAB] ratio, while to monitor the effective silica growth onto AuNRs, the most suitable observable is the silica shell volume.

In Table III.4, we reported the [TEOS]/[AuNR@CTAB] ratio actually used in 1, 2, 3, MTP, 3' and 3''samples, and the silica shell volume of the obtained nanorods, calculated from TEM images assuming the nanorods shape as a cylinder with two hemispheres.

Table III.4

samples	[TEOS]/[AuNR@CTAB]	volume/nm^3
1	83	102.800
2	33	70.000
3	17	54.200
MTP'	5	35.200
3'	2	20.000
3"	1	12.700

Figure III.18 reports the plotted data, and interestingly, indicates a linear correlation between the silica volume with [TEOS]/[AuNR@CTAB] ratio. In particular, it is possible to recognize two linear trend, with different slope; the steepest slope corresponds to the three samples in which the amount of NaOH is twice the amount used in the other three samples whose points correlate with a lower-slope straight line.

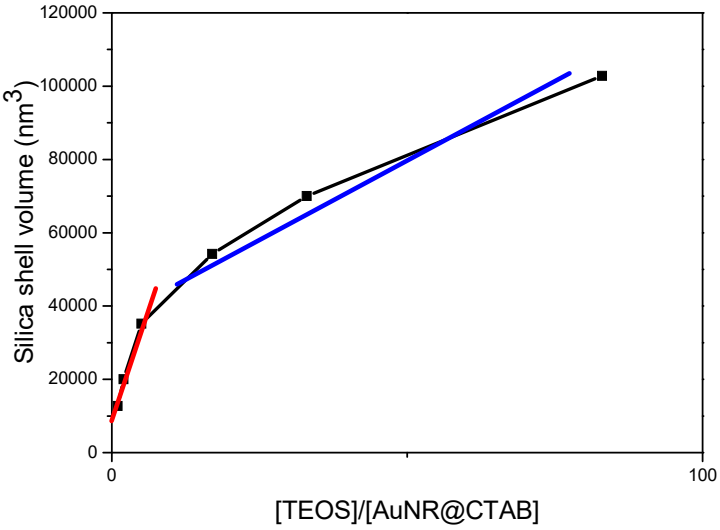

Figure III.18. Correlation between the silica shell volume of AuNR@SiO_2 with [TEOS]/[AuNR@CTAB] ratio

III.4. Conclusions

The silica growth over gold nanorods has been obtained in aqueous solution by using TEOS as silica source, by hydrolysis and condensation in basic environment. To address preferentially TEOS polymerization over NRs surface, rather than in water suspension, the used AuNRs are coated with CTAB that forms templating micelles, inside which silica polymerizes. Nevertheless, a considerable amount of TEOS forms silica spheres in aqueous solution, which are subsequently separated from the AuNR@SiO_2 by centrifuges.

As observed, an excessive pH causes a rapid TEOS polymerization in water suspension, while a low alkaline pH is insufficient to prompt TEOS activation. Because pH is controlled by NaOH addition, Na^+ ion can dislodge CTAB molecules from the gold surface (on which they are held by electrostatic interactions); to counteract this, a CTAB solution is added to the reaction vessel, to restore the CTAB molecules that are gradually detached from the NRs surface. However, CTAB concentration over the CMC hampers the formation of the templating micelles, leading to a disordered silica growth.

While pH and CTAB concentration are hardly tuneable to control silica thickness, [TEOS]/[AuNR@CTAB] ratio is a good parameter for this purpose; in particular, it has been envisaged a linear correlation between this parameter and the silica shell volume, which efficacy seems to be pH-dependent in an extremely high sensitivity.

Because the silica grows on the CTAB micelles formed on the gold surface, its structure is mesoporous, and solvent molecules are embedded into. Consequently, the dielectric constant of the AuNR@SiO_2 shell in water solution depends on the water-embedded molecules, which in turn depends on the silica porosity. In the case of CTAB coverage of the AuNRs, the dielectric constant practically coincides with that of water.

The position of the longitudinal band of AuNR depends on the dielectric constant value of the medium around gold surface; by comparing the band position of AuNR@CTAB with that of AuNR@SiO_2, it is possible to observe a red-shift that varies with the silica thickness. Probably, this trend reflects also the porosity degree of the shell, but to clarify this point, further studies are necessary.

REFERENCES

1. H. Chen, L. Shao, Q. Lia, J. Wang, *Chem. Soc. Rev*., **2013**, 42, 2679
2. T. Ming, L. Zhao, Z. Yang, H. Chen, L. Sun, J. Wang, C. Yan, *Nano Lett*.,**2009**, 9, 3896
3. L. Jiang, H. Mundoor, Q. Liu, I. I. Smalyukh, *ACS Nano*, **2016**, 10, 7064
4. J. Perez-Juste, I. Pastoriza-Santos, L. M. Liz-Marzán, P. Mulvaney, *Coord. Chem. Rev.*, **2005**, 249, 1870
5. W. Wu and J. B. Tracy, *Chem. Mater*.,**2015**, 27, 2888

IV. FUNCTIONALIZATION OF THE SILICA SHELL

IV.1 Silica-shell gold nanorods embedding a metal complex

IV.2. Results and discussion

IV.3 Conclusions

IV.1 Silica-shell gold nanorods embedding a metal complex

Mesoporous silica is an excellent host material, and gold nanoparticles coated with it can be functionalized embedding various compounds into the silica shell [1]. In particular, encapsulating photophysically-active molecules in the shell of AuNR@SiO_2 provides the opportunity to study the interactions between their excited electronic states and the plasmonic modes of gold nanoparticles.

To study the "talking" between luminescent compounds and the gold plasmon, we selected a highly-emissive Ir(III) complex (**Ir_1** in Fig. IV.1) and prepared embedding **Ir_1** silica-coated AuNRs nanorods (AuNR@(**Ir_1**)SiO_2) to investigate the properties of two water samples: the first, called ***functionalised system***, containing AuNR@(**Ir_1**)SiO_2, and the second, called ***assisted system***, containing AuNR@SiO_2 and **Ir_1**, both dissolved in solution (Fig. IV.2). Because the experiments were been conducted in aqueous environment, silica-coated AuNRs were overcoated by 3-(triethoxysilyl)propylsuccinic anhydride (TPSA), which makes nanoparticles very stable in water. We will call these samples as AuNR@(**Ir_1**)SiO_2@TPSA and AuNR@SiO_2@TPSA.

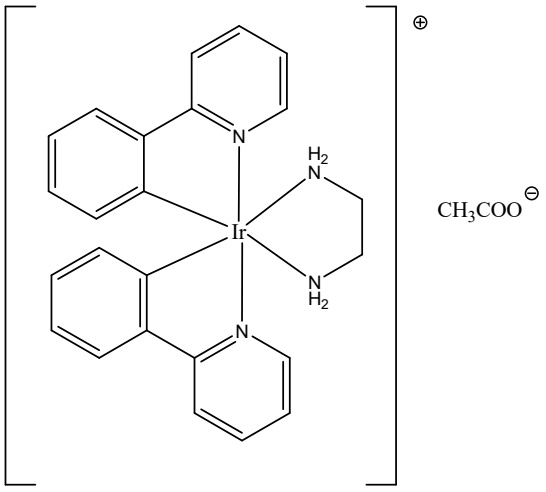

Fig. IV.1. Formula structure of **Ir_1**

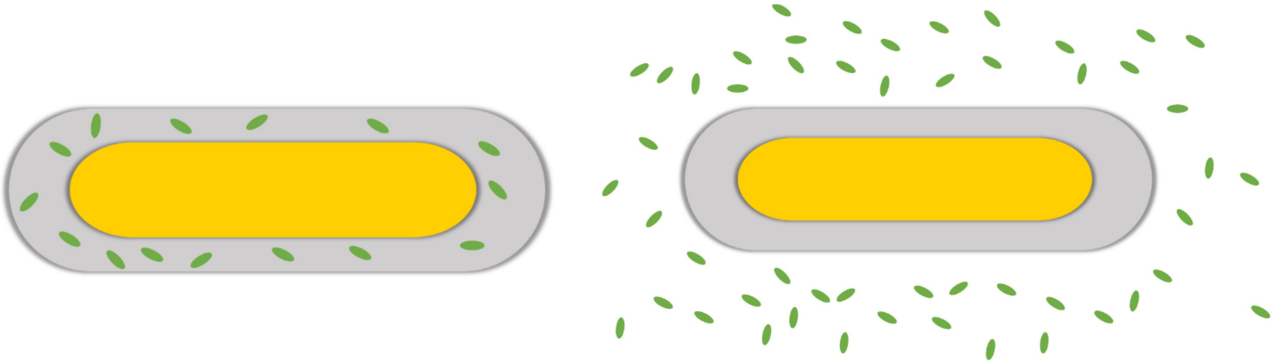

AuNR@(**Ir$_1$**)SiO$_2$@TPSA AuNR@SiO$_2$@TPSA + **Ir$_1$**

Fig. IV.2. Sketch of the *functionalised system* (on the left) and the *assisted system* (on the right). The green ellipse represents **Ir$_1$**.

Photophysical properties of Ir$_1$. The photophysical characterization of **Ir$_1$** was already published in various papers [2] [3] [4]. Here we resume the principal features. The absorption spectrum of **Ir$_1$** (Figure IV.3) is dominated by the intense spin-allowed $^1\pi$-π^* ^{1}LC transitions of aromatic ligands. At higher wavelength (350 – 450 nm), less-intense ^{1}MLCT bands are present. Additionally, the weak tails observed above 450 nm are due to the direct spin-forbidden population of the triplet excited states (^{3}MLCT and ^{3}LC transitions). Indeed, the high spin-orbit coupling of the Iridium metal core allows the mixing of triplet states with the higher-lying ^{1}MLCT levels.

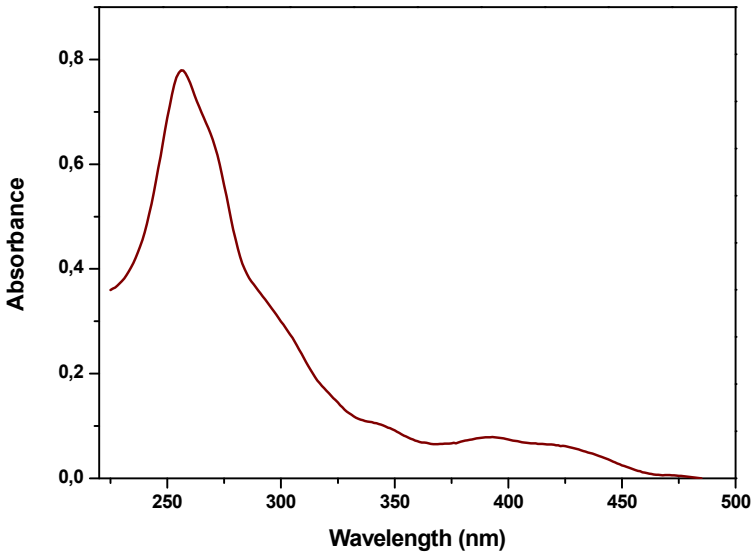

Fig. IV.3. Absorption spectrum of **Ir$_1$** in water at room temperature (3.20 E-5 mol/L).

The presence of a high spin-orbit coupling increases the intersystem crossing efficiency from the singlet to the triplet excited states, with a final high-efficient spin-forbidden phosphorescence emissions. **Ir_1** in water solution (Figure IV.4) give an intense luminescence band centred at 515 nm, due to the ^{3}MLCT deactivation. As expected, the emission intensity is highly sensitive to the amount of oxygen.

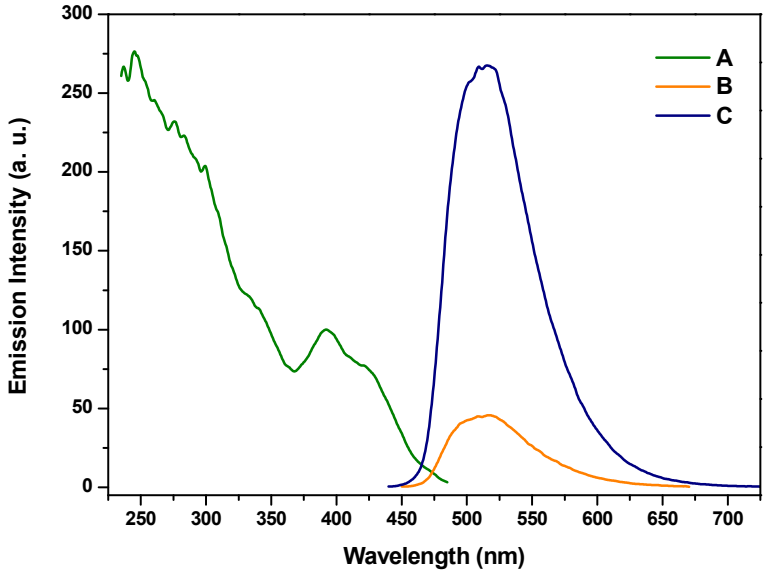

Figure IV.4. Excitation spectrum (**A**) in degassed water (λ_{em}= 515 nm) and emission spectra of **Ir_1** at room temperature in air-saturated (**B**) or in degassed (**C**) water (λ_{ex}= 260 nm).

Time-dependent emission intensity of **Ir_1** (Figure IV.5) has been fitted by a mono-exponential decay function.

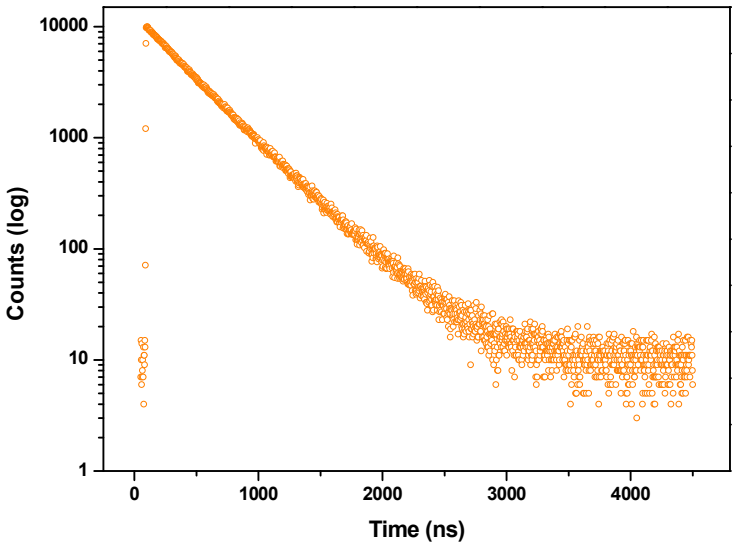

Fig.IV.5 Time-resolved emission decay of **Ir_1** in water (λ_{ex}= 379 nm, $\lambda_{monitored}$= λ_{em}= 510 nm).

In Ar-equilibrated solutions, the complex shows lifetime values of 2.182 μs that is reduced to 0.395 μs in presence of oxygen. As expected, the emission quantum yield decreases from the values of 0.96 in absence of oxygen to 0.10 in air-equilibrated solution.

IV.2. Results and discussion

Synthesis of AuNR@SiO_2@TPSA. 10 µL of 0.2 M CTAB were added to 2 mL of an aqueous dispersion of AuNR@CTAB (2.5E-4 M). After few seconds 20 µL of a 0.1 M NaOH aqueous solution were added under vigorous stirring, followed by three additions, each of 12 µL, of TEOS 20% v/v in methanol under gentle stirring, at room temperature. After 14 h, the mixture was centrifuged in EtOH twice at 6000 rpm for 10 min. Successively, a solution of 2 mL of EtOH containing 5 µL of TPSA was added, and gently stirred overnight. Finally, the mixture was centrifuge and redispersed in water.

*Synthesis of AuNR@(**Ir_1**)SiO_2@TPSA.* 6 mg of **Ir_1** complex were dissolved in 2 mL of an aqueous dispersion of AuNR@CTAB (2.5E-4 M). Henceforth the synthesis proceeds as in the previous case. After three purification steps, the washing waters, tested by spectroscopy, are free from Iridium (III) complex.

TEM Image. Both samples were observed under TEM (Fig. IV.6). Although the followed synthetic procedures are identical, the coating thickness is different; in particular, the thickness of AuNR@(**Ir_1**)SiO_2@TPSA is greater than that of AuNR@SiO_2@TPSA, 22x18 nm *vs.* 18x15 nm, respectively.

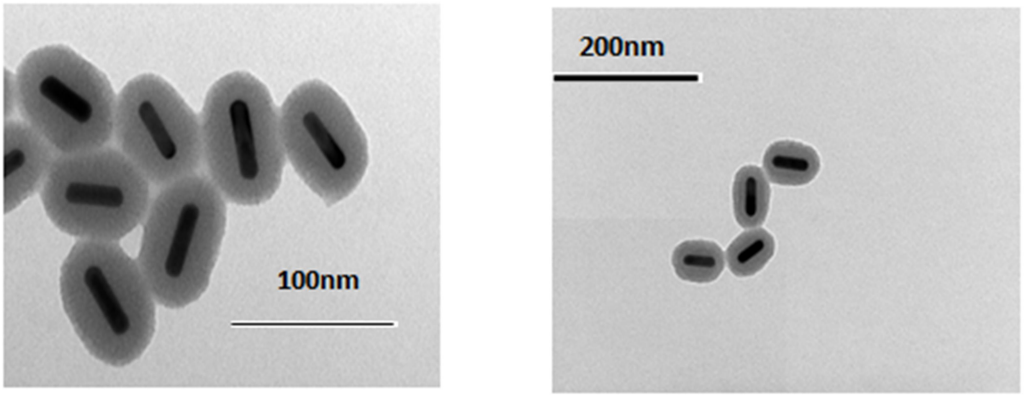

(a) (b)

Fig. IV.6. TEM images of AuNR@(**Ir_1**)SiO_2@TPSA (a), and of AuNR@SiO_2@TPSA (b)

Spectroscopical characterization. Figure IV.7 reports the extinction spectra of AuNR@(**Ir_1**)SiO_2@TPSA and of AuNR@SiO_2@TPSA water solution. While plasmonic transversal band is practically unvaried, longitudinal one appears red-shifted in the NRs embedding **Ir_1** respect

to those without. Moreover, in the spectrum of AuNR@(**Ir$_1$**)SiO_2@TPSA is visible at 420 nm an absorption band of the complex (see Fig. IV.3).

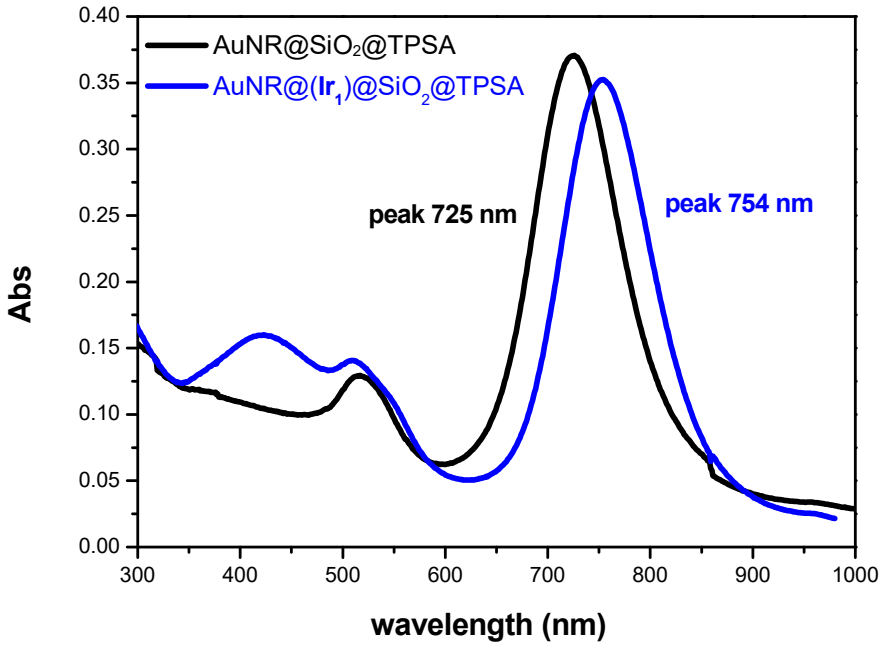

Fig. IV.7. Extinction spectra of AuNR@(**Ir$_1$**)SiO_2@TPSA and of AuNR@SiO_2@TPSA.

Since the sensitivity of the longitudinal band to the refractive index is known, the AuNR@(**Ir$_1$**)SiO_2@TPSA red-shift should be due to a change of the refractive index of the medium around gold surface. Because both samples are identically coated, the difference can be ascribed to a variation of the CTAB layer over which silica growths. In fact, the **Ir$_1$** is an ionic compound (Fig. IV.1), and the positively charged ion can partially dislodge CTAB molecules from the gold surface (on which they are held by electrostatic interactions), changing the layer directly in contact with the metal. Moreover, assuming this hypothesis, the CTAB micelles on the gold surface (that favour the ordered silica growth), are somewhat disrupted, and the silica, no longer confined within the micelles, can grow in a more disordered way but gives rise to greater shell thicknesses, as it is evident for the AuNR@(**Ir$_1$**)SiO_2@TPSA sample.

To support the hypothesis that **Ir$_1$** can dislodge CTAB layer causing a longitudinal band red-shift, growing amounts of this complex were added to a water solution of AuNR@CTAB. The results, reported in Fig. IV.8, show an increasing red-shift, confirming the hypothesis.

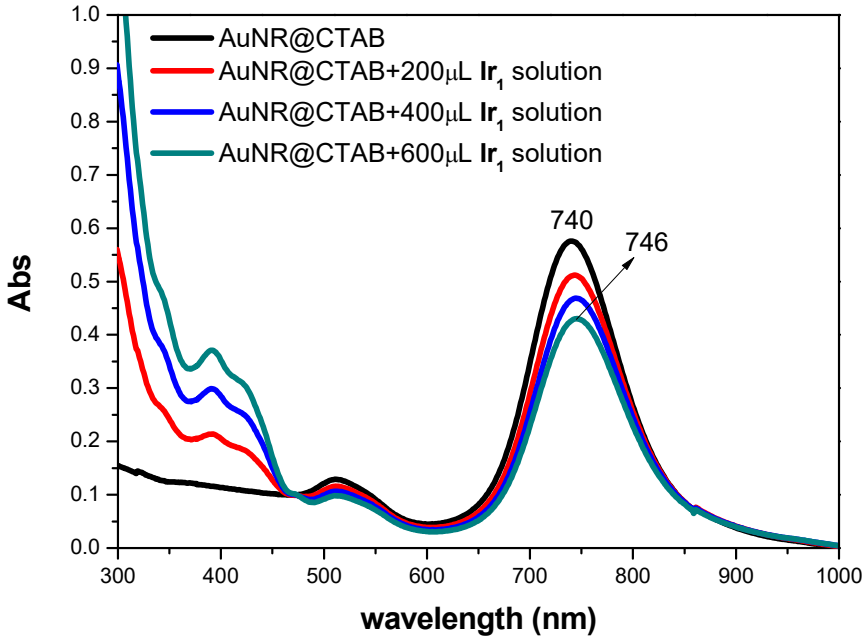

Fig. IV.8. Extinction spectra of AuNR@CTAB solutions added with increasing amount of $\mathbf{Ir_1}$ solution.

$\mathbf{Ir_1}$ can replace CTAB layer because CTAB molecules are held onto metal surface by electrostatic interactions. If the AuNR coating was made by PEG-SH (which adheres to gold by a strong S-Au bond), $\mathbf{Ir_1}$ could not replace it, and consequently no red-shift should be observed. To better confirm our hypothesis, a good amounts of $\mathbf{Ir_1}$ were added to an alcoholic solution of AuNR@PEG-SH (see § II.2 for the synthesis), and the solution extinction spectra are reported in Fig. IV.9. No red-shift is observed.

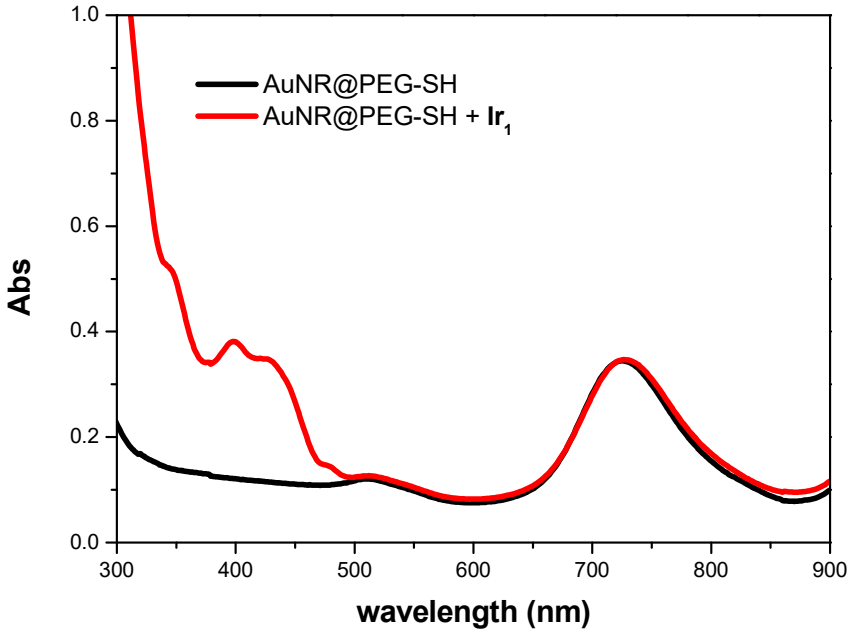

Fig. IV.9. Extinction spectra of AuNR@PEG-SH solutions with and without adding $\mathbf{Ir_1}$ solution.

Figure IV.10 reports the water solution extinction spectra of the ***functionalised system*** (AuNR@(**Ir$_1$**)SiO$_2$@TPSA) and of the ***assisted system*** (AuNR@SiO$_2$@TPSA + **Ir$_1$**).

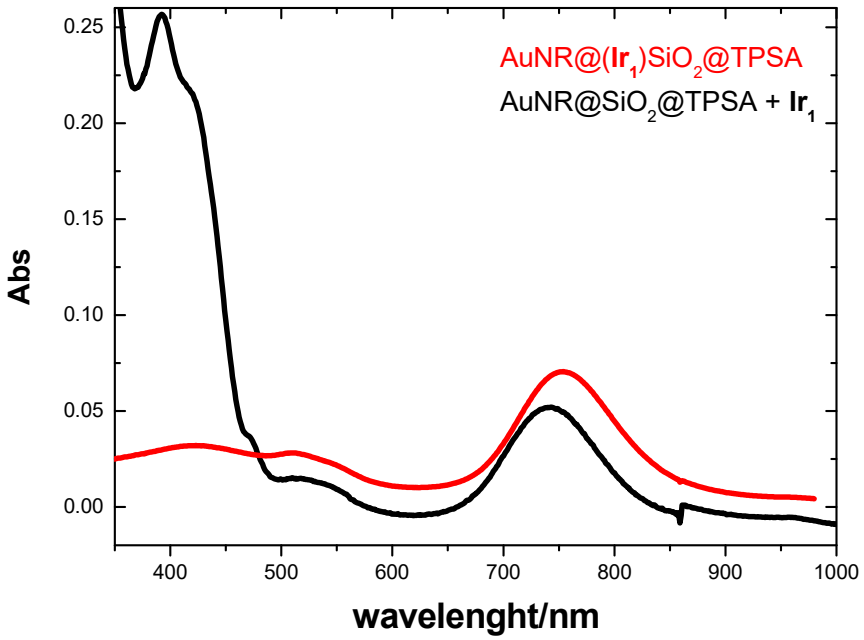

Fig. IV.10. Water solution extinction spectra of the ***functionalised system*** (AuNR@(**Ir$_1$**)SiO$_2$@TPSA) and of the ***assisted system*** (AuNR@SiO$_2$@TPSA + **Ir$_1$**).

Very interesting is to explore the differences between the two systems by exciting the Ir(III) complex, and comparing the results with an analogous functionalised system in which gold nanorods are replaced by gold nanospheres [2], AuNS@(**Ir$_1$**)SiO$_2$@TPSA.

Emission spectra series of correlated water samples, all containing **Ir$_1$**, are reported in Fig. IV.11. AuNR@(**Ir$_1$**)SiO$_2$@TPSA and AuNS@(**Ir$_1$**)SiO$_2$@TPSA are identical except the form, rod and sphere, respectively; (**Ir$_1$**)SiO$_2$@TPSA is made of TPSA-coated **Ir$_1$**-embedding silica nanoparticles. These samples are compared with the assisted system AuNR@SiO$_2$@TPSA + **Ir$_1$** and with a sample containing **Ir$_1$** dissolved in water. By comparing the emission spectra of these five samples, obtained exciting at 390 nm, *i.e.* on the electronic levels of the Ir(III) complex, we note that, while four samples show an identical emission spectrum, the functionalised system AuNR@(**Ir$_1$**)SiO$_2$@TPSA is quite different. In particular, four samples (detailed in Fig. IV.11) show a single band peaked at 515 nm corresponding to the emission of **Ir$_1$** in water solution (Fig. IV.4), AuNR@(**Ir$_1$**)SiO$_2$@TPSA water solution shows a well-defined vibronically structured band at 465 nm, a less intense similar band centred at 542 nm, and a low-defined band at exactly 515 nm.

Lifetime measurements are reported in Tab. IV.1

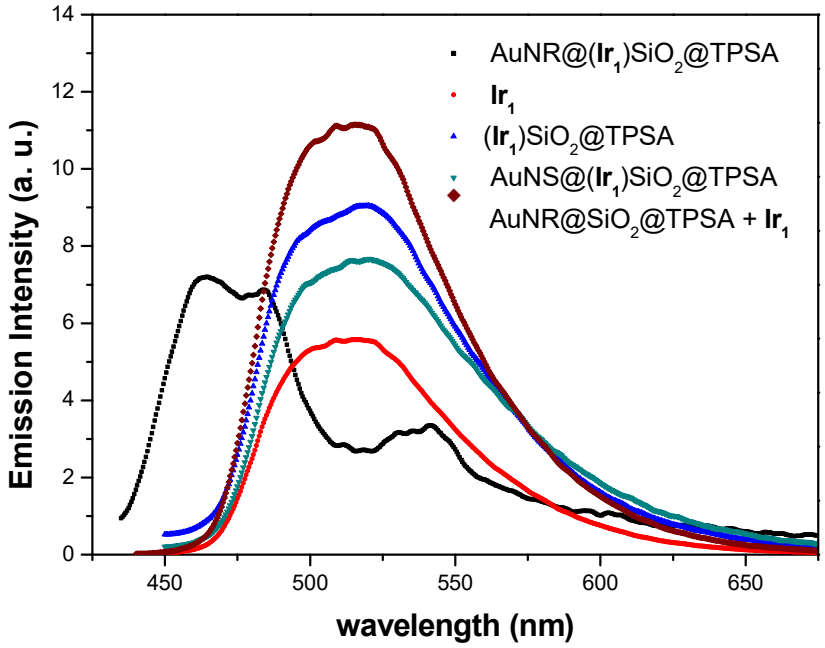

Fig. IV.11. Emission spectra of a series of systems obtained by exciting the Ir(III) complex at 390 nm. All samples are water solutions.

Table IV.1. Lifetimes measured in air-equilibrated water samples

Sample	Emission, λ_{max}/nm	Lifetime, τ/ns (α/%)
Ir_1	515 nm	395 ns
(**Ir_1**)SiO_2@TPSA	515 mn	415 ns (56.4%); 2372 ns (43.6%)
AuNS@(**Ir_1**)SiO_2@TPSA	515 nm	408 ns (31.9%); 1210 ns (68.1%)
AuNR@(**Ir_1**)SiO_2@TPSA	465 nm	7 ns (15.4%); 83 ns (11.0%); 869 ns (63.6%)
	515 nm	8 ns (11.8%); 204 ns (19.6%); 964 ns (68.6%)
	542 nm	18 ns (2.7 %); 279 ns (30.0 %); 1060 ns (67.3%)
AuNR@SiO_2@TPSA + **Ir_1**	515 nm	392 ns

By considering the emission intensity decay of **Ir_1** encapsulated into TPSA-coated silica spheres (*i.e* (**Ir_1**)SiO_2@TPSA sample), we note that compared to **Ir_1** in water solution, a longer lifetime appears, while the short lifetime value remains almost identical. The last lifetime (415 ns) can be attributed to the **Ir_1** fixed on the nanoparticle surface (in contact with the solvent, and therefore in a situation similar to **Ir_1** free in solution), while the former (2372 ns) is attributed to the

decay of the Ir(III) complex entrapped into the rigid silica shell. This is confirmed by the data obtained from AuNS@(**Ir$_1$**)SiO_2@TPSA sample, which differs from (**Ir$_1$**)SiO_2@TPSA by the presence of a spherical gold core; in this case, we measure a short lifetime of 408 ns (attributable, as usually, to the **Ir$_1$** on the nanoparticle surface), and a long lifetime of 1210 ns, attributed to the **Ir$_1$** entrapped into silica matrix, but reduced by an energy transfer process towards gold plasmon, peaked almost exactly at 515 nm.

More difficult is to rationalize the behaviour of AuNR@(**Ir$_1$**)SiO_2@TPSA, which differs from the previous sample for the shape of gold core. We have also considered the synthetic procedure followed for the two sample; in fact, in the case of gold nanospheres, microemulsion method was employed [2], which uses gold nanospheres coated with sodium 2-mercaptoethanesulfonate (MES) over which TEOS polymerizes. In the case of gold nanorods, TEOS polymerizes over a CTAB-coated rods.

We propose that high-energy and relatively high-intensity emission bands at 465 nm of AuNR@(**Ir$_1$**)SiO_2@TPSA are ascribable to the **Ir$_1$** directly in contact with the metal. The possibility of a direct contact of the fluorophore with the metal surface is due to the fact that the ionic nature of the Ir(III) complex allows a partial substitution of the CTAB molecules on the gold surface (on which they are held by electrostatic interactions), while this process is prevented in the analogous AuNS@(**Ir$_1$**)SiO_2@TPSA by the high bond interaction between MES and gold.

From a photophysical point of view, the interactions of fluorophores with metallic surfaces can have a number of useful effects, including increased quantum yields, increased photostability, increased distances for resonance energy transfer, and decreased lifetimes. These effects are called metal-enhanced fluorescence (MEF) [5].

A fluorophore in the excited state has the properties of an oscillating dipole. The excited fluorophore can induce oscillations of the electrons in the metal. The electric field created by the metal can interact with the excited fluorophore and alter its emission. As expected, we observe an increased intensity emission of the MEF bands, respected to the others. Moreover, a very short lifetime of 7 ns appears.

Really, at 465 nm a three-exponential function is necessary to fit decay profile. This is due to the strictly overlapping bands, each of which is characterized by a proper lifetime, and refers to different conditions of the fluorophore, as illustrated in fig. IV.12. In the appendix we reported the time-resolved emission decays.

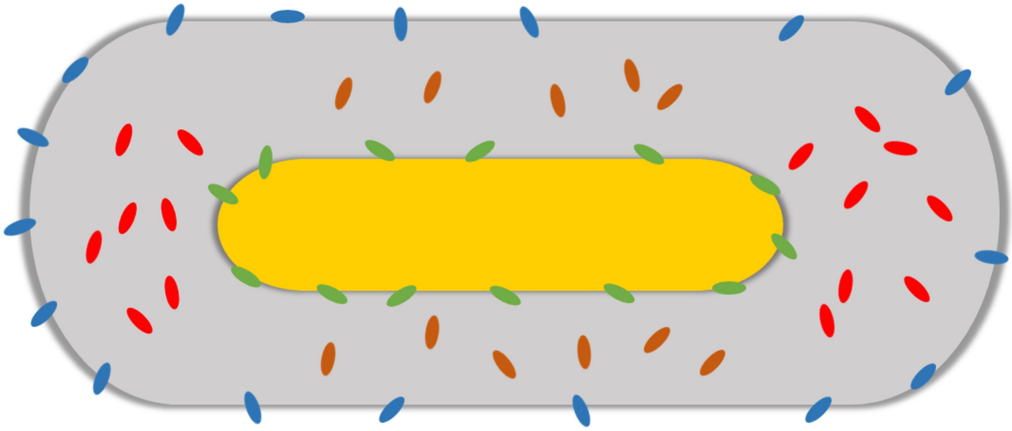

Fig. IV.12. Pictorial representation of the different location of $\mathbf{Ir_1}$ in AuNR@($\mathbf{Ir_1}$)SiO_2@TPSA. Green ellipses represent $\mathbf{Ir_1}$ directly in contact with gold surface; red ellipses refers to a localization into silica matrix tip zone, while brown colour indicates a localization into silica matrix side zone. Finally, blue ellipses represent $\mathbf{Ir_1}$ on the silica surface.

The intermediate weak band at 515 nm of AuNR@($\mathbf{Ir_1}$)SiO_2@TPSA, fixed at the same position of the band in the emission spectra of the other samples, refers to fluorophore in the silica matrix and on the silica surface, which show a biexponential decay, as in the homologous AuNS@($\mathbf{Ir_1}$)SiO_2@TPSA (Fig. IV.13). Obviously, while in the nanospheres we measure a 408 ns and 1210 nm, in the nanorods we measure 204 ns and 964 ns, plus the short 8 ns lifetime; as already mentioned this is due to the fitting procedure of lifetime decay measured on overlapping bands.

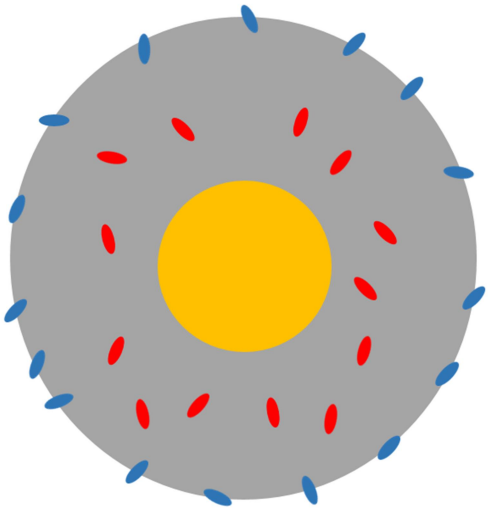

Fig. IV.13. Pictorial representation of the different location of $\mathbf{Ir_1}$ in AuNS@($\mathbf{Ir_1}$)SiO_2@TPSA. Colours identical to those of figure IV12 correspond to the same location of $\mathbf{Ir_1}$

Finally, the low-energy band at 542 nm, which shape is characteristic of **Ir_1** emission, but strongly red-shifted, can be attributed to the specifity of the plasmonic field in a rod-shape nanoparticle. In this case, the intensity of the plasmonic field is greater on the tips than on the sides (§ I.4), and the **Ir_1** molecules entrapped into silica matrix in the tip zone, experience a more intense field. This determines a red-shift of the emission band [6], and a reduced lifetime value, as evidenced by the 1060 ns value compared to the 1210 ns corresponding value in the homologous AuNS@(**Ir_1**)SiO_2@TPSA sample.

Concerning the assisted system AuNR@SiO_2@TPSA + **Ir_1**, the emission spectrum show a unique band at 515 nm, whit a corresponding lifetime of 392 ns. These values are equivalent to those of the **Ir_1** free in solution, confirming that, at the concentrations used, no relevant interactions between fluorophore and AuNRs have been detected.

The direct contact of the **Ir_1** fluorophore with the metal surface origines the metal enhaced fluorescence. To better confirm this, we prepared AuNR@SiO_2(**Ir_1**)SiO_2@TPSA that differs from AuNR@(**Ir_1**)SiO_2@TPSA because fluorophore was added after the first TEOS addition (*i.e.* between the first and the second TEOS addition, see protocol *"Synthesis of AuNR@SiO_2@TPSA"*): in this way **Ir_1** was placed onto the first layer of silica shell, so avoiding the direct contact with metal surface. In Fig. IV.14 we reported the emission spectrum of the sample AuNR@SiO_2(**Ir_1**)SiO_2@TPSA that doesn't shows the features attributed to MEF. By comparing this spectrum with that one obtained from AuNR@(**Ir_1**)SiO_2@TPSA we safetely evidenced the absence of MEF due to the absence of a direct contact fluorophore-metal.

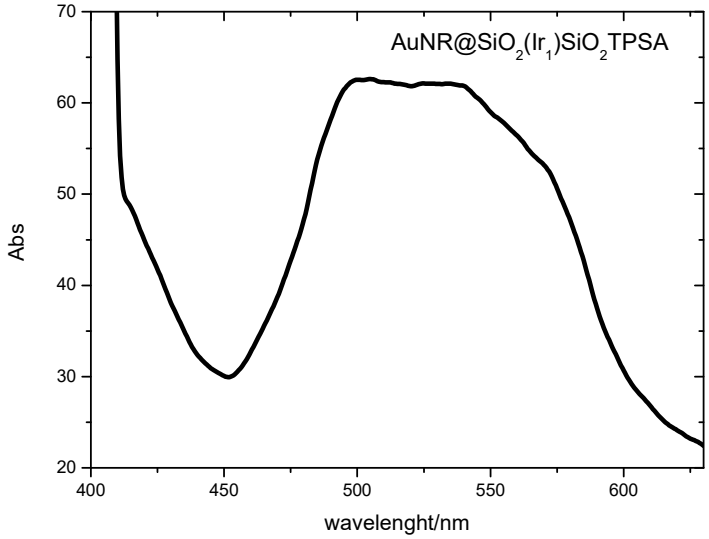

Fig. IV.14. Emission spectra of AuNR@SiO_2@SiO_2@TPSA obtained by exciting the Ir(III) complex at 390

IV.3. Conclusions

The collected data show that the luminescence properties of **Ir_1** can be modified when it interacts with gold nanoparticles. In particular, the extend and the way depends on the overlap between the **Ir_1** emission band with the AuNPs plasmonic band, and on the distance between the chromophore and the metallic nanoparticle.

In general, band overlap can be tuned by selecting the proper chromophore and/or the shape and size of AuNPs, while the distance can be regulated by the silica shell growth process.

By comparing different samples, it can be concluded that green luminescence of **Ir_1** is quenched by an energy transfer process towards the transversal plasmonic band of AuNRs (or by the single plasmonic band in AuNSs) positioned at about 520 nm. This transfer process was observed only in the functionalised system, while was absent in the assisted system (at least at the used concentrations).

More interestingly, lifetimes studies allow inferring the chromophore localization into silica shell, *i.e.* in the matrix or on the surface. In the case of Au nanorods, it was evidenced a more structured photophysics, that suggest to identify a tip and a side zone into the silica shell, where the intensity of the plasmonic field is different. Finally, a particular spectral feature, *i.e.* a blue band on which was measured a very short decay, led us to suppose a MEF effect, attributed to the fraction of **Ir_1** directly in contact with the metal surface.

REFERENCES

1. L. Jiang, H. Mundoor, Q. Liu, I. I. Smalyukh, *ACS Nano,* **2016**, 10, 7064
2. L. Ricciardi, M. Martini, O. Tillement, L. Sancey, P. Perriat, M. Ghedini, E. I. Szerb, Y J. Yadav, M. La Deda, *J Photochem Photobiol B*, **2014**,140, 396 (a) L. Ricciardi, T. F. Mastropietro, M. Ghedini, M. La Deda, E, I. Szerb, *J Organomet Chem,* **2014***,* 772-773, , 307 (b)
3. a) R. D. Costa, F. Monti, G. Accorsi, A. Barbieri, H. J. Bolink, E. Ortí and N. Armaroli, *Inorg. Chem*., **2011**, 50, 7229; b) J. M. Fernández-Hernández, C. H. Yang, J. I. Beltrán, V. Lemaur, F. Polo, R. Fröhlich, Jêrôme Cornil and L. De Cola, *J. Am. Chem. Soc., **2011***, 133, 10543
4. R. D. Costa, E. Ortì, H. J. Bolink, F. Monti, G. Accorsi, N. Armaroli, *Angew. Chem. Int. Ed.* **2012**, 51, 8178
5. J. R. Lakowicz, Principles of Fluorescence Spectroscopy Third Edition, *Springer*, **2006**
6. L.Zhao, T. Ming, H. Chen, Y. Liang and J. Wang, *Nanoscale*, **2011**, 3, 3849

V. ASSEMBLED GOLD NANORODS AND THEIR PLASMONIC BEHAVIOR

V.1. Gold nanorods direct assembly

V.2. Gold nanorods indirect assembly

Current methods for assembling gold nanoparticle superstructures involve (§I.3) **direct interactions** through interparticle forces (depletion forces [1], molecular interactions [2]) or **indirectly** using a template (liquid crystal [3]).

Assembly through *direct interactions* is the results of the balance between the acting forces, *i.e.* the strength of the depletion forces (due to the shape of the nanoparticles) and the strength of the intermolecular interactions (due to the nanoparticles molecular cover), ranging from the weak van der Waals interactions to the strong hydrogen bond) [4]. It can be observed that in AuNRs coated with multilayers of surface-adsorbed cationic surfactants, such as CTAB, a remarkable order degree of gold nanoparticles is induced, due to a balance between short-range electrostatic repulsion and interchain attraction (§I.3 Solvent evaporation-induced assembly) [5]. Assembly of gold nanoparticles driven by strong interactions have been observed when thiol-functionalized derivatives [6] have been used as binder. Gold–thiol bonding chemistry is commonly utilized for completely or partially functionalizing the surface of AuNR. Large thiol-terminated polymers with high molecular weights, such as poly(ethylene glycol)s (PEGs) and DNAs, have particularly been employed for functionalization. Thiol molecules have been found to preferentially bond to the two ends of AuNR at low concentrations, which has been attributed to the smaller packing density of CTAB at the highly curved ends [7]. The CTAB molecules, adsorbed on AuNRs, act as templates for the deposition of the hydrolyzed TEOS species onto the NRs (§ III). The thickness of the mesostructured silica coating can be tuned with the consequence to modulate the distance between assembled AuNRs and control the plasmonic properties. In fact, organized superstructures of AuNRs show an optical appearance different from the isolated NRs; this is attributed to the plasmon coupling (§ I.5). The effectiveness of the coupling depends on the distance among the nanoparticles and on the efficacy of the NPs' coating to modulate the plasmon field.

In order to successfully exploit nanoparticle assembly in technological applications, and to ensure efficient scale-up, a high level of control is required and, generally, achieved using templates. *Indirectly assembly* consist of a matrix ordered confinement (§I.3 Assembly using templating method) such as liquid crystals, considered suitable substrates for nanoparticle assembly.

On this basis, we explored the assembly of different coated AuNRs and the related optical behaviour.

V.1. Gold nanorods direct assembly

Direct assembly of AuNrs is obtained when interparticles forces are active to arrange nanoparticles. As already discussed, these forces originate from shape affinity and/or chemical interactions of the NRs coating. Because is possible to cover NRs preferentially on the tips or on the side, or indifferently on the total surface, it is possible to distinguish between a *regio-selective* or *non regio-selective* coating, respectively. In the first case, a directional assembly of NRs is expected.

Non regio-selective coating. AuNR@CTAB sample, prepared as reported in § II.1, has been deposited onto carbon grid TEM. Ordered nanoparticles involving side-by-side and end-to-end arrangement, associated with the drying process, are visible (Fig.V.1). Depletion forces allow the NRs arrangement, the high order degree is due to high monodispersity of the sample, and no directional assembling is observed because interchain interaction between CTAB NRs coating is *non* regio-selective.

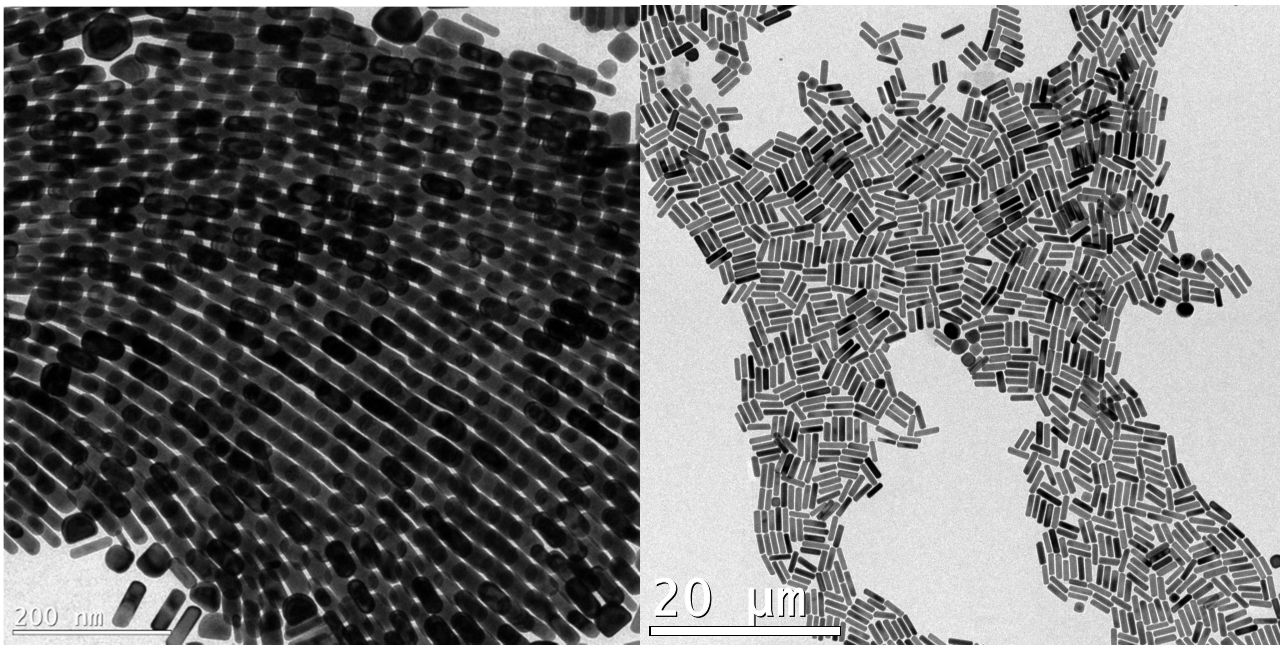

a) b)

Fig. V.1. TEM images (a) and (b) of ordered AuNR@CTAB involving side-by-side and end-to-end arrangement

TEM images show clearly vortical assembly (Fig.V.2); this particular behaviour has been reported in literature [8], where it is attributed to a local flows inside the solvent are often induced by spatially non uniform temperature gradients or local concentrations. Generally, this phenomenon is

rarely observed; in the present case, solvent evaporation from NRs sample was reached by heating the TEM grid, rather than allowing the solvent to evaporate at room temperature, and probably this causes vortex formation.

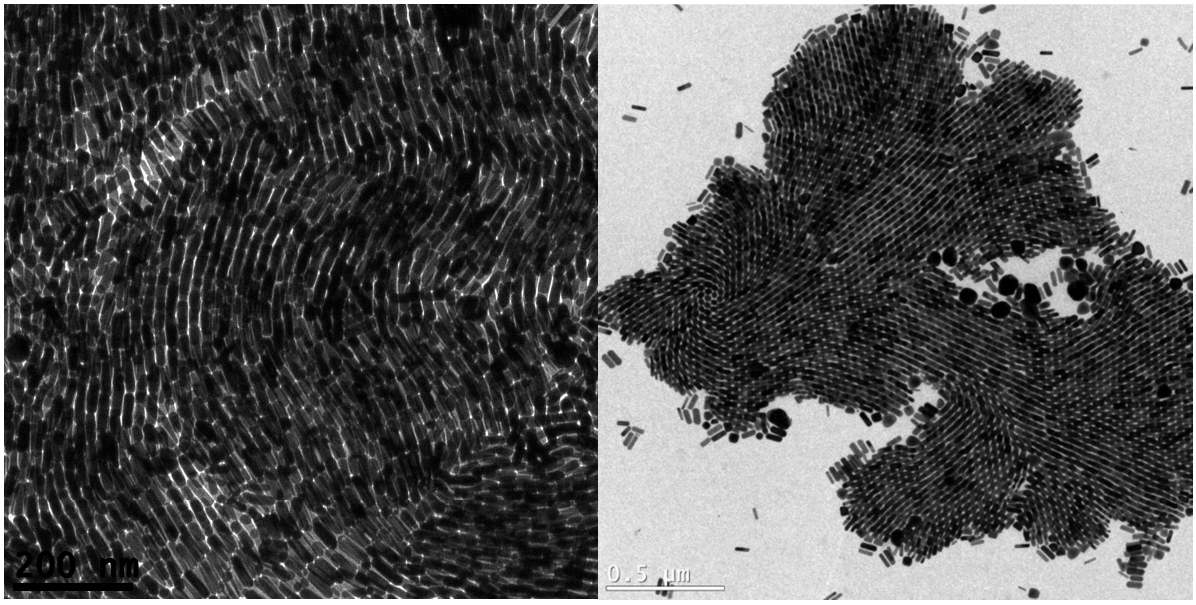

a) b)

Fig.V.2. TEM images (a) and (b) of AuNR@CTAB vortical assembled

Because in the case of AuNR@CTAB, the driving assembling force is the capillary one, different arrangements are visible by observing different region over the TEM grid. Particles organize into a close packed structure (like ribbon) in the region between the center and the edge of the drop on TEM grid, as can be observed in Fig. V.3.

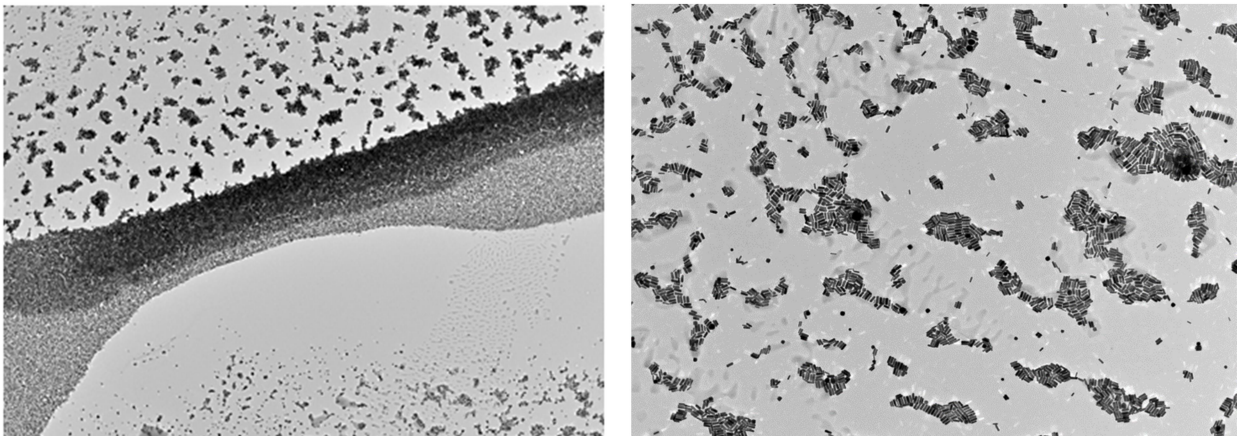

(a) (b)

Fig.V.3. TEM images (a) and (b) of AuNR@CTAB assembled like ribbons

Another example of colloidal assembly, that confirm the actions of the capillary force in determining the NRs assembly, is the formation of a coffee ring like deposit (Fig V.4.). By decreasing the sample concentration, the particles in the edge become depleted of the fluid, and their interstices act as capillaries that drive a strong outward, radial flow that carries nearly all the solute to the edge. The velocity of the flow is dictated by evaporation rate, which is diffusion limited, as the vapour must be removed from the top of the fluid.

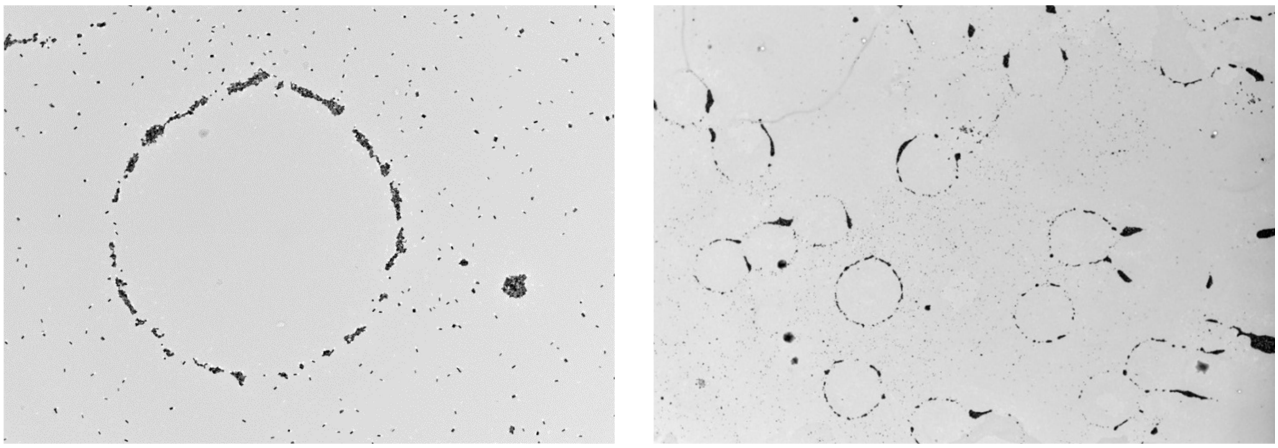

a) b)

Fig.V.4. TEM images (a) and (b) of AuNR@CTAB assembled like ribbons

These assembled superstructures of AuNR@CTAB are expected to show a coupling of the plasmonic bands, due to the proximity of the nanoparticles. Extinction spectra of these samples have been collected, but their quality is very poor. Also in literature was impossible to find excitation spectra of AuNR@CTAB deposited onto transparent glass. Instead, in order to explore the occurrence of the coupling among AuNRs, we prepared four samples of AuNR@SiO_2 (§III) taking into account that the reciprocal distance between nanorods can be tuned by controlling their silica thickness. In this way, we could modulate the optical response.

The prepared silica-coated AuNR samples are:

1) AuNR@SiO_2, with thickness 24 nm x 16 nm (long axis x short axis);
2) AuNR@SiO_2, with thickness 13 nm x 8 nm (long axis x short axis);
3) AuNR@SiO_2, with thickness 10 nm x 5 nm (long axis x short axis);
4) AuNR@SiO_2, with thickness 5 nm x 3.5 nm (long axis x short axis).

All these samples have been analysed by TEM and by optical spectroscopy. In particular, we compared extinction spectra from ethanol solution and from film obtained by solvent evaporation of drop-casted solution onto quartz windows. In this way, taking into account that no assembly, and consequently no coupling, are present in solution, any difference should be attributable to AuNRs interaction.

Sample #1 24 nm x 16 nm. Observing the TEM images (Fig. V.5.) it is visible a high degree of assembling, but the superimposition between the spectrum in solution (where assembly is absent, and consequently any coupling effect is absent) and the spectrum of the film (Fig. V.6.) accounts for the absence of coupling. According to the literature [9], this is due to the silica shell that is too thick to permit the plasmon interaction.

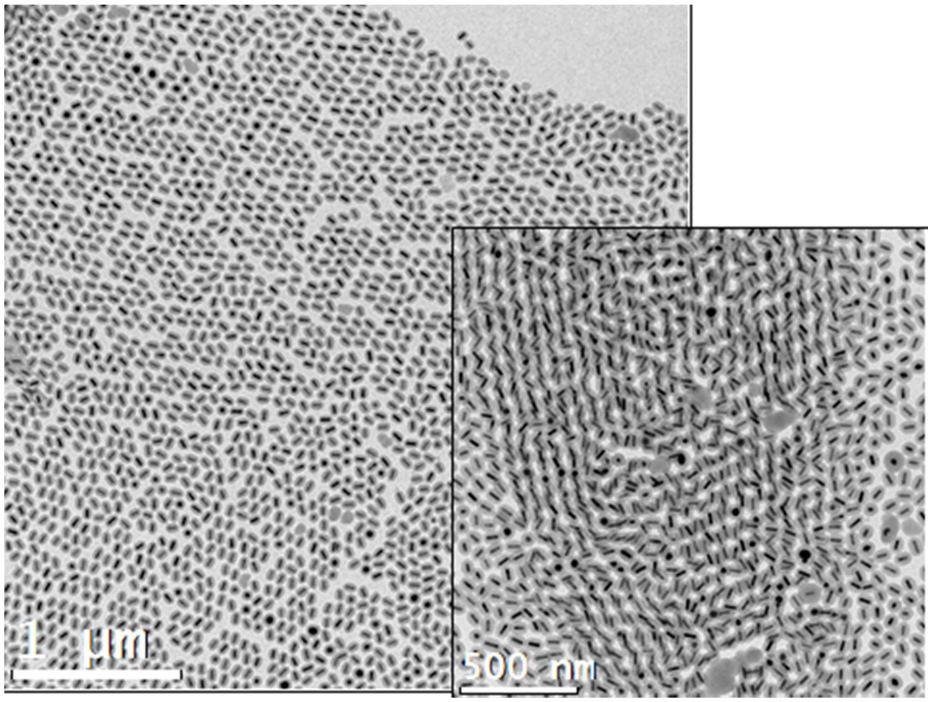

Fig V.5. TEM image of assembled AuNR@SiO_2

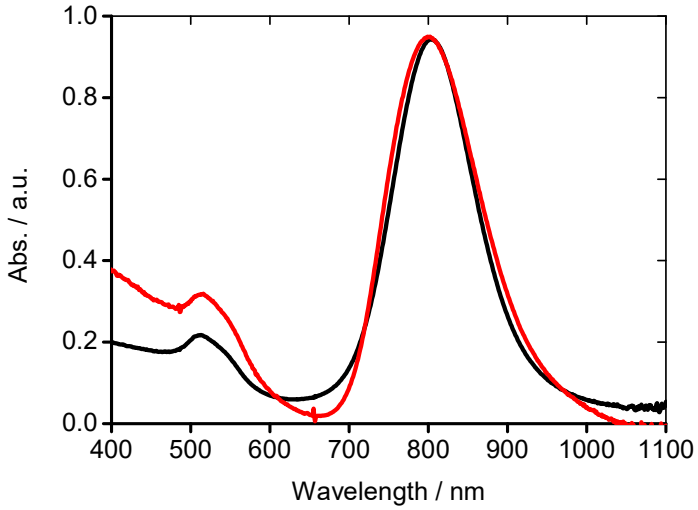

Fig.V.6. Extinction spectrum of AuNR@SiO_2 from ethanol solution (black line), and from film sample (red line)

Sample #2 13 nm x 8 nm. Observing the TEM image (Fig. V.7.) we noted the nanoparticles' tendency to stay as closed as possible, but, although the silica thickness is reduced respect the previous sample, from 24 nm x 16 nm to13 nm x 8 nm, no spectral changes were noted: the superimposition between the spectrum in solution and the spectrum of the film (Fig. V.8.) accounts for the absence of coupling. The little blue-shift of the longitudinal band of film sample respect to that of the solution one (hardly observable also in the previous sample), is attributed to the high sensitivity of this band to the refractive index variation on passing from ethanol (n_d^{20} =1.34) to air (n_d^{20} = 1.00).

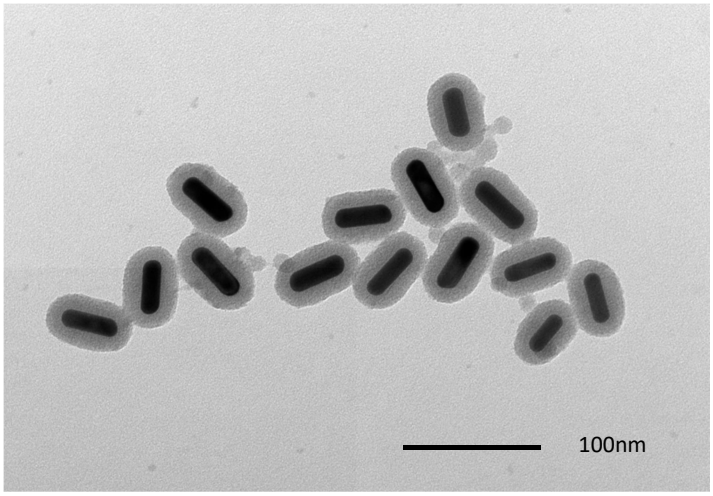

Fig.V.7. TEM image of AuNR@SiO_2

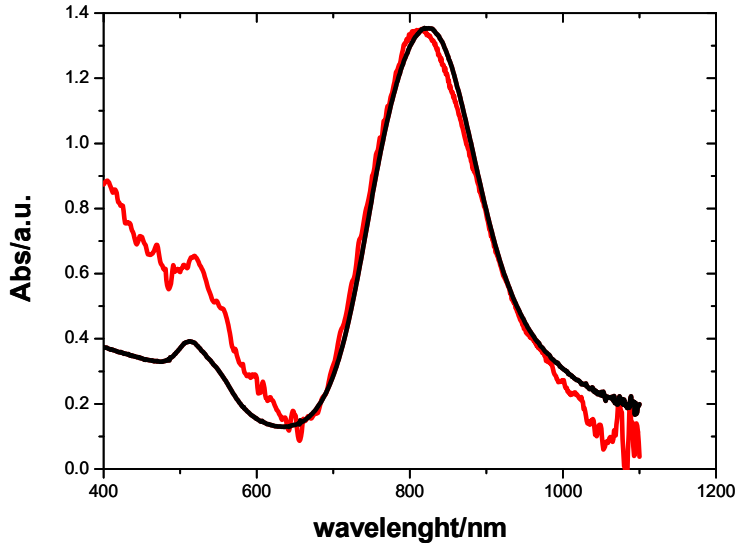

Fig.V.8. Extinction spectrum of AuNR@SiO_2 from ethanol solution (black line), and from film sample (red line)

Sample #3 10 nm x 5 nm. Observing the TEM images (Fig. V.9), we noted that, due to the reduced silica thickness (now 10 nm x 5 nm), the distance between gold core appears reduced. In this case the spectrum of the solution and the spectrum of the film (Fig. V.10) are different; in particular, the longitudinal plasmonic bands of the film spectrum is red-shifted and broadened compared to that of the spectrum in solution. This behaviour is attributed to the coupling of the plasmonic fields [9], allowed by the shortened distance among gold cores.

.

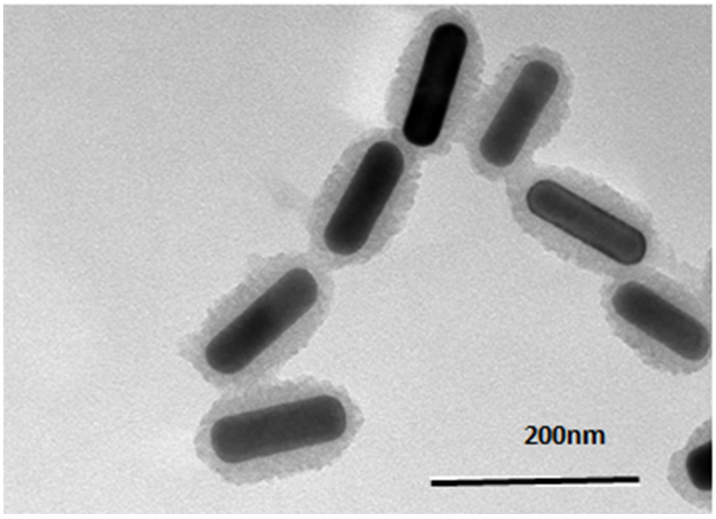

Fig.V.9. TEM image of AuNR@SiO_2

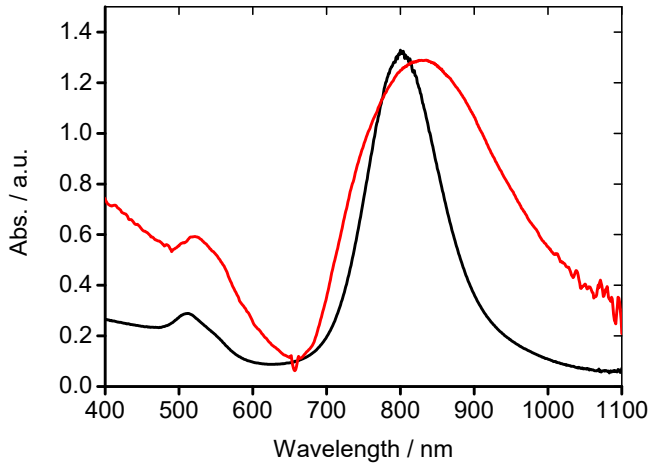

Fig.V.10. Extinction spectrum of AuNR@SiO_2 from ethanol solution (black line), and from film sample (red line)

Sample #45 nm x 3.5 nm. Observing the TEM images (Fig. V.11) the silica shell thickness is so thin as to be barely visible. The longitudinal plasmonic band of the spectrum of the film, compared to the spectrum in solution, is red-shifted (Fig. V.12), but it is impressive the broadening of the band of the film sample. This behaviour is attributed to the coupling of the plasmonic fields, allowed by the shortened distance among AuNRs gold core due to very thin silica shell of 5 nm x 3.5 nm.

Fig.V.13. TEM image of AuNR@SiO_2

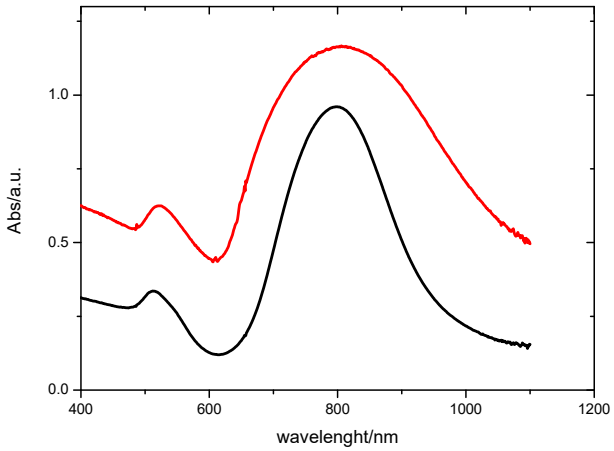

Fig.V.14. Extinction spectrum of AuNR@SiO_2 from ethanol solution (black line), and from film sample (red line)

Non regio-selective coating of AuNRs allows a direct assembling of nanoparticles, which has been observed by TEM. Plasmonic coupling is not easy to observe when CTAB bilayer covers AuNRs, while can be observed in the case of silica coating. Precisely, the effectiveness of the coupling depends on the reciprocal distance of the gold cores, which, in turn, depends on the silica thickness. We analysed samples in which the distance between the nanoparticles gold core is modulated by the silica thickness. By measuring the edge-to-edge distance between the gold core of the examined samples, we found that it shortens by decreasing the silica thickness, so allowing a better coupling. We found that coupling of the plasmonic fields is effective when the distance between nanoparticles it is not higher than 10 nm, *i.e.* samples #3 and #4. When the distance is greater, no nanorod interacts each other and no difference is visible between the solution and the solid spectra.

Regio-selective-coating. Two features are necessary to obtain a directional assembling of the nanoparticle building blocks through a direct interaction of the capping molecule: a regio-selective distribution on the surface of the nanoparticles of the capping molecules with two active groups, allowing a link between nanorods. According to the literature, thiol molecules can direct the spatial nanorods arrangement. Exploiting the high gold affinity of -SH group, an additional sterical control can drive an end or side AuNRs functionalization.

Liz-Marzán and others [10] report experimental and theoretical demonstration regarding the hydrogen-bonding mechanism behind the end-to-end assembly of AuNRs. In particular, they indicate that hydrogen bonding between protonated and unprotonated linking molecules is responsible for nanorod assembly in aqueous solution. Figure V.15 shows a pictorial representation of the linear self-assembly, proposed by Thomas et al. [10], of AuNRs covered with CTAB and thiol-functionalized carboxylic acid at their sides and tips, respectively. This behaviour is attributed to the smaller packing density of CTAB at the highly curved ends, [7] consequently, thiol molecules have been found to preferentially bond to the two ends of AuNRs.

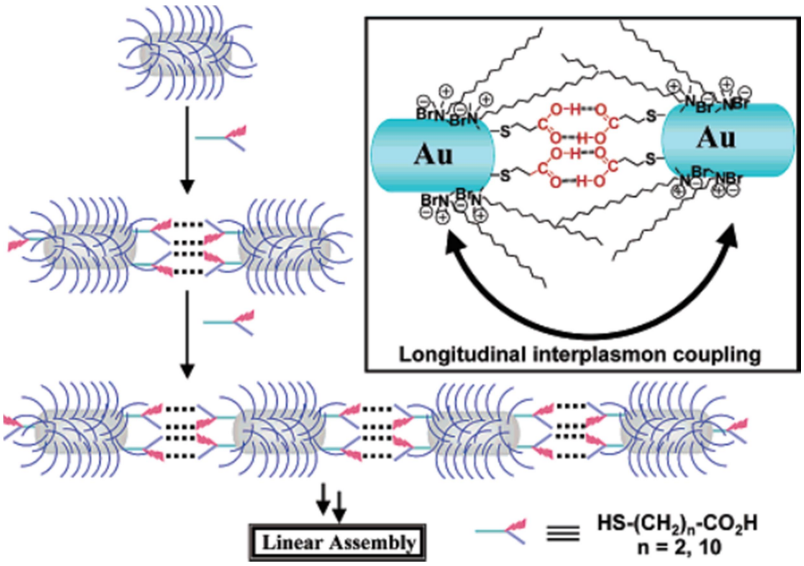

Fig. V.15. Intermolecular hydrogen bonding between thiol functionalized carboxylic acid on adjacent nanorods [10].

On this basis, we prepared and analysed, by TEM and optical spectroscopy, AuNRs stabilized with different capping agents, and studied their organization with and without pH control. The pH-controlled strategy is based on the covering of AuNRs with PEG-SH and lipoic acid (LA, in Fig.1.13) at their sides and tips, respectively [11]. The presence of lipoic acid at the tips

dramatically changes the plasmonic features of the AuNRs at a pH = 5, corresponding to the pKa of LA.

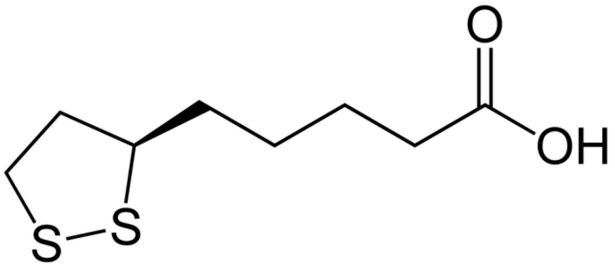

Fig.1.16. Structural formula of Lipoic cid

The prepared AuNRs samples are:

1) AuNRs covered with PEG-SH in water solution;
2) AuNRs covered with PEG-SH and LA in water solution;
3) AuNRs covered with PEG-SH and LA in acidic water solution by HCl (pH=5);

We recorded extinction spectra from solution and from film obtained by solvent evaporation of drop-casted solution onto quartz windows.

Sample #1. According to the protocol previously reported, (§II.2) we synthesized AuNR@PEG-SH from AuNR@CTAB. The longitudinal plasmonic band of the spectrum of the film sample (Fig.V.17 a), compared to the spectrum of the solution (FigV.1.14. b), is red-shifted and broadened suggesting a plasmon coupling (§I.5), allowed, as shown in TEM image (Fig. V.18), by the close proximity among the nanoparticles.

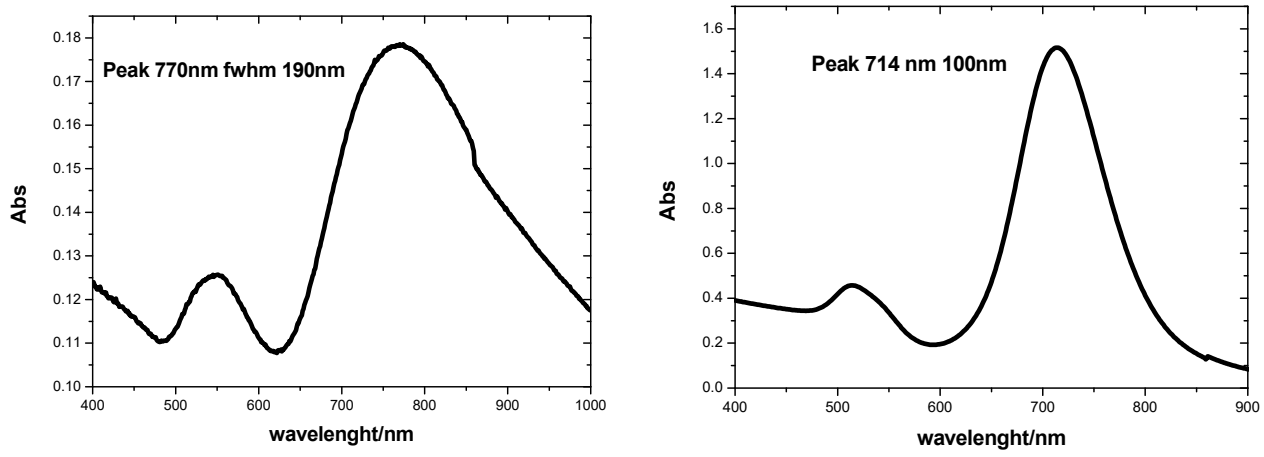

a) b)

Fig.V.17. Extinction spectrum of AuNR@PEG-SH: (a) film sample, (b) water solution.

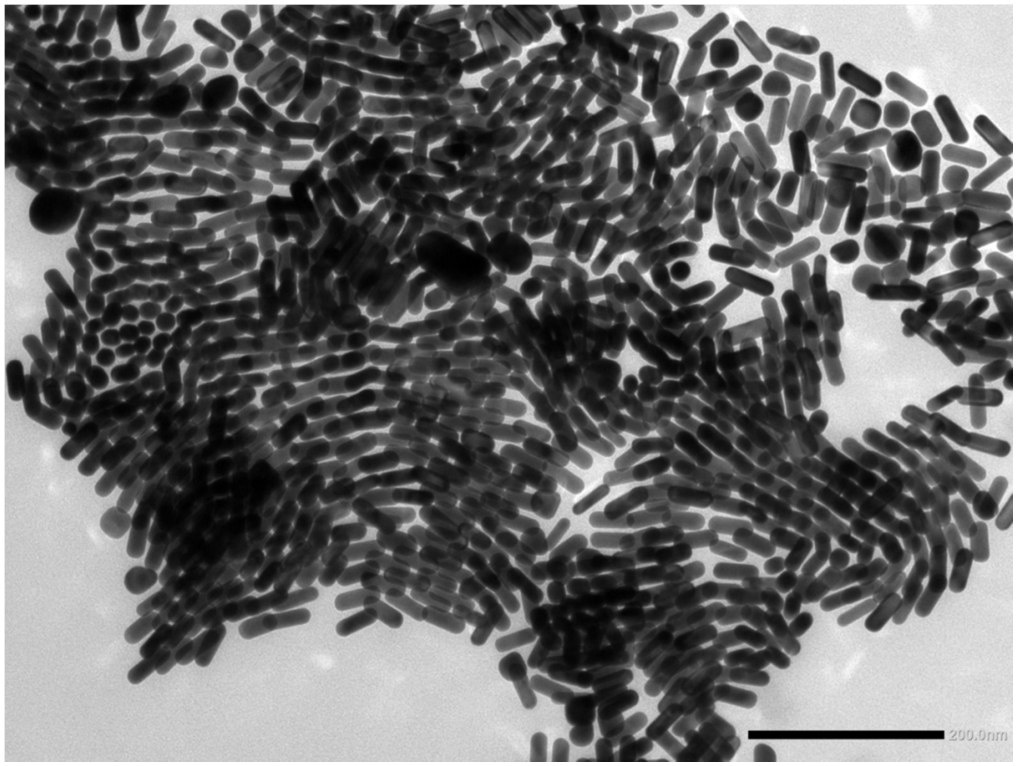

Fig.V.18. TEM image AuNR@PEG-SH

Sample #2. Modifying the protocol of the reference [11], we synthesized AuNRs covered with PEG-SH and LA, AuNR@PEG-SH/LA. We centrifuged AuNR@PEG-SH (4.0 E-4 M) and redispersed them in a buffer solution (pH 8) of LA (1.0 E-3 M as the final concentration). The mixture was stirred for 1 h and left undisturbed for 2 h at room temperature. Then, the AuNRs were centrifuged twice (at 4500 rpm for 20 min) and redispersed in water. The results obtained by optical spectroscopy are similar to those reached in sample #1: the longitudinal plasmonic band of the spectrum of the film (Fig.V.19 a), compared to the spectrum in solution (FigV.20 b), is red-shifted and broadened. The introduction of the LA on the AuNRs does not modify appreciably the arrangement of nanoparticles (TEM image in Fig. V.1.16).

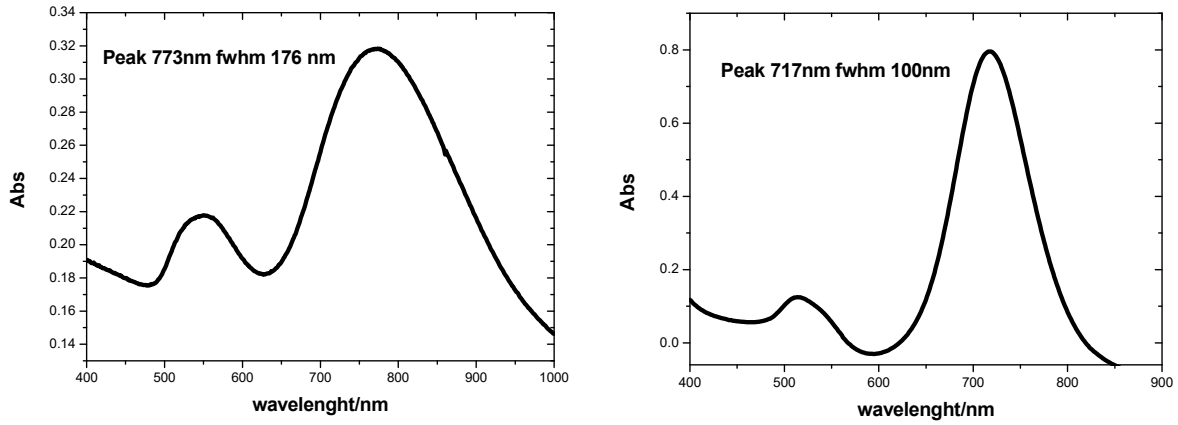

a) b)

Fig:V.19. Extinction spectrum of AuNR@PEG-SH/LA: (a) film sample, (b) water solution.

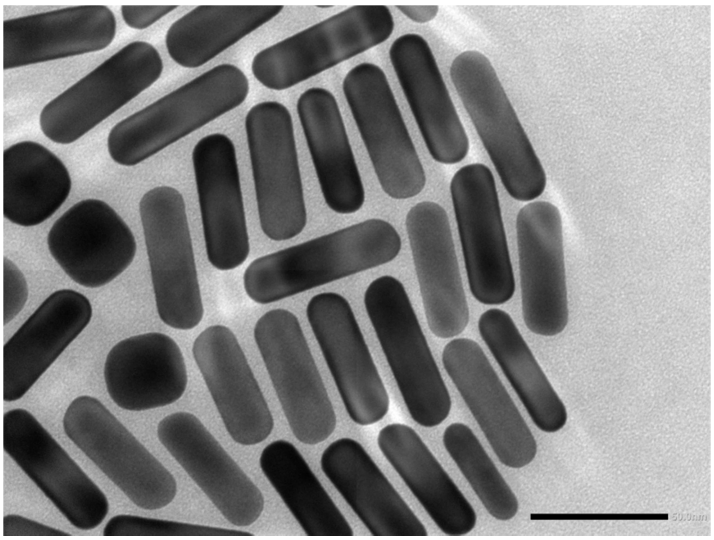

Fig. V.20. TEM image AuNR@PEG-SH/LA

Sample #3. Also in this case we followed the procedure used for Sample #2, but we redispersed AuNR@PEG-SH/LA in a water solution acidified by HCl at pH=5. TEM images (Fig.V.21) shows a clear end-to-end organization of nanoparticles. Optical spectroscopy (Fig.V.22) shows a red-shift and broadening of the longitudinal plasmonic peak of the film sample (a) compared to that of the solution (b).

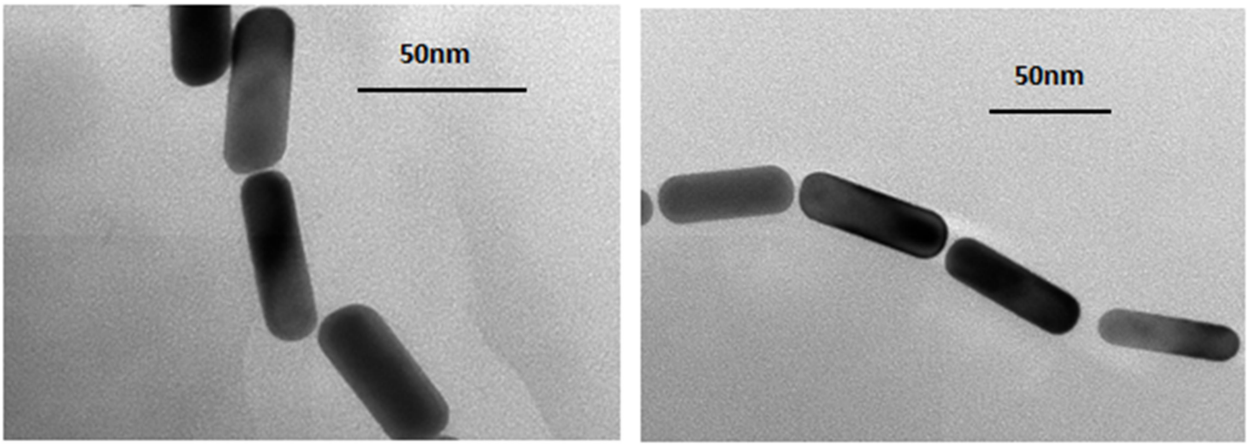

Fig.V.21. TEM images of AuNR@PEG-SH/LA

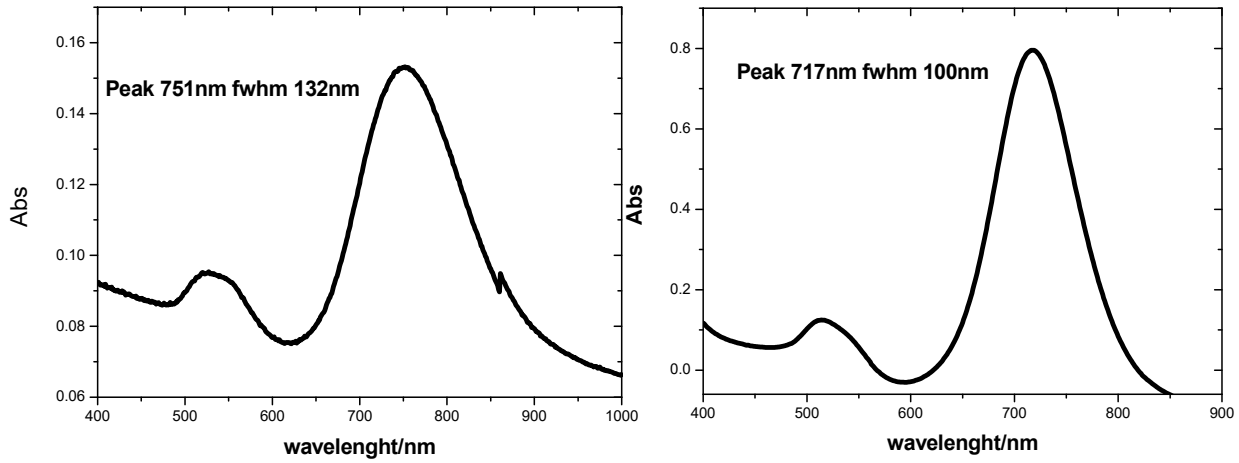

a) b)

Fig:V.22. Extinction spectrum of AuNR@PEG-SH/LA: (a) film sample, (b) water solution.

Thiol group, which adheres to gold by a strong S-Au bond, dislodges CTAB molecules from the gold surface, on which they are held by electrostatic interactions (§ III).

Two kinds of thiol-functionalized molecules are used to cover the nanorods surface: PEG-SH with high steric hindrance, and LA with less steric hindrance. The first ones, although arrange on the whole nanorods surface, will be in a greater quantity on the sides due their steric hindrance. Consequently, the latter will prefer to bind on the tips. All examined film samples show the presence of plasmon coupling, as demonstrated by red-shift and broadening of the longitudinal band, respect to the solution.

TEM images of AuNR@PEG-SH/LA, at neutral pH, do not show any variation in the nanoparticles arrangement respect to the AuNR@PEG-SH, and consequently spectroscopy results unvaried by comparing sample #1 with sample #2. Instead, when the pH value allows hydrogen bond formation among the tips of the LA-functionalised AuNRs, an end-to-end arrangement is achieved, as demonstrated by TEM image of a sample #3. Spectroscopy shows a reduced broadening of this film sample compared to the other film samples, and a less red-shift. Taking into account that the broadening of the longitudinal band is generally attributed to the presence of polydispersion of the active objects, the reduced broadening in sample 3 suggests an increased monodispersion of the *organized NRs*, respect to the other sample, that means that nanorods are driven towards a preferential spatial organization. The reduced red-shift could be attributed to a reduced numbers of interacting NRs; for this reason the energy requested to induce the collective oscillation of the surface electrons result increased.

V.2 Gold nanorods indirect assembly

In order to obtain a nanoparticle's assembly, in addition to stimuli responsive interparticle interactions and morphological or functional features, recent advances have focused to maximize the nanoparticle's organization into a template. The template is considered as any object serving as a scaffold onto which different particles can be arranged. With this picture in the mind, a variety of elements can be considered as templates. A promising approach is the assembling of nanoparticles with the liquid crystals (LCs) ordered templates, which are able to rapidly self-arrange into large ordered anisotropic matrices which, in addition, can contain linear structural defects (§ I.3) [12].
The liquid-crystalline state is intermediate between that of a perfectly ordered crystal and a disordered isotropic liquid. The moieties within a liquid crystal possess intrinsic directional order, often accompanied by various degrees of positional order, whilst remaining in a fluid state. A material that exhibits a liquid-crystalline state as a function of temperature is referred to as thermotropic, whereas those that exhibit a LC phase in relation to a concentration in a solvent, they are known as lyotropic [13].

Liquid-crystalline materials offer unique opportunities in the field of nanoparticles (NPs) organization due to the intrinsic order and fluid properties that they possess, allowing complex architectures to be established with high processability. In fact, the organization of nanomaterials in two- or three-dimensional space, offered by the LC medium, seems to be an ideal vehicle to explore and control the organization of matter on the nanometre scale [14]. Historically, the concept of doped liquid crystals was born due to the demands of a growing display industry by means of a ‘‘guest–host’’ effect demonstration. Pleochroic dyes were the first ‘‘guest’’ dopants to a liquid crystal ‘‘host’’ which served as a tuneable ordering matrix: anisometric molecules of organic dyes were aligned along a preferred orientation of liquid crystal [15].

The synthesis of LC–NP hybrids is of course largely determined by the nature of the nanoparticle, and is affected by factors such as the NPs synthetic method and, in particular, their surface chemistry. Precisely, for this reason, it is necessary to first coat the NPs with a suitable material that allows the particles to mix without aggregates caused by segregation with the “host” LC. Our challenge is to prepare **LC–AuNRs hybrids** and to investigate, by optical spectroscopy, the AuNRs array. We used as LC the well-known 4-Octyl-4’-Cyanobiphenyl (8CB), a thermotropic liquid crystal showing smectic A and nematic mesophases [16] (Fig.V.23). We synthesized AuNRs covered with L_1 (§II.2), and prepared a 1% w/w chloroform solution by mixing AuNR@L_1 chloroform solution with 8CB. The mixture was placed onto a quartz window, and, after solvent

evaporation, the sample appeared pink for the presence of the nanorods. No aggregates were visible, suggesting a mixture between AuNR@L_1 and 8CB.

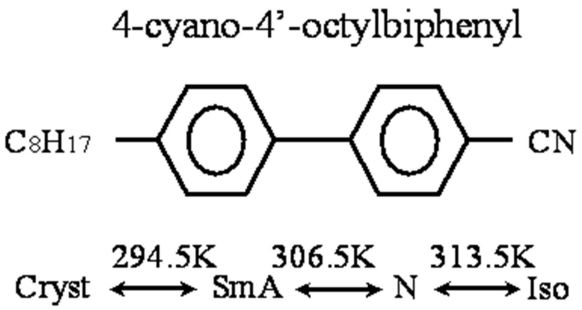

Fig.V.23. Chemical formula and phase sequence of 8CB

We registered extinction spectra of the 8CB-AuNR@L_1 mixture at 300 K (where LC is in smectic phase) and 333 K (where LC is in isotropic phase), as reported in Fig. V.24: we didn't verify difference (*e.g.* longitudinal band fwhm increase, whose presence indicates the presence of NPs assembling) between the two spectra, unless for a blue-shift of the longitudinal band with increasing the temperature, which is probably ascribable to a reduced refraction index of the LC matrix. We can therefore state that there is no variation in the organization of the nanorods passing from an isotropic to an anisotropic phase.

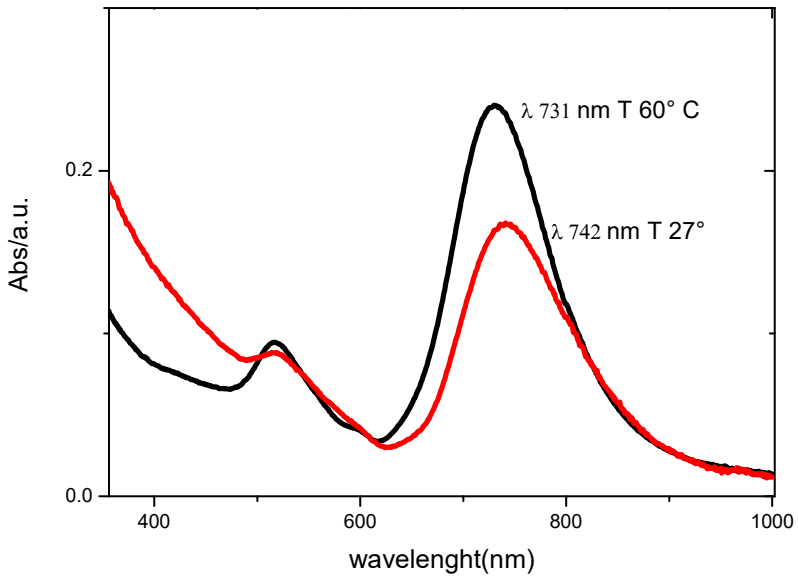

Fig. V.24. Extinction spectra of 8CB-AuNR@L_1 at T=27° C (red line), and at T=60° C (black line). In the inset, a TEM image of the LC-NP mixture is reported.

We tried to assemble AuNR@L_1 in defect lines arrays created in liquid crystal exploiting periodic arrangements of twisted domains with opposite handedness. The experiments were carried out on asymmetric nematic cells [17] in which one surface imposes a strong uniform planar alignment, while the other provides a periodic planar alignment. The former is obtained by a 20 nm-thick layer of polyvinyl alcohol (PVA, 87% hydrolyzed) spin-coated on a glass substrate and uniaxially rubbed using a velvet-wrapped roller. The second one is a polarization sensitive photoaligning layer of a dichroic sulphuric bis-azobenzene dye, spin-coated on glass from a dimethyl formamide solution (0.5 % by weight). The empty cells, with thickness in the range of 5–10 μm, were exposed for 120 s to the spatially rotating linear polarization pattern produced by the interference of two coherent Gaussian beams of equal intensity (60 mW/cm^2), wavelength λ=458 nm, and orthogonal circular polarizations. The plane of incidence was oriented perpendicular to the uniform anchoring direction on the PVA surface, and the spatial periodicity of the polarization pattern Λ= 50 μm was kept constant. We infiltrated 8CB-AuNR@L_1 into the cells by capillary action above the clearing temperature and then slowly cooled down in the smectic phase to the room temperature. The asymmetric anchoring conditions yield either planar or twisted configurations depending on whether the local easy axis on the photo-aligning layer is parallel or not with respect to the rubbing direction of the PVA-coated substrate. Moreover, a periodic array of disclination lines is expected, due to the distruption of the orientational order in the regions where the right- and left-handed twisted domains meet. By polarizing microscope we confirmed the presence of smectic order and the periodic array of disclination lines.

In order to study the arrangement of the NPs on the whole surface of the cells, we recorded the extinction spectrum in different points, observing a reduction of the AuNR@L_1 absorbance measured on the side where was infiltrated the sample with the opposite side. This behaviour is due to a limited diffusion of the mixture into the cell, so the concentration of nanorods is greater on one side than on the other. More interesting is the observation that no differences have been found by comparing AuNR@L_1 extinction spectra recorded from the uniformly aligned smectic area with those from the disclination lines array (fig. V.25): **this accounts for a similar NRs organization into both the environment.**

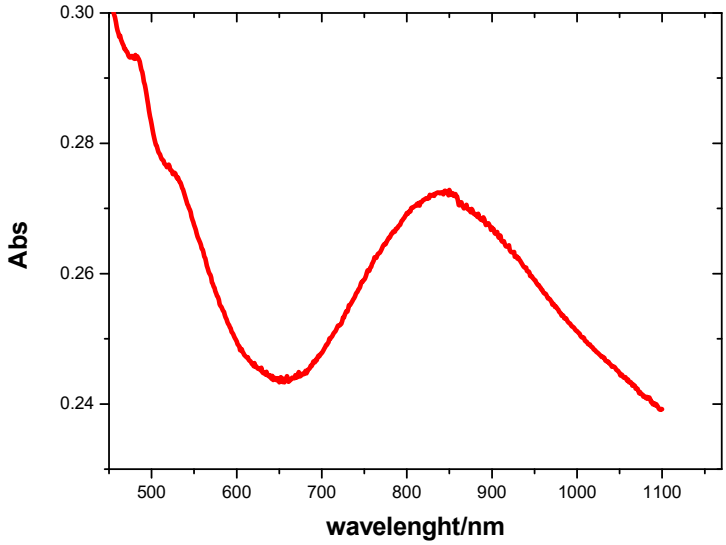

Fig.V.25. AuNR@L_1 inside liquid crystal environment

By comparing spectrum obtained from cell (reported in Fig. V.25) with that obtained from mixture placed onto quartz window (fig. V.24), the longitudinal band is red-shifted (passing from 742 nm to 840 nm) and broadened (fwhm from 130 nm to 200 nm). This suggests that LC organized into the cell acts as an orienting medium for AuNR@L_1, while the smectic organization onto quartz window is unable to drive nanorods assembly.

The longitudinal and transversal localized plasmon resonances of AuNRs are basically independent of each other, they can be selectively excited by using light polarized with the oscillating electric field parallel and perpendicular to the long axis of the rod, respectively [18]. On this basis, and according to Lacaze [19], we compared the extinction spectra of AuNR@L_1 in cell illuminated by polarized light in a zone where disclination lines are absent with those the lines are present (*i.e.* in the smectic area): no differences have been evidenced. The spectra, reported in Fig. V.26, show that when the incident light is polarized parallel to the smectic easy axis (red line in figure), no plasmonic band are visible, while if the incident light is polarized perpendicular (black line), the longitudinal plasmonic band is detected. This evidence can be accounted for assuming that NRs preferentially orient their long axis perpendicular to the smectic easy axis.

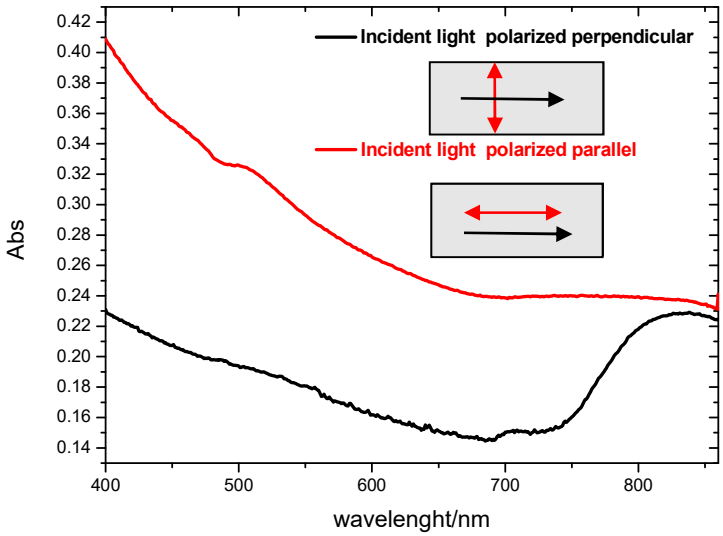

Fig. V.27. The incident light is polarized parallel to the disclination lines (red line) the incident light is polarized perpendicular to the disclination lines (black line)

In conclusion, we observed spectral response of AuNR@L_1 embedded in 8CB liquid crystal smectic phase and in disclination line patterning. No difference have been detected between two areas. This accounts for a homogenous assembling into two environments organized according the spatial LC organization, responsible of the coupling of the plasmonic band. The longitudinal plasmonic band of the spectrum obtained from cell is red-shifted and broadened suggesting that LC environment organized into the cell acts as an orienting medium for AuNR@L_1.

Moreover, irradiating the 8CB-AuNR@L_1 by polarized light, it was observed a difference in the longitudinal band intensity according to the polarization angle; in particular, this band disappears when the incident light has a polarization direction parallel to the smectic easy axis. Taking into account that we found a limited diffusion of the mixture (8CB- AuNR@L_1) into the cell, due to the not very high affinity between AuNR@L_1 and 8CB, we assume that nanorods arrange perpendicular to the smectic easy area in order to minimize the contact between L_1 coating and 8CB.

REFERENCES:

1. a) S. R. J. Oliver, N. Bowden and G. M. Whitesides, *J. Colloid Interface Sci*., **2000**, 224, 425; b)
   Z. L. Wang, *Adv. Mater*., **1998**, 10, 13
2. a) M. Brust, D. Bethell, D. J. Schiffrin and C. J. Kiely, *Adv. Mater*.,**1995**, 7, 795; b) R. P. Andres, *Science*, 1996, 273, 1690
3. a) M. Bagiński, A. Szmurło, A. Andruszkiewicz, M. Wójcik, W. Lewandowski , **2016**: Dynamic self-assembly of nanoparticles using thermotropic liquid crystals, *Liquid Crystals*; b) T. Hegmann, H. Qi, V. M. Marx, *JIOPM*, 17, **2007**, 483
4. K. J. M. Bishop, C.E. Wilmer, S. Soh, B. A. Grzybowski, *Small*, **2009**, 5, 1600
5. N. R. Jana, L. A. Gearheart, S. O. Obare, C. J. Johnson,K. J. Edler, S. Mann, C. J. Murphy, *J. Mater. Chem*., **2002**, 12, 2909
6. a) H. Nakashima, K. Furukawa, Y. Kashimura, K. Torimitsu, *Langmuir*, **2008**, 24, 5654; b) G. González-Rubio, J. González-Izquierdo, L. Bañares, G. Tardajos, A. Rivera, T. Altantzis, S. Bals, O. Peña Rodríguez, A. Guerrero-Martínez, L. M. Liz-Marzán, *Nano Lett*. **2015**, 15, 8282
7. H. Chen, L. Shao, Q. Lia, J. Wang, *Chem. Soc. Rev*., **2013**,42, 2679
8. Y. Xie, Yu. Liang, D. Chen, X. Wu, L. Daic, Qian Liu, *Nanoscale*, **2014**,6, 3064
9. S. Vial, I. Pastoriza-Santos, J. Pèrez-Juste, L. M. Liz-Marzán, *Langmuir*,**2007**, 3, 4606
10. a) W. Ni, R. A. Mosquera, J. Perez-Juste, L. M. Liz-Marzán, *J. Phys. Chem. Lett*., **2010**, 1, 1181 ; b) K. G. Thomas, S. Barazzouk, B. I. Ipe, S. T. S. Joseph, P. V. Kamat, *J. Phys. Chem. B,* **2004**, 108, 13066
11. R. Ahijado-Guzmán, G. González-Rubio, J. G. Izquierdo, L.Bañares, I.López-Montero, A. Calzado-Martín, M. Calleja,G. Tardajos, A. Guerrero-Martínez, *ACS Omega,* **2016**, 1, 388
12. D. Coursault, J. Grand, B. Zappone, H. Ayeb, G. Lévi, N. Félidj, E. Lacaze, *Adv. Mater.,* **2012**, 24, 1461
13. G. L. Nealon, R. Greget, C. Dominguez, Z. T. Nagy, D. Guillon, J. Gallani, B. Donnio, *J. Org. Chem.*, **2012**, 8, 349
14. H. Qi, T. Hegmann, *Liquid Crystals Today*, **2011**, 20, 102
15. Y. A. Garbovskiy, A. Glushchenko, *Solid State Physics*, VOL. 62
16. The nematic liquid crystal phase is characterized by molecules that have no positional order but tend to point in the same direction (along the director).The smectic liquid crystal phase is characterized by molecules that have positionally ordered along one direction.

17. D. Lysenko, P. Pagliusi, C. Provenzano, Y. Reznikov, K. Slyusarenko, G. Cipparrone, *Appl. Phys. Lett*., **2013**, 103, 151913
18. J. Perez-Juste , I. Pastoriza-Santos a, L. M. Liz-Marzán,P. Mulvaney, *Coord. Chem. Rev*., **2005**, 249, 1870
19. B. Rožič, J.Fresnais, C. Molinaro, J. Calixte, S. Umadevi, S. Lau-Truong, N. Felidj, T.Kraus, F. Charra, V. Dupuis, T. Hegmann, C. Fiorini-Debuisschert, B. Gallas, E. Lacaze, *ACS Nano*, **2017**, 11, 6728

CONCLUSIONS AND PERSPECTIVES

Conclusions and perspectives

Synthesis and characterization of gold nanoparticles

The research work concerns with **the synthesis and characterization of gold nanoparticles**. The main goal of the thesis is to emphasize the *correlation* between size, shape and environment of nanoparticles and their plasmonic properties. As the **shape** or **size** of the nanoparticle changes, the surface geometry changes causing a shift in the electric field density on the surface. This causes a modification of the oscillation frequency of the electrons, generating different cross-sections for the optical properties including absorption and scattering. The refractive index of the surrounding medium (capping agent and solvent), as well as the average distance between neighbouring metal nanoparticles, has been shown to influence the spectral features.

As we have schematized below (scheme A), the followed synthetic mechanism of nanoparticles' synthesis is based on the reduction of $Au^{(III)}$ to $Au^{(0)}$. Small metallic nanospheres, originated by fast reduction of $Au^{(III)}$, act as seeds, that, by successive addition of $Au^{(0)}$, grow to form larger nanoparticles. The gold nanoparticles' surface is covered by a capping agent to prevent the coalescence.

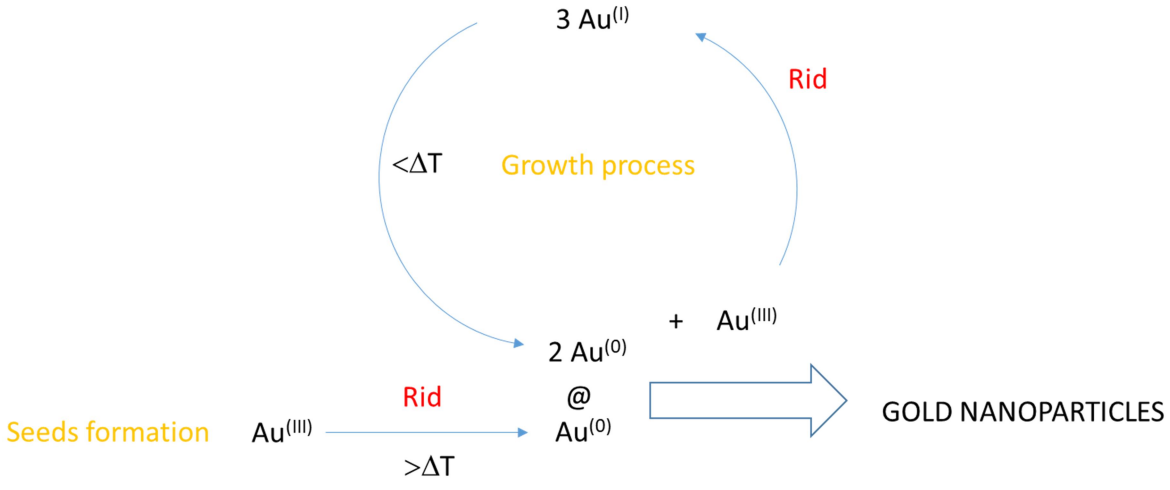

Scheme A. General synthetic mechanism of nanoparticles' synthesis

We started our investigation from the simplest shape, *i.e.* the *spherical shape;* successively, we explored anisotropic shapes, in particular *nanotriangles* and *nanorods*. All synthesis are performed in water solution.

The final shape of the nanoparticles is strongly dependent on the **size** of the seeds that changes according to the **capping agent**. In particular, we observed that seeds with size around 7 nm and capped with the negative charged sodium citrate, are the best choice if the spherical final shape is the challenge. Gold nanotriangles have been obtained from 7 nm-diameter seeds coated by CTAC. Instead, seeds with size around 3 nm and positive charged surface, coming from CTAB, are the best choice to synthesize nanorods with high yield.

Gold Nanospheres

On this basis, we synthesized gold nanospheres with different size by using NaCit as reducing and covering agent. The advantage of this synthetic protocol is the speed preparation of the stock solutions, because only two reagents are used: the metal salt, source of $Au^{(III)}$, and NaCit. The disadvantage is that involves a considerable amount of time, because the synthesis is under temperature's control. In order to reduce the reaction time we used a microwave as the heat source achieving high quality nanoparticles in a shorter time.

The first step is the seeds formation in which NaCit, under boiling temperature, *reduces* $Au^{(III)}$ to $Au^{(0)}$ and *covers* the seeds (to prevent the coalescence). In the growth process, the reduction of $Au^{(III)}$ to $Au^{(0)}$ from NaCit is performed by cooling temperature until 90°C to allow the inhibition of a new nucleation and favouring the consequent overgrown of the pre-synthesized seeds.

We resumed all the process in the scheme B.

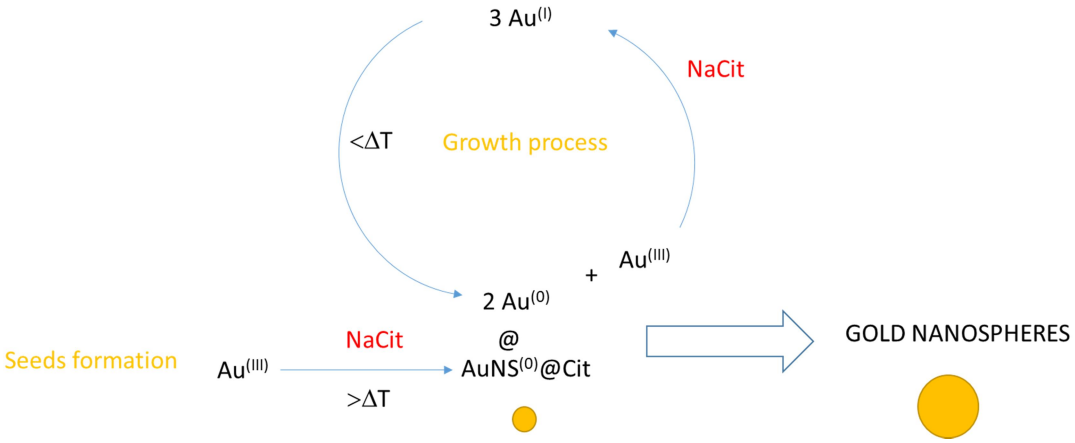

Scheme B. Mechanism of $AuNS^{(0)}$@Cit synthesis performed in water solution

Anisotropic shape

To prepare nanoparticles with anisotropic shape, it is necessary to use additional reagents, acting as "template-mediated shape" like CTAB or "shape directors", like Ag^+ . Specifically, the synthetic mechanism, known as ***seed-mediated growth approach***, proceeds through a physical separation of the nucleation process (seeds formation solution) from the growth process (growth solution), with a more effective control on the final shape. Following the *seed-mediated growth approach,* we synthesized gold nanorods covered with CTAB, AuNR@CTAB, dispersed in water. Both solutions includes a reductant, $HAuCl_4$ as gold source and CTAB. In presence of CTAB, $AuCl_4^-$ suffers a metathesis reaction, giving $AuBr_4^-$, passing from yellow to orange.

In the first step (*seeds solution*), the strong reducing agent, $NaBH_4$ reduces $Au^{(III)}$ to $Au^{(0)}$ in presence of CTAB that covers the spherical seeds to prevent the coalescence. High-quality seed solution is necessary to obtain high-quality nanorods. Ideally, the seeds should be monodisperse and display the same crystallographic habit, which in practice is achieved by adding the strong reducing agent in excess as fast as possible and under vigorous stirring.

Many actors play in the second step (*growth solution*) and we tried to understand in depth their role. According to the literature, it's clear that all of them play a crucial role in the growth processes of anisotropic gold nanoparticles, but it is not yet clear which molecule/nanoparticle interactions are primarily responsible for shape control. In the preparation of growth solution, we use ***CTAB at the critical concentration in which it forms rodlike micelles***, which act as compartments of nanometers size able to confine the nanocrystals growth and control and limit physically their enlargement. We add to the growth solution a salicylic acid derivative, *i.e.* 5-BrSA, to stabilize the CTAB micelles. We rationalized the mechanism underlying the process, taking into account that 5-BrSA acts as a weak reducing agent, reducing $Au^{(III)}$ to $Au^{(I)}$ (as showed by the bleaching of the starting $AuBr_4^-$ orange solution), and as complexing agent, forming a gold(I) complex. This complex intercalates into the CTAB bilayer, stabilizing the structure and localizing Au(I) into the rod-like nanoreactor. As discussed in the previous chapters, to obtaining rod-shaped nanoparticles is necessary to add $AgNO_3$ water solution. Also in this case, 5-BrSA is plausible to complex Ag^+ and, likewise to Au(I) ion, contribute to accumulate silver ion into the CTAB micelles.

At this stage, seed solution is added to the growth solution just after ascorbic acid addition; the little spherical seeds, coated by CTAB, diffuse into the rod-like micelles. Silver ions form a monolayer on the seed surface, preferentially on the anisotropic faces that are eventually present. Au(I) ion, also deposited onto seed surface, suffer the following **disproportion reaction**:

$$3Au^{+} \rightarrow 2\,Au^{(0)} + Au^{3+}$$

The $Au^{(III)}$, resulting from the previous reaction, is reduced by ascorbic acid reduces to $Au^{(I)}$, and, in this way, the seeds growth; the presence of silver ion drives the formation of elongated shape. The growth starts on the faces where $Ag^{(I)}$ is absent; successively, $Ag^{(I)}$ is dislodged, and the gold growth proceeds anisotropically.

The scheme C recapitulates the steps of the synthesis.

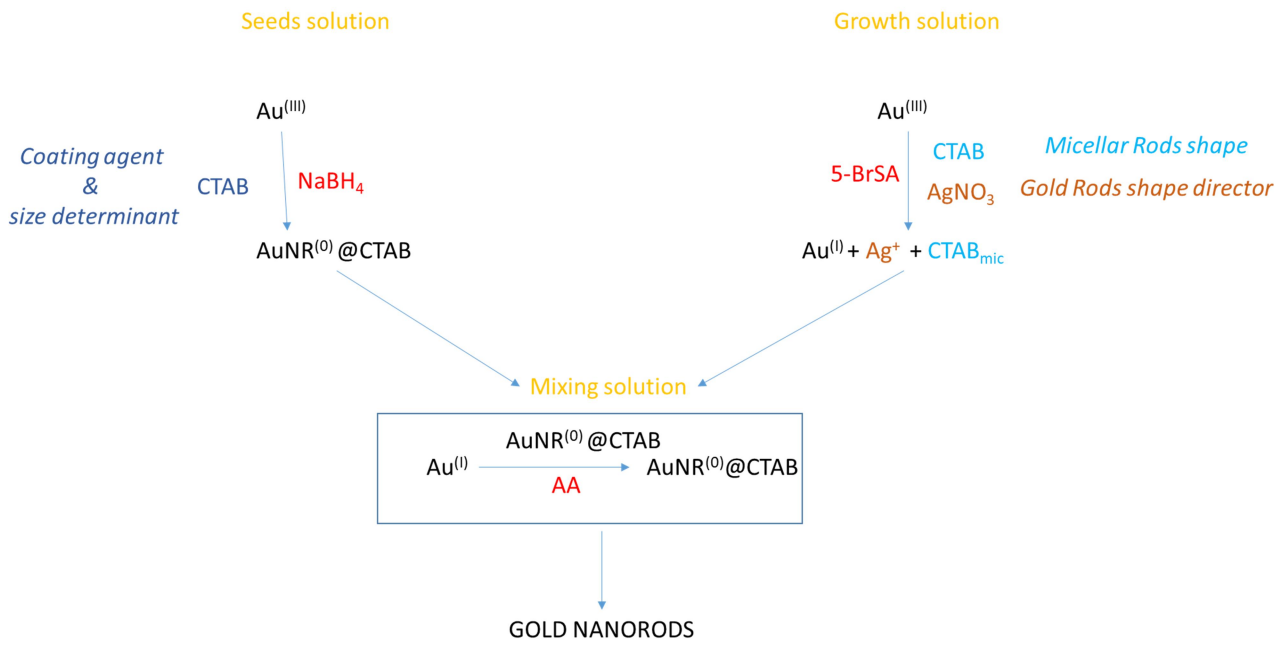

Scheme C. Mechanism of $AuNR^{(0)}$@CTAB synthesis performed in water solution

We analyzed accurately the contribution of CTAB and $AgNO_3$ in the formation of the shape like rod. In particular, reducing the CTAB concentration, nanorods with a high polydispersity are formed. Regards to the $AgNO_3$ role, we evidenced that by reducing its amount, elongated shape of nanoparticles are formed, similar to bipyramids, while, if $AgNO_3$ is absent, very different shape are observed.

The **seed-mediated growth method** is a tuneable synthetic strategy for metal nanoparticles: in fact, less changes of the protocol translate into important differences in the morphology of the nanoparticles. To this end, small variations introduced in the $AuNR^{(0)}$@CTAB synthetic protocol, allow to obtain gold nanotriangles $AuNR^{(0)}$@CTAC. First of all, CTAB is replaced by CTAC, because, as previous illustrated, CTAC allow bigger spherical micelles. In summary, we prepared **two growth solutions**, one (A) used to grow the CTAC-capped seeds into larger nanospheres, while the second (B) is used as NTs growth batch. A picture of the process includes seeds formation (from $AuCl_4^-$ reduction by $NaBH_4$) capped by CTAC, that growth after A solution is added, by the already illustrated disproportion reaction. At this stage, B solution is added; this solution differs from A by the presences of NaI, which role is clearly to direct the formation of nanoparticles triangular-like-shaped, as demonstrated by the fact that its absence carry out to spherical nanoparticles, however, an accurate description of the mechanism is currently unknown. No protocol allows to obtain nanotriangles with an unitary yield, so it is always necessary to purify the final solution to separate triangles from the other shapes: this is obtained by addition of a 25 wt % CTAC solution, that causes the precipitation of the more heavy nanotriangles, while in the surnatant remain other shapes (spheres, cubes).

We resumed all the process in the scheme D.

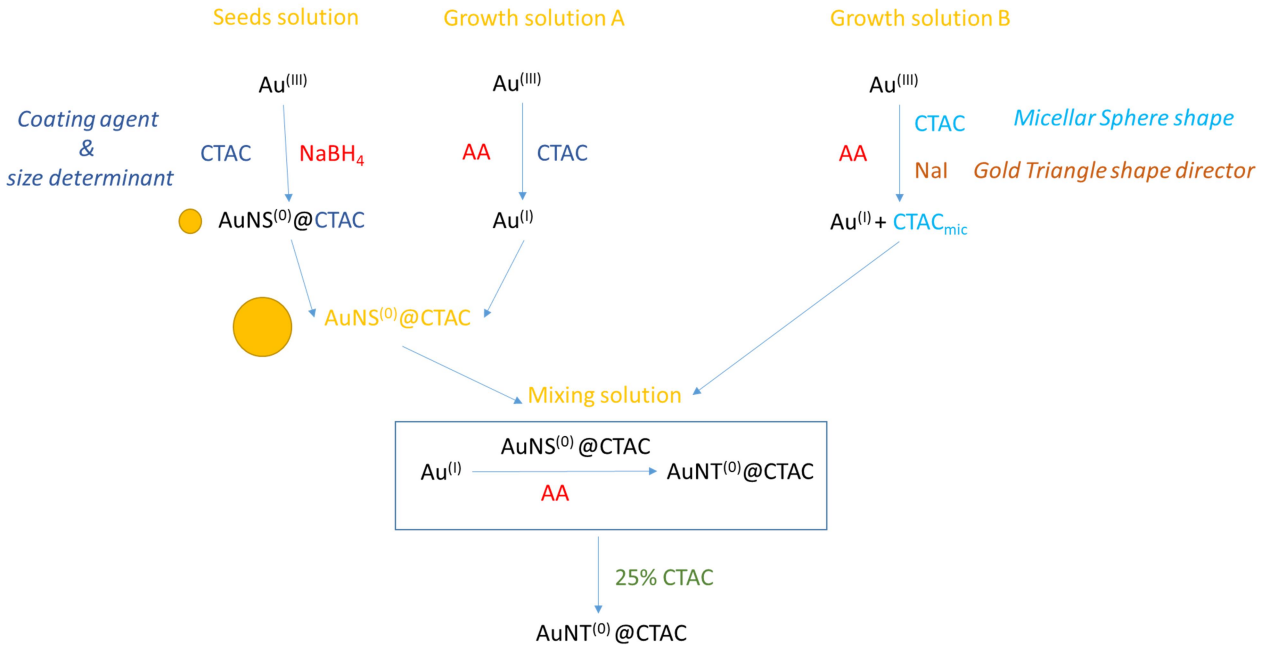

Scheme D. Mechanism of AuNT$^{(0)}$@CTAC synthesis performed in water solution

Size control

Besides shape control, size control of the nanoparticles can be obtained by various synthetic strategies. For exemplum, the increase of the **spherical** AuNS$^{(0)}$@Cit diameter is obtained by repeating the addition of NaCit and Au$^{(III)}$ to the preformed nanospheres (see Scheme B). We synthesized **nanorods** with different aspect ratio by using two strategies: in the first, the size is determined by the amount of the Au$^{(III)}$ in the growth solution (see Fig. 1), while, in the second one, a variable amount of sees solution is added when Au$^{(III)}$ is disappeared (Fig. 2). In the case of **nanotriangles**, literature reports that different amount of seeds implies different size.

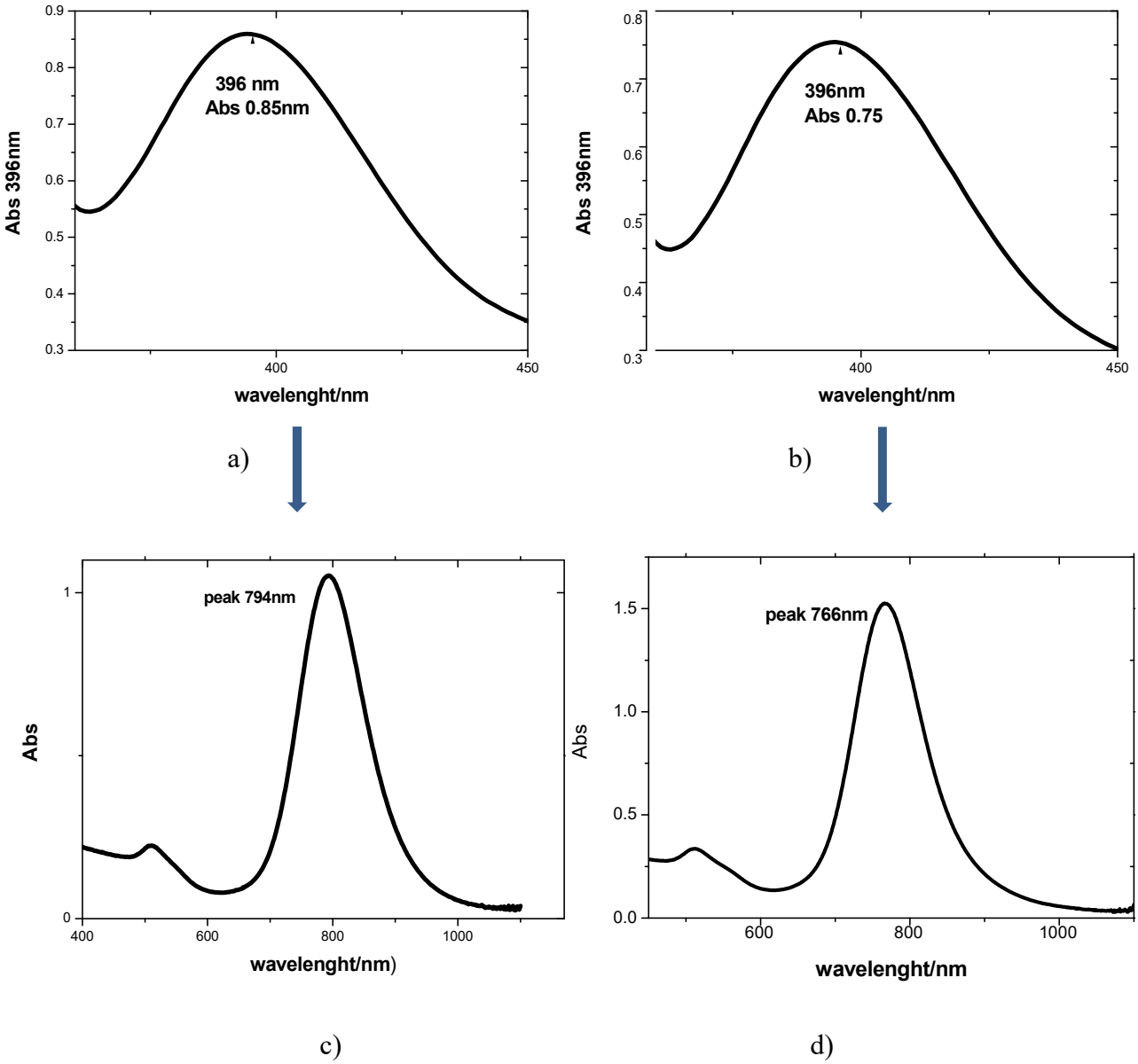

Fig.1. (c) (d) Extinction spectra of gold nanorods with different aspect ratio correlated with the amount of $Au^{(III)}$ present in the growth solution (a), (b)

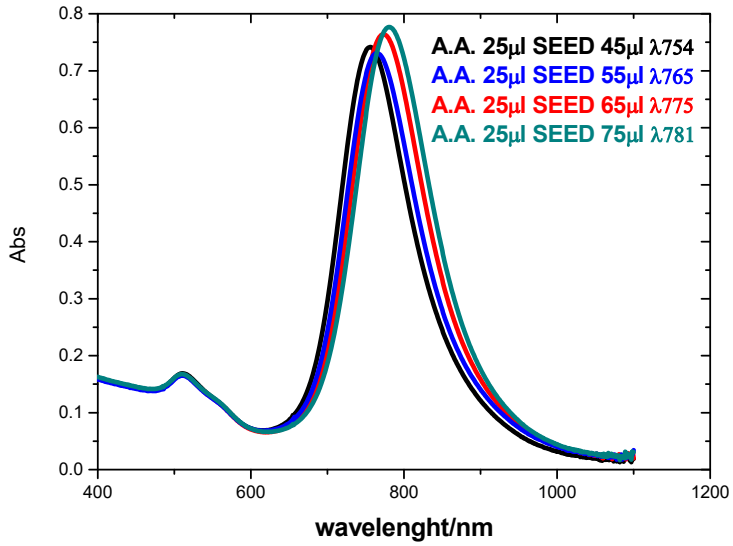

Fig.2. Extinction spectra of gold nanorods with different aspect ratio obtained by varying the seed solution amount in a narrower range.

Surface chemistry

To obtain nanoparticles soluble in various solvent, we modified surface chemistry by varying the coating agent. For example, citrate-capped gold nanospheres have been coated with PVP simply by adding PVP to AuNS@Cit water solution. In the case of AuNR@CTAB we have been changed original coating with PEG-SH, liquid crystal, PEG-SH-DDT, and, finally, silica coating, taking advantage of a wide solubility and of different chemical interplay.

Optical properties

Metal nanoparticles with various shapes, sizes and organization show unique scattering spectra depending on their geometries. Spectroscopy is a precious technique able to identify, characterize and study nanoparticles features. On this basis, we tuned the optical properties of nanoparticles modifying not only their shape, but size, covering agent, medium and arrangement.

As illustrated in figure 3, different shapes correspond to precise extinction spectra: in particular, surface plasmonic resonance of **spherical gold nanoparticles** is characterized by a single band in the visible region around 515 nm. Growing the diameter of the nanospheres, the plasmonic peak red-shifts: this because surface electrons are held on the nanoparticle surface by a force than decrease if the nanoparticle size increases.

Anisotropic nanoparticles show more than one plasmonic peak in the visible and near infrared region of the electromagnetic spectrum, associated with the various orientations of the particle axes relative to the electric field of light. By using an unpolarised light source to irradiate unoriented AuNR solution, both peaks are detected; instead, polarized light impinging oriented AuNRs can excited a single resonance mode. In particular, transverse oscillation is peaked at around 515 nm; differently from this band, the longitudinal resonance produce a band which position is more sensible to the aspect ratio and other factors, falling in a more wide range from 700 to 850 nm.

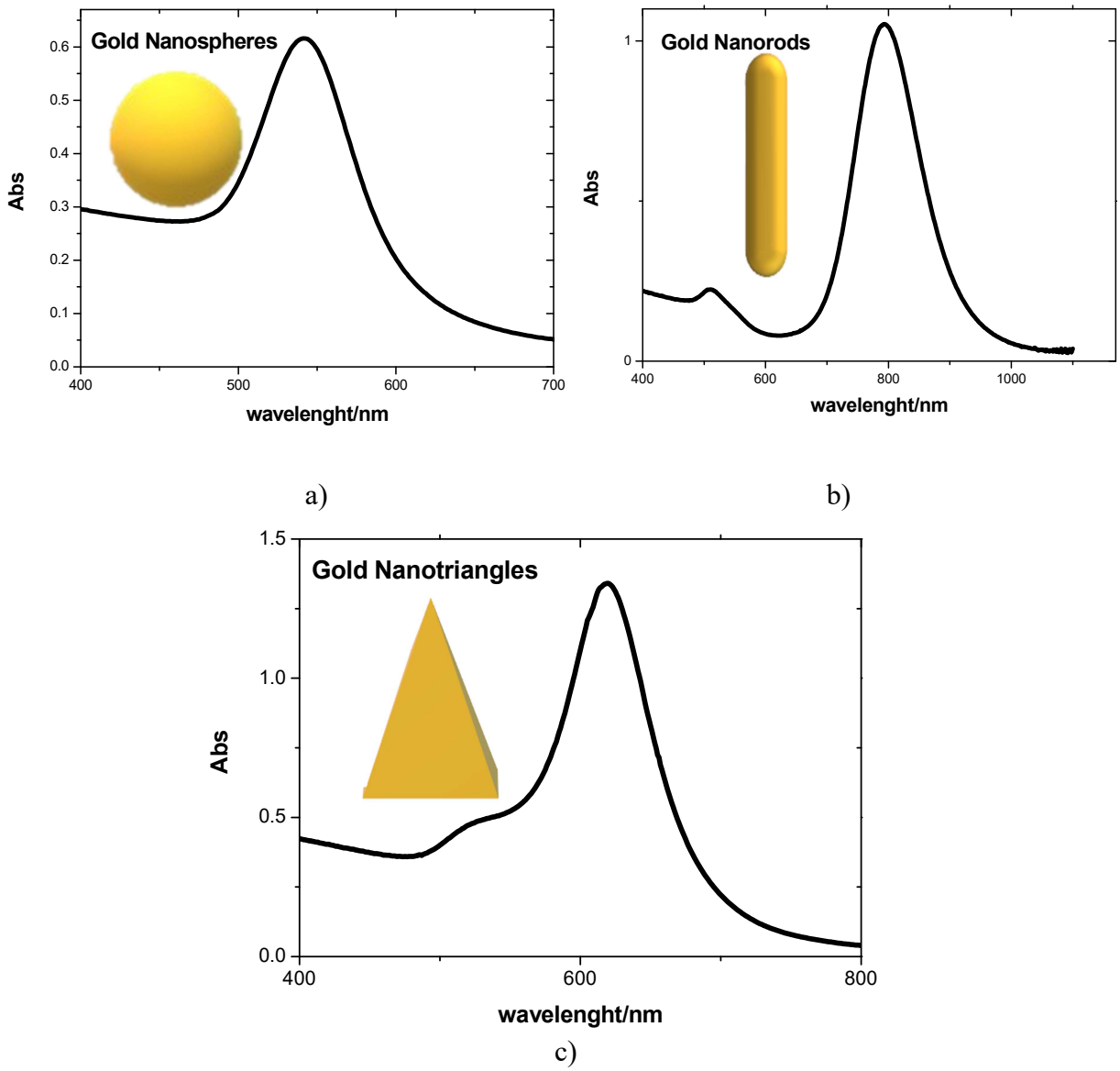

Fig.3. Extinction spectra of gold nanospheres (a); gold nanorods (b); gold nanotriangles (c)

Position of the plasmon band is due to the difference of the **refractive index** at the interface metal/dielectric, where the dielectric medium can be the solvent and/or the

coater. We have explored different coating agents in different solvents: invariably, for capping agents able to give only thinner coating (*e.g.* PEG-SH, liquid crystal, PEG-SH-DDT), the band position depend on the refractive index of the solvent, while, in the case of the silica shell, tuning of the thickness determines the plasmonic band position. In this regard, we were able to tune the silica thickness by modulating the ratio between NRs to TEOS concentration, obtaining AuNR@SiO_2 with thickness varying from 3.5 to 30 nm. Tuning the thickness of the silica coating, it's a way to change the optical properties of gold nanorods as showed in Fig.4.

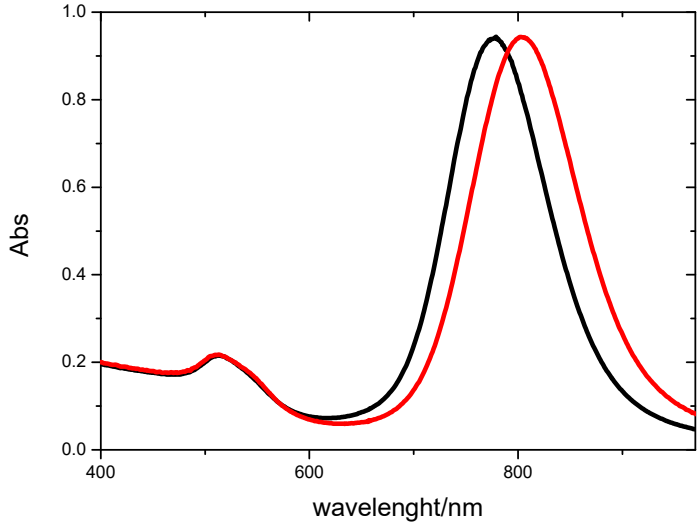

Fig.4. Extinction spectra of AuNR@SiO_2 with different thickness: 24 nm x 16 nm long axis x short axis (red line); 5 nm x 3.5 nm long axis x short axis (black line)

Silica: an excellent host material

Silica is a fascinating material for its versatility and modularity and an excellent host material; in fact, many molecules like **fluorophores** can be embedded into the shell. On this basis we prepared AuNR@(**Ir_1**)SiO_2 by encapsulating into the silica shell an Ir(III) luminescent complex, **Ir_1**, to study the interactions between its excited electronic states and the plasmonic modes of gold nanorods. We found that the green luminescence of Ir(III) is quenched by an energy transfer process towards the transversal plasmonic band of AuNRs positioned at 514 nm. To study this process, we compared the photophysical properties of AuNR@(**Ir_1**)SiO_2 with a sample constituted by mixing a AuNR@SiO_2 solution with **Ir_1**; only in the first system we observed a dramatic energy transfer from complex to gold plasmon. Furthermore, a particular spectral feature, *i.e.* a blue band, on which was measured a

very short excited state decay, led us to suppose a metal enhanced fluorescence (MEF) effect, attributed to the fraction of **Ir_1** directly in contact with the metal surface. To better confirm this hypothesis, we prepared AuNR@SiO_2(**Ir_1**)SiO_2 that differs from AuNR@(**Ir_1**)SiO_2 because fluorophore was added after the first TEOS addition: in this way **Ir_1** was placed onto the first layer of silica shell, so avoiding the direct contact with metal surface. Photophysical analyses show the absence of the features attributed to MEF. In addition, in AuNR@(**Ir_1**)SiO_2 was evidenced a more structured photophysics, that suggest to identify a tip and a side zone around nanorods, where the intensity of the plasmonic field is different; consequently, because the MEF depend on the plasmon field intensity, the two zones showed a different intensity of the phenomenon.

Spatial arrangement of Gold Nanorods

Currently, the most ambitious strategy to modulate the plasmonic properties of anisotropic nanoparticles is to operate on their **spatial arrangement** inducing a directional and/or positional order. Organized superstructures of AuNRs show an optical appearance different from the isolated NRs; this is attributed to the plasmon coupling, *i.e.* the interaction between the plasmons.

To spatially organize anisotropic gold nanoparticles should be, in principle, followed two strategies: one based on the interparticle forces due to a proper functionalization of the AuNPs (*direct assembly*), the other based on the presence of an orienting medium (*indirect assembly*).

Gold nanorods, for their anisotropic shape, can be assembled along two orientations: end-to-end or side-by-side; on this prospective, we synthesized **nanorods functionalised** preferentially on the tips or on the side, or, indifferently, on the total surface. Following a pH-controlled strategy we synthesized AuNRs covered by PEG-SH and lipoic acid at their sides and tips, respectively. The presence of lipoic acid at the tips dramatically changes the organization of the AuNRs at a pH = 5, corresponding to the pKa of the lipoic acid: hydrogen bonding between protonated and unprotonated lipoic acid is, in fact, responsible for nanorod end-to-end assembly in aqueous solution (Fig. 5). Without pH control, nanoparticles are assembled, but not in a preferential array.

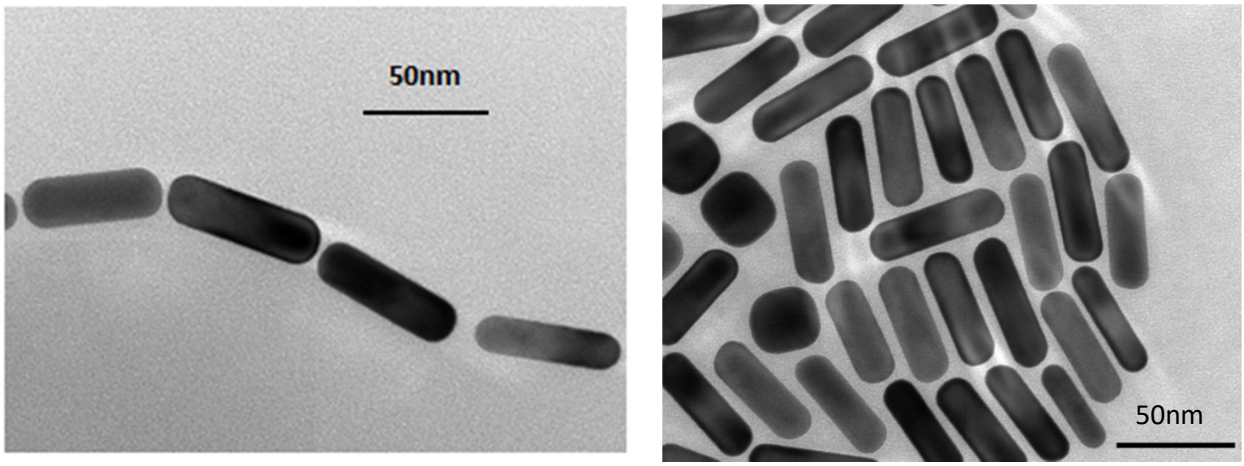

Fig.5. TEM image of nanorod end-to-end assembled with pH control; (b) nanorods no preferentially assemble without pH control.

Liquid crystals can act as **orienting medium** to organize AuNRs. Supramolecular mesogen organization appears to be undersized to give a positional order to a comparatively bigger NRs, while it seems suitable to organize them orientationally. Instead, proper-sized features could be the liquid crystal defects, where it should be possible to locate and to impart a positional and orientational order to AuNRs.

Plasmon coupling

The **plasmon coupling** has been found to be strongly dependent on the nanoparticles orientation. In particular, we present, as example, extinction spectra of three samples of AuNRs covered by PEG-SH and lipoic acid at their sides and tips, respectively. The first sample is constituted by unorganized nanorods (Fig. X1); the second by assembled (but unorganized!) NRs (Fig. X2) and the last sample is constituted by organized NRs according to the intermolecular forces, *i.e.* end-to-end arrangement (Fig.3).

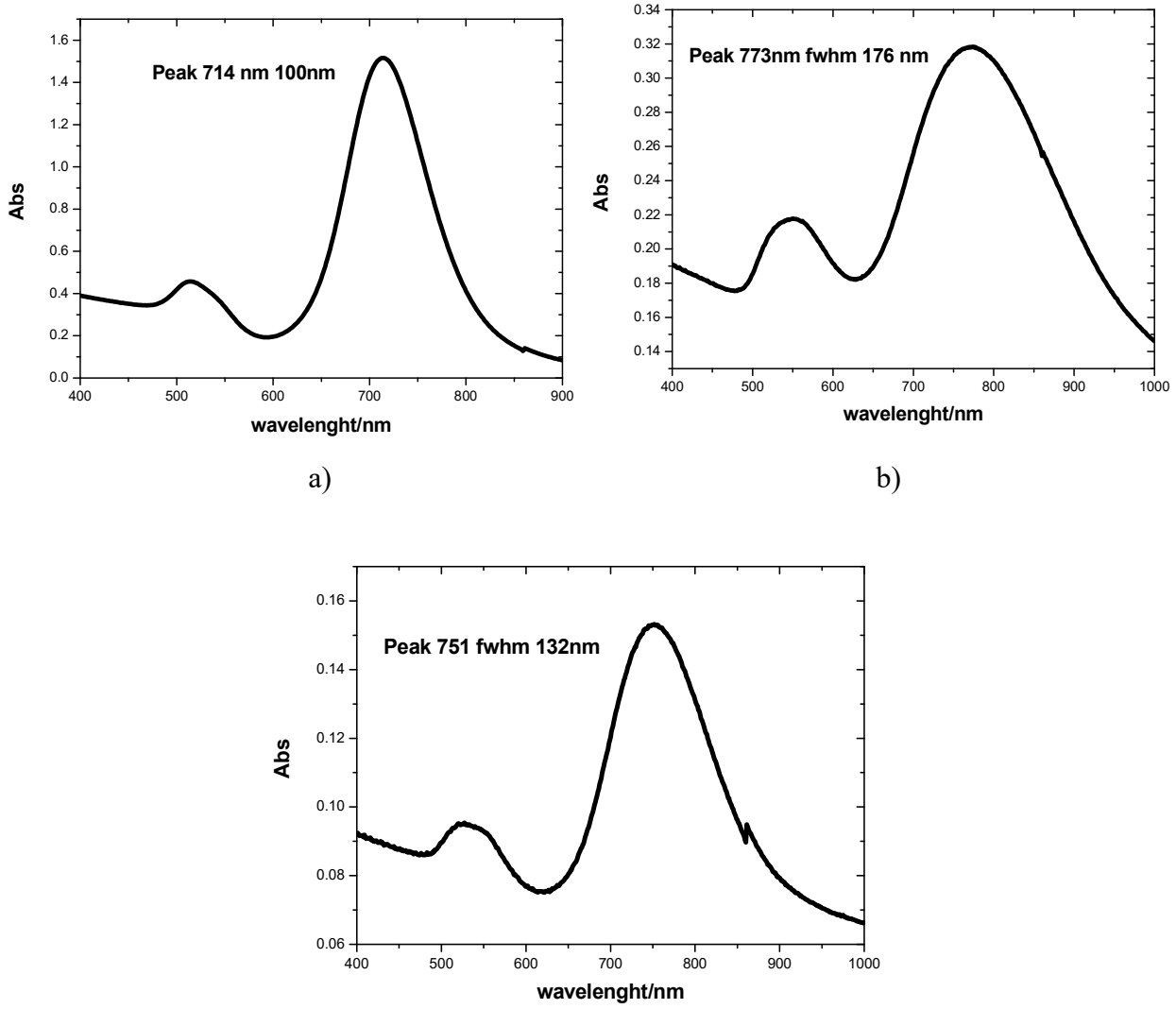

Fig.6. extinction spectra: a) unorganized AuNRs; b) assembled AuNRs; c) end-to-end organized AuNRs

As shown in the figures, in the extinction spectra of assembled AuNRs (Fig.6 (b)), the longitudinal plasmonic band is red-shifted and broadened respect to the unorganized AuNRs (Fig.6 (a)); moreover, spectra of the end-to-end organized NRs sample (Fig.6. (c)) shows a reduced broadening of the this sample compared to that of the assembled NRs, and a less red-shift. Taking into account that the broadening of the longitudinal band is generally attributed to the presence of polydispersion of the active objects, the reduced broadening suggests an better monodispersion of the organized NRs, respect to the other sample, that means that nanorods are driven towards a preferential spatial organization. The reduced red-shift could be attributed

to a reduced numbers of interacting NRs; for this reason the energy requested to induce the collective oscillation of the surface electrons result increased.

Plasmon coupling and inter-particle spacing

The plasmon coupling has been found to be strongly dependent also on the inter-particle spacing. This can be achieved by tuning the **coating thickness**. The coverage, in fact, can modulate the plasmon field in different ways: it can drive the nanoparticles' assembling in a precise structural order, or avoid the plasmon interaction, increasing the distance between nanoparticles. On this perspective, by tuning the silica thickness, we estimated the distance between nanoparticles necessary for the plasmon interaction. By measuring the edge-to-edge distance between the gold core of the examined samples (Fig.7), in fact, we found that it shortens by decreasing the silica thickness, so allowing a better coupling. The coupling of the plasmonic fields is effective when the distance between nanoparticles it is not higher than 10 nm (Fig.7(b)). When the distance is greater, no nanorod interacts each other (Fig.7 (a)).

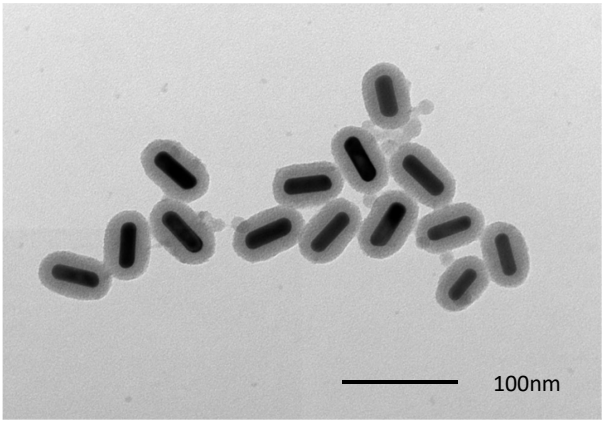

a)

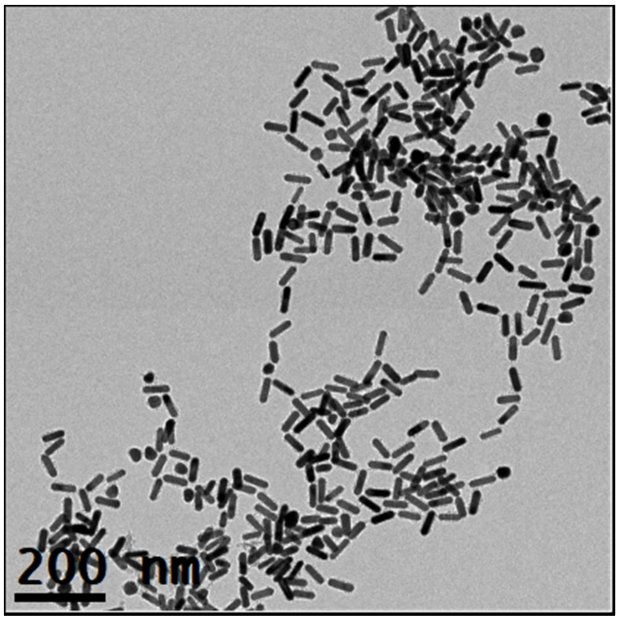

b)

Fig.7. TEM image of AuNR@Si with interparticle distance higher than 10 nm (a); TEM image of AuNR@Si with interparticle distance less than 10 nm (b)

Spectroscopically, it is evident by the difference in the spectral feature between the two samples (a) and (b): in the sample (b) the spectrum of the solution and the spectrum of the film (Fig. 8 (b)) are different; in particular, the longitudinal plasmonic bands of the film spectrum is red-shifted and broadened compared to that of the spectrum in solution. This behaviour is attributed to the coupling of the plasmonic fields, allowed by the shortened distance among gold cores. Differently, Fig.8 (a), corresponding to sample (a), shows the superimposition between the spectrum in solution and the spectrum of the film accounts for the absence of coupling because the interparticle distance is higher than 10 nm.

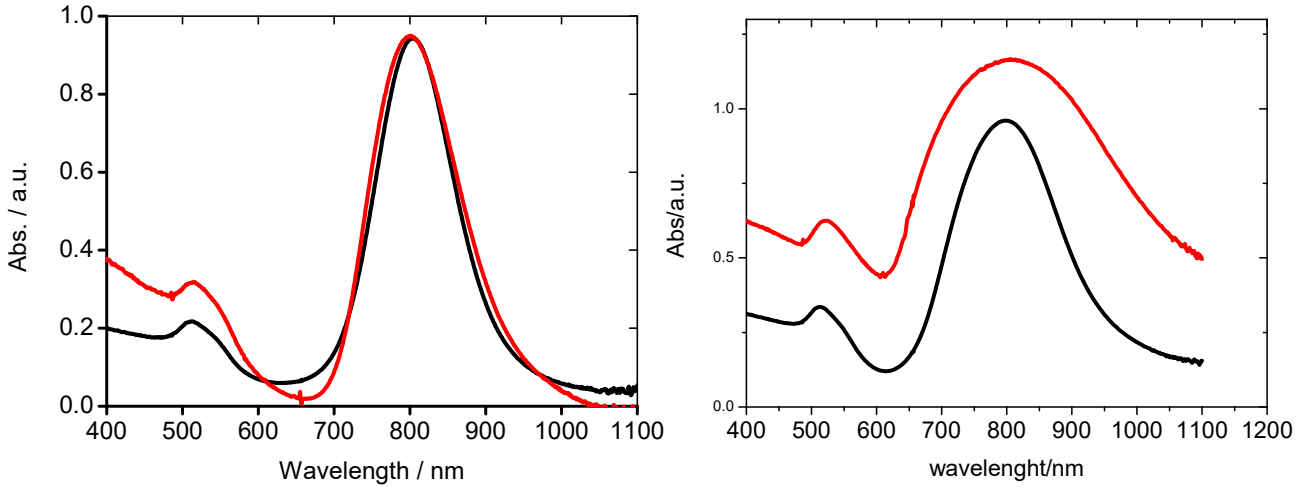

a) b)

Fig.8. (a) Extinction spectrum of AuNR@SiO_2 from ethanol solution (black line), and from film sample (red line): (b) extinction spectrum of AuNR@SiO_2 from ethanol solution (black line), and from film sample (red line)

Final remarks

In conclusion, we deeply discussed the mechanisms underlining the synthetic protocols of gold nanoparticles, in particular modulating their shape and size. We synthesized gold spheres, rods and triangles, exploring different coating, and studying the thickness effect. We performed accurate photophysical studies of the plasmonic properties of these metal nanoparticles, correlating them to the size, shape and environment.

Moreover, we have started to study the assembly of this nano-objects, driven that by direct or indirect mechanism, and finally we have explored the spectroscopical effect of the plasmon coupling.

We are awareness that anisotropic gold nanoparticles can be useful in various fields, from metamaterials to several biotechnology applications, such as sensory probes, drug delivery, and therapy techniques. Because gold nanoparticles can be excited by light at Near-IR absorbing, it is reasonable to think that they can be used as contrast agents for diagnostic and phototherapeutic applications, such as two-photon luminescence imaging, light-scattering imaging, surface-enhanced Raman scattering, and photothermal therapy. Scientists expert in plasmonic and organic photovoltaic field are working together to improve the absorption of sunlight and the photon–electron coupling to boost the performance of the devices. Recent advances in the field of plasmonics for organic solar cells focus on the incorporation of gold nanoparticles. Furthermore, as we have abundantly emphasized, by changing the particle shape, size, surface chemistry, or spatial array , the optical and electronic properties of gold nanoparticles can be adjustable and applicable for different uses, which present a promising potential. Gold nanorods are preferred to the spheres because it is possible to tune their longitudinal plasmon band (from the visible to NIR region of the electromagnetic spectrum) according to aspect ratio, chemical surface, medium and arrangement. This makes gold nanorods interesting candidates for a lot of applications such as sensing of biological species via particle aggregation, darkfield imaging of nanorods in biological mediums in order to provide spatial or mechanical information, photothermal therapeutic treatment of pathogenic cells including bacteria, cancer, or potentially viruses as a result of irradiation induced local temperature increases.

Appendix

MATERIALS AND EXPERIMENTAL APPARATUS

A.1 Photophysical Measurements

Spectrofluorimetric grade solvents were used for the photophysical investigations in solution.

1) ***Absorption***

A Perkin Elmer Lambda 900 spectrophotometer was employed to obtain the absorption spectra.

2) ***Emission***

Steady-state emission spectra were recorded on a HORIBA Jobin-Yvon Fluorolog-3 FL3-211 spectrometer (Fig. 1) equipped with a 450 W xenon arc lamp (**L**), double-grating excitation ($\mathbf{M_{ex}}$) and single-grating emission ($\mathbf{M_{em}}$) monochromators (2.1 nm/mm dispersion; 1200 grooves/mm), and a Hamamatsu R928 photomultiplier tube (**PM**) or a TBX-04-D single-photon-counting detector ($\mathbf{D_{TCSPC}}$) or a InGaAs liquid nitrogen-cooled solid-state detector ($\mathbf{D_{InGaAs}}$). Emission and excitation spectra were corrected for source intensity (lamp and grating) and emission spectral response (detector and grating) by standard correction curves.

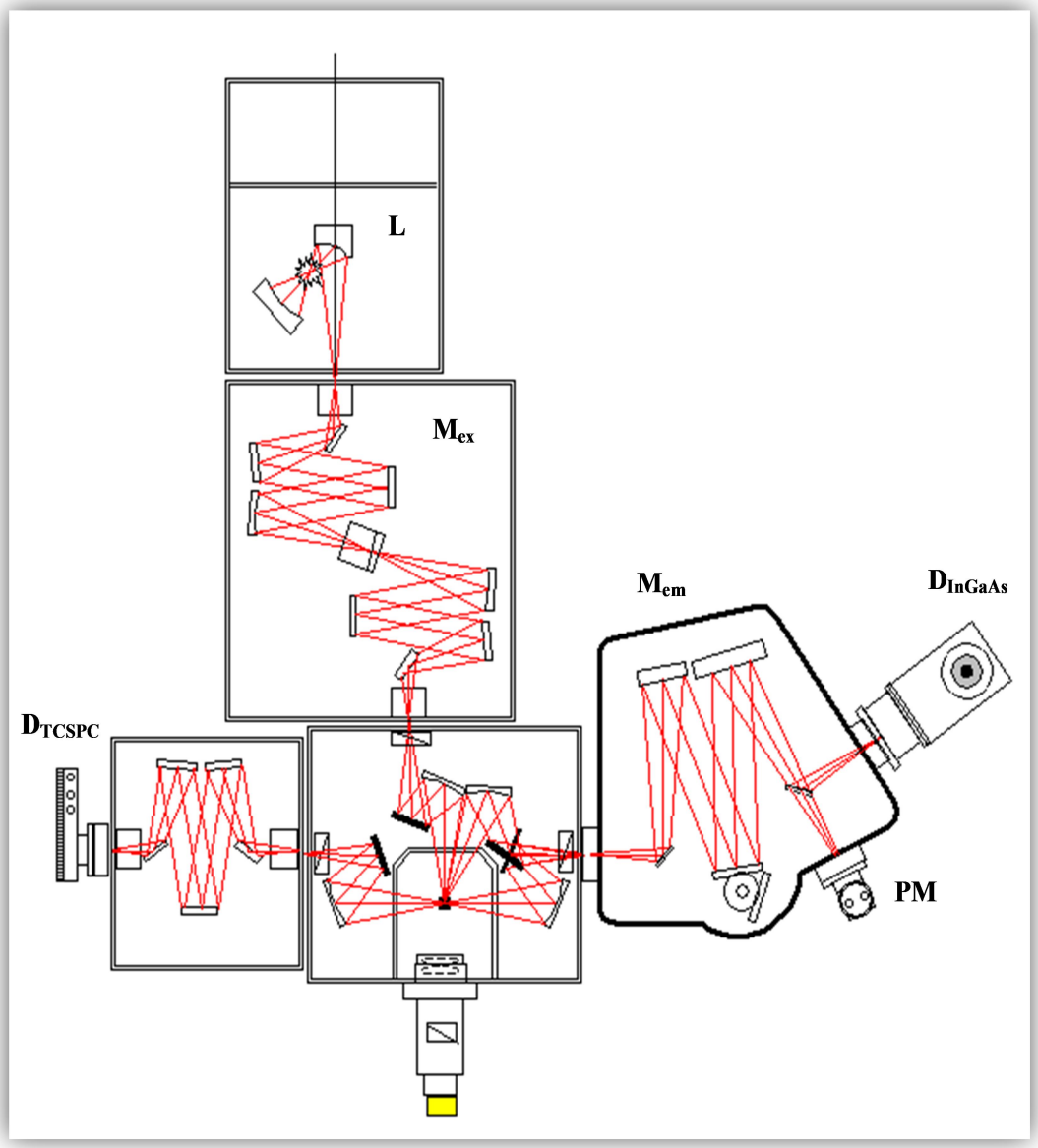

Figure 1. FluoroLog3-2iHR1-TCSPC-IGA, optical configuration.

3) ***Lifetimes***

Time-resolved measurements were performed using the time-correlated single-photon counting (TCSPC) option on the Fluorolog 3.

Excitation sources (Table 1) were mounted directly on the sample chamber at 90° to a single-grating emission monochromator and collected with a TBX-04-D single-photon-counting detector. The photons collected at the detector are correlated by a time-to-amplitude converter (TAC) to the excitation pulse.

Source	λ_{em}	Duration	Power	Repetition rate
Laser Nanoled	379 nm	750 ps	63 pJ	1 MHz

Table 1. Excitation source used.

Signals were collected using an IBH Data Station Hub photon counting module, and data analysis was performed using the commercially available DAS6 software (HORIBA Jobin Yvon IBH). The fitting procedure of the emission intensity decays I(t) uses a multi-exponential model according to the expression

$$I(t) = \Sigma_i \alpha_i \exp(-t/\tau_i)$$

where τ_i are the decay times and α_i represent the amplitudes of the components at t=0. Goodness of fit was assessed by minimizing the reduced Chi squared function (χ^2) and visual inspection of the weighted residuals. When using the multi-exponential decay law it is often valuable to determine the average lifetime ($< \tau >$), which is given by

$$< \tau > = \Sigma_i \alpha_i \tau_i^2 / \Sigma_i \alpha_i \tau_i$$

4) ***Emission quantum yields***

Emission quantum yields values (Φ) in solution were determined by using the optically dilute method (Demas 1971) on aerated and deaerated solutions, which absorbance at excitation wavelengths was < 0.1, according to the formula (where the superscript text R refers to the reference standard):

$$\Phi = \Phi^R (A_{em}/ A^R_{em}) (Abs/Abs^R) (n/n^R)$$

where A_{em} is the integrated corrected emission area obtained exciting the sample at the wavelength λ_{ex}, *Abs* is the absorbance measured at the λ_{ex}, *n* is the refractive index of the solvent. $Ru(bipy)_3Cl_2$ (bipy = 2,2'-bipyridine) in water (Φ = 0.028) (Nakamaru 1982) or aminopyridine in ethanol (Φ = 0.37) (Mutai 2002) were used as standard. The experimental uncertainty on the molar extinction coefficients is 10%, while on the emission quantum yields is 20%. The examined compounds are fairly stable in solution, as demonstrated by the constancy of their absorption spectra over a week.

A.2 Morphological Characterization

*1) **Transmission Electron Microscope***

The size and morphology of the gold nanoparticles were measured using a transmission electron microscope (Jeol JEM-1400 Plus 120 kV). The samples for transmission electron microscopy (TEM) were prepared by depositing a drop of a diluted solution on 300 mesh copper grids. After evaporation of the solvent in air at room temperature, the particles were observed at an operating voltage of 80 kV.

*2) **Dinamic light scattering***

A direct measurement of the size distribution of colloids was performed by using the Dinamic light scattering (DLS) technique on a Zetasizer Nano S system from Malvern Instruments (632.8 nm, 4 mW HeNe gas laser, avalanche photodiode detector, 175° detection). DLS measurements were performed in triplicate at 25 °C.

A.3 Chemicals

Hexadecyltrimethylammonium bromide (CTAB, ≥96%), 5-bromosalicylic acid (technical grade, 90%), hydrogen tetrachloroaurate trihydrate ($HAuCl_4 \cdot H_2O$, ≥99.9%), silver nitrate ($AgNO_3$, ≥99.0%), L-ascorbic acid (≥99%), sodium iodide 99.99%), trisodium citrate (99%), polyvinilpolypyrrolidone (PVP K15, Mn 10000) and sodium borohydride ($NaBH_4$, 99%) were purchased from Aldrich. All the chemicals were used as received. Milli-Q water (resistivity 18.2 MΩ·cm at 25 °C) was used in all experiments. All glassware was washed with aqua regia, rinsed with water, sonicated 3-fold for 3 min with Milli-Q water, and dried before use. TEOS (Alfa Aesar, 99.9%), NaOH (Sigma Aldrich, 98%), MeOH (Sigma Aldrich) were used for the SiO_2 overcoating. Ir(III) complex was synthesized according to the procedure previously reported.[§ IV.1]

A.4 Luminescence Intensity Decays

The time-resolved emission decays below refer to **Ir_1** in water contained in the sample AuNR@(**Ir_1**)@SiO_2TPSA (λ_{ex}= 379 nm, $\lambda_{monitored}$= λ_{em}= 465 nm (a) 490 nm (b) 540 nm (c) 565 nm (d)).

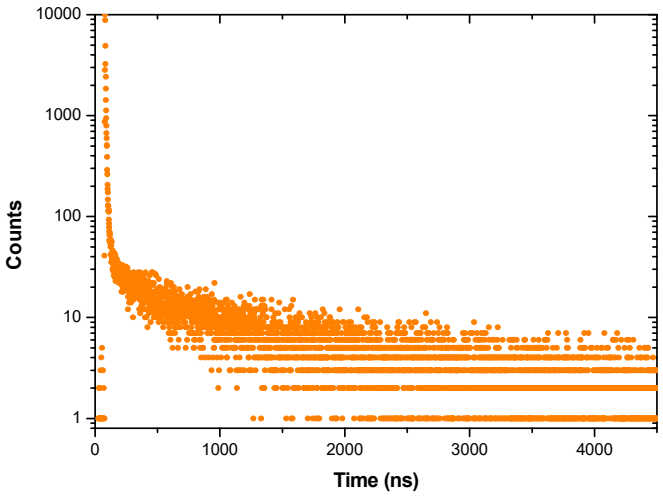

a)

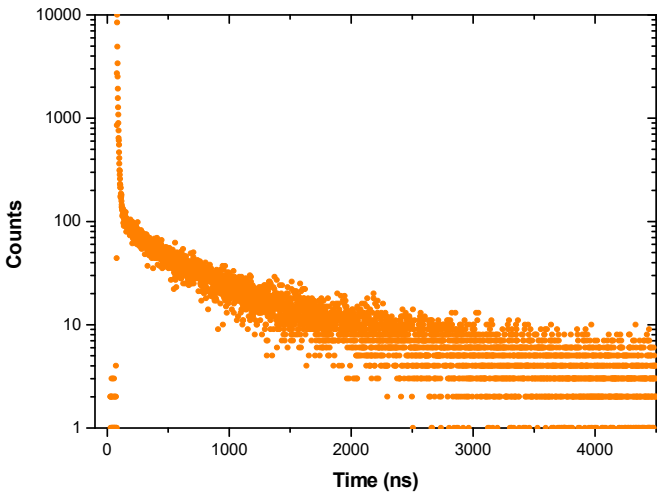

b)

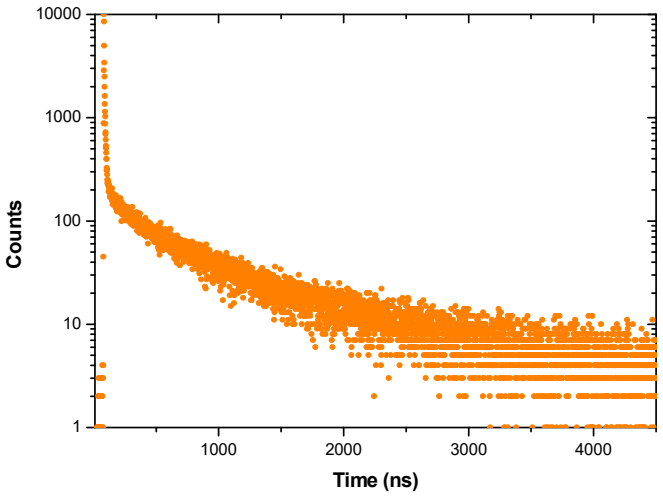

c)

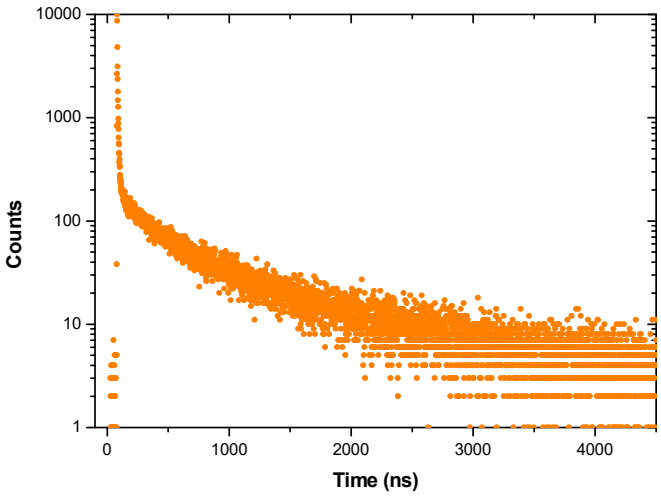

d)